INTERNATIONAL ATOMIC ENERGY AGENCY
UNITED NATIONS EDUCATIONAL, SCIENTIFIC AND CULTURAL ORGANIZATION
INTERNATIONAL CENTRE FOR THEORETICAL PHYSICS
I.C.T.P., P.O. BOX 586, 34100 TRIESTE, ITALY, CABLE: CENTRATOM TRIESTE

SMR.755/6

Workshop on Fluid Mechanics

(7 - 25 March 1994)

Lattice-gas models of phase separation: interfaces, phase transitions, and multiphase flow

Daniel H. Rothman
Department of Earth, Atmospheric, and Planetary Sciences
Massachusetts Institute of Technology
Cambridge, MA 02139
U.S.A.

and

Stéphane Zaleski
Laboratoire de Modélisation en Mécanique
C.N.R.S., Université Pierre et Marie Curie
4, Place Jussieu
75005 Paris
France

These are preliminary lecture notes, intended only for distribution

Lattice-gas models of phase separation: interfaces, phase transitions, and multiphase flow

Daniel H. Rothman[1]
Laboratoire de Physique Statistique
C.N.R.S., École Normale Supérieure
24, rue Lhomond
75005 Paris France

Stéphane Zaleski
Laboratoire de Modélisation en Mécanique
C.N.R.S., Université Pierre et Marie Curie
4, place Jussieu
75005 Paris France

Submitted to *Reviews of Modern Physics*, December 1993

[1]Permanent address: Department of Earth, Atmospheric, and Planetary Sciences, Massachusetts Institute of Technology, Cambridge, MA 02139

ABSTRACT

Momentum-conserving lattice gases are simple, discrete, microscopic models of fluids. This review describes their hydrodynamics, with particular attention given to the derivation of macroscopic constitutive equations from microscopic dynamics. Lattice-gas models of phase separation receive special emphasis. The current understanding of phase transitions in these momentum-conserving models is reviewed; included in this discussion is a summary of the dynamical properties of interfaces. Because the phase-separation models are microscopically time-irreversible, interesting unanswered questions are raised about their relationship to real fluid mixtures. Simulation of certain complex-fluid problems, such as multiphase flow through porous media and the interaction of phase transitions with hydrodynamics, is illustrated.

Contents

I. Introduction

Macroscopic complexity can mask microscopic simplicity. For example, the swirls and bursts of a turbulent fluid are just the collective dynamics that emerge from a large number of molecules interacting with each other via Newton's equation of motion. Whereas the microscopic dynamics in such a system are straightforward in principle, the organization of these microscopic motions to produce turbulence, or even hydrodynamics itself, remains shrouded in mystery.

Much, however, is of course known. Both the kinetic theory of gases and the Navier-Stokes equations of hydrodynamics date from the nineteenth century, while in this century considerable progress has been made towards the understanding of the connections between the microscopic or atomistic description of fluids and macroscopic hydrodynamics (Chapman and Cowling, 1970). Nevertheless, some relatively simple questions concerning the relation between these two levels of description are only just beginning to be addressed. For example, one may ask precisely how large a microscopic system of particles must be for it to contain enough degrees of freedom to be considered, at a larger scale, as a continuously varying macroscopic medium. To answer such questions, the advent of modern computers has been essential. Among the many achievements in the field of molecular-dynamics simulation has been the explicit demonstration that hydrodynamic flows can be obtained (albeit at considerable computational expense) from large molecular systems (Rapaport and Clementi, 1986; Mareschal and Kestermont, 1987)

We now know, however, that the complexity of hydrodynamics not only may be described by an explicit "averaging" of the N-body problem of molecular dynamics, but that virtually the same macroscopic hydrodynamic equations may be obtained from a drastically simplified version of molecular dynamics. Specifically, in 1986, Frisch, Hasslacher, and Pomeau showed that one may derive the Navier-Stokes equations from a microdynamics consisting of an artificial set of rules for collision and propagation of identical particles, each of which are constrained to move on a regular

lattice in discrete time with one of only a small, finite number of possible velocities (Frisch et al., 1986). This remarkable observation has not only had implications for statistical mechanics and kinetic theory, but also for the numerical simulation of certain hydrodynamic flows. This review is therefore dedicated to an explication of the original work of Frisch et al. and a review of some of the resulting ramifications during the eight years since its introduction.

Because the model of Frisch et al. is constructed from discrete dynamical variables (the velocities) that evolve on a discrete lattice in discrete time, it is an example of a *cellular automaton* (Farmer et al., 1984; Wolfram, 1986b; Toffoli and Margolus, 1987). The idea of cellular automata, which dates back to work of von Neumann and Ulam in the 1940's (von Neumann, 1966), is to find simple rules of spatial interaction and temporal evolution, from which collective, complex behavior emerges. The early motivations for this work came from biology: the goal, as described in the historical perspective given by Dyson (Dyson, 1979), was to provide a theory for how an artificial life capable of reproducing itself could be constructed. While applications of cellular automata to biology remain of current interest (see, for example, the book by Weisbuch (Weisbuch, 1991)), in the last two to three decades much of the interest has shifted to physics and computation. One of the earliest works in this regard is that of Zuse (Zuse, 1970), who was possibly the first to perceive the connections between cellular automata and the simulation of partial-differential equations. Other examples include studies of time-reversible automata (Margolus, 1984), speculations on the simulation of quantum-mechanical phenomena (Feynman, 1982), creation of a "statistical mechanics" of cellular automata (Wolfram, 1983), and explicit considerations of cellular automata as discrete dynamical systems (Vichniac, 1984) and as an alternative to partial-differential equations (Toffoli, 1984). Indeed, by 1985 there was a surfeit of speculation and expectation, but in the absence of any widely known, concrete example of a cellular-automaton model of a partial-differential equation, many were left wondering whether such models could indeed be constructed.

In this context the model of Frisch, Hasslacher, and Pomeau (FHP) was introduced. The model, an extension of earlier work by Hardy, de Pazzis, and Pomeau (Hardy et al., 1973; Hardy et al., 1976), consisted of identical particles that hop from site to site on a regular lattice, obeying simple collision rules that conserve mass and momentum. FHP showed that, at a spatial scale much larger than a lattice unit, and a temporal scale much slower than a discrete time step, the model asymptotically simulates the incompressible Navier-Stokes equations.

The FHP model, the first of a wide class of models that soon became known as *lattice-gas automata*, led to many interesting ramifications. First, as already mentioned, it demonstrated that the full details of real molecular dynamics are not necessary to create a microscopic model with macroscopic hydrodynamic behavior (Wolfram, 1986a; Kadanoff, 1986; Frisch et al., 1987; Kadanoff et al., 1989; Zanetti, 1989). Second, lattice-gas automata were immediately considered as an alternative means for the numerical simulation of hydrodynamic flows (d'Humières et al., 1985b; d'Humières and Lallemand, 1986; d'Humières and Lallemand, 1987). Third, the method gave rise to some new ideas for constructing models of certain complex fluids; specifically, fluid mixtures including interfaces, exhibiting phase transitions, and allowing for multiphase flows (Rothman and Keller, 1988; Appert and Zaleski, 1990). Thus lattice-gas automata have not only become "toy models" for the exploration of the microscopic basis of hydrodynamics, but also tools for the numerical study of certain problems in fluid mechanics. Both aspects of the subject are covered in this review.

In what follows, we first provide a broad overview of the field. We introduce the FHP model, describe in general terms its hydrodynamic limit, and illustrate its ability to simulate the Navier-Stokes equations. We then introduce lattice-gas models of multiphase fluids, and briefly describe two examples. One is a model of a binary fluid mixture that exhibits a phase-separation transition. The other contains just a single species of fluid, but exhibits a liquid-gas transition.

Following this overview, we then show how one may derive hydrodynamic equations from these microscopic models. We first describe the hydrodynamic limit of the simplest, single-component, models. We then review the state of theoretical understanding of the more complex, multiphase lattice gases. The hydrodynamic behavior of the multiphase models is in one case precisely the same, and in the other case very close, to that of the simplest lattice gases. Thus our emphasis on the multiphase models is concentrated on aspects of their phase transitions—in other words, the formation of interfaces—and on the physics of these interfaces themselves. We describe a catalog of results, both theoretical and empirical, that show that the macroscopic behavior of the multiphase models is qualitatively, if not quantitatively, similar to that obtained from classical models of phase transitions and interfaces. We argue that this agreement with classical theory is not only important for applications, but also for better understanding some of the foundations of statistical mechanics. Stated bluntly, these models break many classical rules—for example, their microdynamics is time-irreversible—but apparently without significant deleterious effect. Understanding why this may be remains one of the more important questions to be addressed.

In the remainder of the review we provide a broad overview of the variety of numerical experimentation that has been performed with lattice gases. We describe problems of both two and three dimensional flow, and of both single and multiple fluids. While the lattice gas may in principle be used for nearly any problem in hydrodynamic simulation, we emphasize that many of the most successful applications have involved either a complex fluid, a complex geometry, or both. Such complexity is perhaps best exemplified by the problem of multiphase flow through porous media.

Having stated the content of this review, we find it also worthwhile to indicate some of the subjects we do not cover. One such topic is multispeed models in which moving particles are no longer restricted to unit speed, thus allowing the definition of a temperature (Grosfils et al., 1992; Molvig et al., 1992; Qian et al., 1992a). Related to the internal energy transport in thermal models are models of diffusion or passive-

scalar transport. Diffusion is relatively simple to study with lattice gases, and indeed has been the subject of considerable attention (Burges and Zaleski, 1987; d'Humières et al., 1988; Chopard and Droz, 1988; McNamara, 1990; Kong and Cohen, 1991); it is, however, largely neglected by this review. Likewise, we also do not discuss recent lattice-gas models of reaction-diffusion equations (Dab et al., 1990; Dab et al., 1991; Kapral et al., 1991; Lawniczak et al., 1991). Lastly, we have chosen to devote only minimal attention to the "lattice-Boltzmann method," an important extension of the lattice gas which is of both theoretical and practical interest. Whereas we derive the lattice-Boltzmann equation from the Boolean dynamics of lattice gases in Section IV., methods for solving this equation are considered only in a brief, introductory, discussion in Appendix C. Further details of the lattice-Boltzmann method can be found in the recent review paper by Benzi et al. (Benzi et al., 1992).

II. Lattice-gas models of simple fluids

In this paper, the term "lattice gas" refers to a system of particles that move with a discrete set of velocities from site to site on a regular lattice. This kind of lattice gas is in some ways a generalization of the classical lattice-gas models that have been employed, for example, in theoretical models of the liquid-gas transition (Stanley, 1971). The major difference between the "new" lattice-gas models and their classical counterparts is dynamical: momentum is explicitly conserved in the new models, thereby allowing one to obtain hydrodynamic equations of motion. These momentum-conserving lattice gases are thus of interest for both hydrodynamics and statistical mechanics.

In this section, we first provide a brief historical overview of some specific hydrodynamic lattice-gas models. We then introduce in some detail the lattice-gas model of Frisch et al. (Frisch et al., 1986), and follow that discussion with some examples of lattice gas simulations.

A. Historical overview

From the viewpoint of hydrodynamics, the essential innovation due to momentum-conserving lattice gases is the simultaneous discretization of space, time, velocity, and density. Discretization of space and time is in modern times relatively mundane, being an everyday occurence in the numerical solution of partial-differential equations by, for example, the method of finite differences. Discretization of velocities, however, is a relatively unusual idea. It seems to have first been considered for hydrodynamic flows by Broadwell, who constructed a discrete-velocity, continuous-time, continuous-space, and continous-density model to find exact solutions to a Boltzmann equation describing shock waves (Broadwell, 1964). Further ramifications of this approach are described in the monograph by Gatignol (Gatignol, 1975).

The first discrete-velocity model in statistical mechanics appears to have been pro-

posed by Kadanoff and Swift (Kadanoff and Swift, 1968). In an attempt to demonstrate the theoretical possibility of the divergence of transport coefficients near the critical point, they created a version of a classical Ising model in which positive spins acted as particles with momentum in, say, one of 4 directions on a square lattice, while negative spins acted as holes. Particles were then allowed to collide with other particles, or exchange their positions with holes, but only if energy (based on nearest-neighbor Ising interactions) and momentum were exactly conserved. The model, purely analytic in the form of a master equation, was discrete in space, velocity, and density, but not in time. One of the new results was that, despite its simplicity, the dynamics led to hydrodynamics via the existence of sound waves.

A fully discrete model of hydrodynamics was first introduced in the 1970's by Hardy, de Pazzis, and Pomeau (Hardy et al., 1973; Hardy et al., 1976). Their model consisted of identical particles moving from site to site on a square lattice in discrete time, conserving particle number and momentum upon collision. Their objective was not the simulation of hydrodynamics in the broad sense, but rather the study of issues in statistical mechanics such as ergodicity and the divergence of transport coefficients in two dimensions. Using the simplest possible model of molecular dynamics, their work is notable not only for the reasons cited, but also for the interesting interplay provided by the comparisons between theoretical predictions of the model's transport properties and the empirical results obtained from numerical simulations of it.

Although the model of Hardy et al. led to a number of interesting results, it has had only limited applications because its hydrodynamic limit is anisotropic. This is the direct—and rather unsurprising—consequence of the constraints imposed by the underlying square lattice. It was not realized until 1986, in the aforementioned work of FHP (Frisch et al., 1986), that a simple extension of the model to a *triangular* lattice would suffice for isotropic hydrodynamics. We thus turn now to an introduction to the FHP model.

B. The FHP lattice gas

In the following, we first introduce a *microdynamical* description of the FHP model. We then provide an outline of the derivation of the *macrodynamical*, or hydrodynamic, behavior. Full details concerning the hydrodynamic limit are given in Section IV..

1. Microdynamics

The FHP gas is constructed of discrete, identical particles which move from site to site on a triangular lattice, colliding when they meet, always conserving particle number and momentum. The dynamics evolves in discrete time steps; a representative example of the evolution during one time step is illustrated in Figure 1. The initial configuration is given in Figure 1a. Each arrow represents a particle of unit mass moving with unit speed (one lattice unit per time step) in one of 6 possible directions given by the lattice links. No more than one particle may reside at a given site and move with a given velocity; thus, in this example, 6 bits of information suffice to fully describe the configuration at any site.

Each discrete time step of the lattice gas is composed of two steps. In the first, each particle hops to a neighboring site (Figure 1b) in the direction given by its velocity. In the second step (Figure 1c), the particles may collide. The precise collision rules are parameters of the model; all collisions, however, conserve mass and momentum. Two examples of collisions that result in a change in the velocity of particles are evident by comparing the middle row in Figure 1b and Figure 1c. Note that the two-body collision could just as easily have been a counter-clockwise rotation instead of clockwise. Typical implementations perform both with equal probability, either through the use of random numbers or via a deterministic scheme. Explicit examples of collisions are given in Figure 2.

The microdynamics in Figure 1 are expressed by the following equation:

$$n_i(\mathbf{x}+\mathbf{c}_i, t+1) = n_i(\mathbf{x}, t) + \Delta_i[\mathbf{n}(\mathbf{x}, t)]. \qquad \text{(II.1)}$$

The Boolean variables $\mathbf{n} = (n_1, n_2, \ldots, n_6)$ indicate the presence (1) or absence (0) of particles moving from site $\mathbf{x}$ to site $\mathbf{x} + \mathbf{c}_i$, where the possible velocities are given by

$$\mathbf{c}_i = (\cos \pi i/3, \sin \pi i/3), \qquad i = 1, 2, \ldots, 6. \tag{II.2}$$

The collision operator Δ_i describes the change in $n_i(\mathbf{x}, t)$ due to collisions, and takes on the values ± 1 and 0. It is the sum of Boolean expressions, one for each possible collision. For example, the operator for the three-body collision in Figure 2 is given by

$$\begin{aligned} \Delta_i^{(3)} &= n_{i+1} n_{i+3} n_{i+5} (1 - n_i)(1 - n_{i+2})(1 - n_{i+4}) - \\ &\quad n_i n_{i+2} n_{i+4} (1 - n_{i+1})(1 - n_{i+3})(1 - n_{i+5}), \end{aligned} \tag{II.3}$$

where the circular shift $i + 3 = j$ such that $\mathbf{c}_j = -\mathbf{c}_i$, $j = 1, \ldots, 6$. The operator for the two-body collision in Figure 2 is

$$\begin{aligned} \Delta_i^{(2)} &= a n_{i+1} n_{i+4} (1 - n_i)(1 - n_{i+2})(1 - n_{i+3})(1 - n_{i+5}) + \\ &\quad (1 - a) n_{i+2} n_{i+5} (1 - n_i)(1 - n_{i+1})(1 - n_{i+3})(1 - n_{i+4}) - \\ &\quad n_i n_{i+3} (1 - n_{i+1})(1 - n_{i+2})(1 - n_{i+4})(1 - n_{i+5}). \end{aligned} \tag{II.4}$$

Note that $\Delta_i^{(2)}$ allows for clockwise rotations when the supplementary Boolean variable $a(\mathbf{x}, t) = 1$, and counter-clockwise rotations when $a(\mathbf{x}, t) = 0$. For the simplest lattice gas, the full collision operator Δ_i is

$$\Delta_i = \Delta_i^{(2)} + \Delta_i^{(3)}. \tag{II.5}$$

More elaborate collision operators may be formed by including, for example, four-body collisions, or by allowing for collisions with stationary, or "rest" particles (d'Humières and Lallemand, 1987). In the usual formulations, the only restrictions on Δ_i are that it conserve mass,

$$\sum_i \Delta_i(\mathbf{n}) = 0, \tag{II.6}$$

and that it conserve momentum,

$$\sum_i \mathbf{c}_i \Delta_i(\mathbf{n}) = 0. \tag{II.7}$$

Using the first of these relations, one may sum the microdynamical equation (II.1) over each direction i to obtain an expression for the conservation of mass,

$$\sum_i n_i(\mathbf{x} + \mathbf{c}_i, t + 1) = \sum_i n_i(\mathbf{x}, t), \tag{II.8}$$

and, after multiplying the same equation by $\mathbf{c}_i$, summing again over i, and using the second relation, one obtains an expression for the conservation of momentum,

$$\sum_i \mathbf{c}_i n_i(\mathbf{x} + \mathbf{c}_i, t + 1) = \sum_i \mathbf{c}_i n_i(\mathbf{x}, t). \tag{II.9}$$

Equations (II.8) and (II.9) describe the evolution of mass and momentum in the Boolean field, and may be considered as the microscopic mass-balance and momentum-balance equations, respectively, of the lattice gas.

2. Macrodynamics

Conservation of mass and momentum at the microscopic or molecular scale of a fluid implies the same conservation at a macroscopic, or continuum scale. It is at this scale, and partly from these conservation laws, that the Navier-Stokes equations are derived (Landau and Lifshits, 1959a; Batchelor, 1967). One expects that much the same analysis should apply to the lattice gas.

To obtain a broad overview of why this is possible, consider a contiguous, enclosed set of lattice sites. Note that the change in mass within this set is precisely balanced by the flux of mass out of it. Consider, then, the evolution of the average quantity $\langle n_i \rangle$, in which the average is taken over an ensemble of systems prepared with different initial conditions. We identify $\sum_i \langle n_i \rangle$ with the mass and $\sum_i \langle n_i \rangle \mathbf{c}_i$ with the mass flux. Whereas the unaveraged Boolean field is necessarily noisy at the smallest scales, we may assume that $\langle n_i \rangle(\mathbf{x}, t)$ is slowly varying in both space and time. We can thus

infer that temporal and spatial scales much larger than one time step and one lattice unit, but still small enough such that $\langle n_i \rangle$ varies slowly, may be defined in the limit of long times and large lattices. Since the same balance between mass change and mass flux that applies to n, also applies to $\langle n_i \rangle$, we may conclude, via the divergence theorem and the usual arguments of continuum mechanics, that

$$\partial_t \sum_i \langle n_i \rangle = -\partial_\alpha \sum_i \langle n_i \rangle c_{i\alpha}, \tag{II.10}$$

where the α-component of the ith velocity vector $\mathbf{c}_i$ is given by $c_{i\alpha}$, and the Einstein summation convention is assumed over indices given by Greek letters.

One may reach a similar conclusion for the momentum. The change in the α-component of momentum in any region of the lattice is itself precisely balanced by the flux of α-momentum in the β-direction, $\sum_i \langle n_i \rangle c_{i\alpha} c_{i\beta}$, out of this region. Thus, by the same argument, one obtains

$$\partial_t \sum_i \langle n_i \rangle c_{i\alpha} = -\partial_\beta \sum_i \langle n_i \rangle c_{i\alpha} c_{i\beta}. \tag{II.11}$$

Finally, by defining the mass density $\rho = \sum_i \langle n_i \rangle$ and the momentum density $\rho u_\alpha = \sum_i \langle n_i \rangle c_{i\alpha}$, and substituting into equations (II.10) and (II.11), we obtain the familiar continuity equation,

$$\partial_t \rho = -\partial_\alpha (\rho u_\alpha), \tag{II.12}$$

and the macroscopic momentum-balance equation,

$$\partial_t (\rho u_\alpha) = -\partial_\beta \Pi_{\alpha\beta}, \tag{II.13}$$

of hydrodynamics, where in the latter we have introduced the momentum flux density tensor (Landau and Lifshitz, 1959a)

$$\Pi_{\alpha\beta} = \sum_i \langle n_i \rangle c_{i\alpha} c_{i\beta}. \tag{II.14}$$

While equation (II.12) is fully explicit, the writing of momentum conservation as an explicit equation in terms of ρ and $\mathbf{u}$ requires some work. Not surprisingly, the

presence of an underlying lattice makes this derivation of hydrodynamics somewhat different from the usual fluid case. The seminal contribution of FHP was to notice that in a low velocity expansion, a second order tensor such as $\Pi_{\alpha\beta}$ is written (Frisch et al., 1986)

$$\Pi_{\alpha\beta} = p_0(\rho)\delta_{\alpha\beta} + \lambda_{\alpha\beta\gamma\delta}(\rho) u_\gamma u_\delta + \mathcal{O}(u^4) \tag{II.15}$$

where p_0 and $\lambda_{\alpha\beta\gamma\delta}$ must be obtained from equation (II.14) and the expressions for $\langle n_i \rangle$, the average populations. In ordinary continuous media the tensor $\lambda_{\alpha\beta\gamma\delta}$ is readily found to be isotropic and to preserve Galilean invariance. However, because we work with an underlying lattice, it is not the case for lattice gases. In fact, $\lambda_{\alpha\beta\gamma\delta}$ acts instead as an elasticity tensor, and inherits the symmetry properties of the lattice just as elasticity tensors share the symmetry properties of a crystal lattice. This "memory" of the lattice would in fact doom our effort to simulate a fluid, except for a remarkable property of hexagonal lattices well noticed by Landau and Lifschitz, who wrote (Landau and Lifshitz, 1959b), "It should be noticed that deformation in the xy-plane (...) is determined by only two moduli of elasticity, as for an isotropic body; that is, the elastic properties of a hexagonal crystal are isotropic in the plane perpendicular to the [hexagonal] axis." In equations, isotropy implies the general form

$$\lambda_{\alpha\beta\gamma\delta}(\rho) = A(\rho)\delta_{\alpha\beta}\delta_{\gamma\delta} + B(\rho)(\delta_{\alpha\gamma}\delta_{\beta\delta} + \delta_{\alpha\delta}\delta_{\beta\gamma}), \tag{II.16}$$

where $\delta_{\alpha\beta}$ is the Kronecker delta and A and B are two independent "elastic" moduli, which must be determined from the average populations $\langle n_i \rangle$, as is done in Section IV.. Once this is done, the momentum conservation equation takes the following form, from (II.13), (II.15), and (II.16):

$$\partial_t \rho u_\alpha + 2\partial_\beta B(\rho) u_\alpha u_\beta = -\partial_\alpha [p_0(\rho) + A(\rho) u^2]. \tag{II.17}$$

This equation is close, but not quite identical, to the usual Euler equation for compressible flow. Moreover, we have not given the expression for the coefficients A and B, nor for $p_0(\rho)$. However, as we detail in Section IV., in the limit of vanishing u, the

lattice gas hydrodynamical equation is equivalent to the usual *incompressible* Euler equation.

To obtain the viscous term, and therefore the Navier-Stokes equation of the lattice gas, one needs also to consider gradients of the momentum field at second order. The fourth-rank *viscous stress tensor*, itself obeying the symmetries of equation (II.16), is then introduced to relate viscous stress to velocity gradients in the lattice gas. The two free parameters of this tensor then determine the shear and bulk viscosities (just as they would give the Lamé parameters in elasticity theory). That the lattice gas does indeed have a viscosity is conceptually deduced by observing that collisions and propagation control the rate at which momentum diffuses. The relevant diffusion coefficient, or kinematic viscosity, may then be calculated via a Boltzmann approximation; i.e., by ignoring correlations between particles (Hénon, 1987b). Each of these issues are addressed in detail in Section IV..

Finally, we note that the derivation of hydrodynamics in this section, crude as it is, reveals one very important point: the precise details of the collision rules (aside from certain pathological choices to be discussed later) do *not* affect the form of the constitutive, hydrodynamic equations. Rather, they determine the values of the transport coefficients.

C. Simulations

Before introducing models with interfaces, it is useful to illustrate the kind of hydrodynamic simulation that is possible with the FHP model.

Figure 3 shows one of the first hydrodynamic flows simulated by the lattice-gas method (d'Humières et al., 1985b). This two dimensional flow past a flat plate is forced by injecting particles at the left boundary of the lattice and removing particles at the right boundary, thus creating a pressure gradient. The flow, at a Reynolds number of approximately 70, creates vortices, known as *von Karman streets*, behind the plate. This flow field qualitatively matches those that would be obtained from

quasi-two-dimensional experiments or other methods of numerical simulation.

As we shall discuss later, one interesting aspect of the lattice-gas method is the ease with which one may simulate flows in complex geometries. An application of this capability is the study of flows through microscopically disordered porous media. An example of a simulation of flow through a two-dimensional porous medium is shown in Figure 4 (Rothman, 1988). Flows such as these obey a linear force-flux relation known as Darcy's law; the simulations allow estimation of the conductivity, or permeability, coefficient of the bulk flow.

These and other simulational studies are described in more detail in Section IX.. Now, however, we turn to a consideration of how the simple FHP model may be modified to simulate the dynamics of certain multiphase fluids and interfaces.

III. Lattice-gas models of phase-separating mixtures

As already indicated in the introduction, one of the important generalizations of the FHP lattice gas has been the introduction of discrete models for the simulation of hydrodynamic mixtures. The earliest models of mixtures were conceived simply by adding a second species of particles. In the case of a *passive* scalar (Chen and Matthaeus, 1987; Baudet et al., 1989), the only new dynamics of interest is diffusion of one species into the other. The second species, however, can also be *active*. Thus, for example, Burges and Zaleski (Burges and Zaleski, 1987) created a model of a mixture that was not only diffusive but also buoyant. A further generalization of this sort is the introduction of *reactive* fluids (Clavin et al., 1986; d'Humières et al., 1987; Clavin et al., 1988; Dab et al., 1990; Dab et al., 1991; Kapral et al., 1991). In this case collisions involving more than one species need not conserve the number of particles of each species entering a collision.

In each of the mixture models cited above, the dynamics of collisions and propagation of the (unforced) fluid mixture are independent of the particular species that a particle may represent; the new behavior comes instead from the redistribution of species (i.e., mass) after performing the FHP collisions described in the previous section. Thus a second, qualitatively different, mixture model results from creating a dynamics in which the redistribution of *momentum* depends on the distribution of mass (or possibly also momentum) prior to collision. We introduce two such models below. In the first case, two species interact with each other to create interfaces with surface tension. In the second, a single species of particles interacts with itself and also forms interfaces, but rather than separating two species of fluids the interface separates a dense (liquid) phase from a less dense (vapor) phase.

A. Immiscible lattice gas

The *immiscible lattice gas* (ILG) is a two-species variant of the FHP model (Rothman and Keller, 1988). At a mechanistic level, the differences from and similarities to the FHP model are best realized from a comparison of the microdynamics of the two models.

Figure 5 illustrates the ILG microdynamics. The initial state (Figure 5a) of the lattice is the same as in Figure 1, but now some of the particles are colored "red," while the others are colored "blue." The hopping step, Figure 5b, is precisely as before: particles propagate to the neighboring site in the direction of their velocity. The collision step in Figure 5c, however, is different. Roughly speaking, the ILG collision rule changes the configuration of particles so that, as much as possible, red particles are directed towards neighbors containing red particles, and blue particles are directed towards neighbors containing blue particles. The total mass, the total momentum, and the number of red (or blue) particles are conserved. Two examples of this collision rule are seen by comparing the middle row of Figure 5b with that of Figure 5c.

The ILG microdynamics may be described as follows. Each lattice site may contain red particles, blue particles, or both, but at most one particle (red or blue) may move in each of the six directions $\mathbf{c}_1, \ldots, \mathbf{c}_6$. In the usual implementation, each site may also have a seventh stationary, or rest, particle moving with velocity $\mathbf{c}_0$ and subject to the same exclusion rule. The configuration at a site $\mathbf{x}$ is thus described by the Boolean variables $\mathbf{r} = \{r_i\}$ and $\mathbf{b} = \{b_i\}$, where the roman index i again indicates the velocity, and r_i and b_i cannot simultaneously equal 1.

At a site $\mathbf{x}$, a color flux $\mathbf{q}$ is defined to be the difference between the red momentum and the blue momentum:

$$\mathbf{q}[\mathbf{r}(\mathbf{x}), \mathbf{b}(\mathbf{x})] \equiv \sum_{i=1}^{6} \mathbf{c}_i [r_i(\mathbf{x}) - b_i(\mathbf{x})]. \qquad \text{(III.1)}$$

A vector proportional to the local color gradient (or "field") is also defined, by

$$\mathbf{f}(\mathbf{x}) \equiv \sum_i \mathbf{c}_i \sum_j [r_j(\mathbf{x}+\mathbf{c}_i) - b_j(\mathbf{x}+\mathbf{c}_i)]. \tag{III.2}$$

The ILG collision rule is anti-diffusive: it maximizes the flux of color in the direction of the local color gradient. The result of a collision, $\mathbf{r} \to \mathbf{r}'$, $\mathbf{b} \to \mathbf{b}'$, is the configuration that maximizes

$$\mathbf{q}(\mathbf{r}', \mathbf{b}') \cdot \mathbf{f}, \tag{III.3}$$

such that the number of red particles and the number of blue particles is conserved,

$$\sum_i r_i' = \sum_i r_i, \qquad \sum_i b_i' = \sum_i b_i, \tag{III.4}$$

and so is the total momentum:

$$\sum_i \mathbf{c}_i(r_i' + b_i') = \sum_i \mathbf{c}_i(r_i + b_i). \tag{III.5}$$

If more than one choice for $\mathbf{r}', \mathbf{b}'$ maximizes (III.3), then the outcome of the collision is chosen with equal probability from among these optimal configurations.

Analogous to the discrete microdynamical equation (II.1) for the FHP model, we have two coupled microdynamical equations for the ILG, one for the red particles,

$$r_i(\mathbf{x}+\mathbf{c}_i, t+1) = r_i'(\mathbf{x}, t) \tag{III.6}$$

and another for the the blue particles,

$$b_i(\mathbf{x}+\mathbf{c}_i, t+1) = b_i'(\mathbf{x}, t), \tag{III.7}$$

where

$$r_i' = C_i^r(\mathbf{r}(\mathbf{x}, t), \mathbf{b}(\mathbf{x}, t), f_*) \tag{III.8}$$

and

$$b_i' = C_i^b(\mathbf{r}(\mathbf{x}, t), \mathbf{b}(\mathbf{x}, t), f_*) \tag{III.9}$$

are the post-collision, pre-propagation states. The collision operators C_i^r and C_i^b assume values of either 0 or 1 and are given implicitly by the maximization of the

quantity (III.3). Note that both C_i^r and C_i^b depend not only on the red and blue population at site $\mathbf{x}$, but also on f_*, the discrete color gradient or field angle obtained from a simplification (described in Section V.C.2.) of equation (III.2). Although here we only discuss ILG models that obtain f_* from information at neighboring sites, ILG models without explicit dependence on neighboring sites have also been proposed (Somers and Rem, 1991; Chen et al., 1991b). These models use colored "holes" in addition to colored particles to obtain f_* using only the local state.

A salient feature of the ILG is its ability to simulate phase separation in a binary mixture; an example is shown in Figure 6. Here a 256×256 lattice is initialized as a random mixture with average density $\rho = 4.9$ particles per site, with 50% of the particles red, and 50% blue. As time progresses, the domains of red and blue grow larger, eventually resulting in a steady state in which one thick blue stripe is parallel to an equally thick red stripe. Measurements show that the red rich phase is virtually ($\gg$99%) pure red, and likewise for blue.

Later we will discuss simulations of phase separation in greater detail, both from a phenomenological and theoretical point of view. We note now, however, that the collision rule defined by equations (III.1)–(III.3) can differ from the plain FHP collisions only if there is more than one color present at the site located at $\mathbf{x}$; it is only in this case that different combinations of r_i and b_i can create different values of the color flux q that can contribute differently to the maximization of (III.3). Thus, after we establish later that there is indeed surface tension at the interfaces, we shall see that in addition to being a model of phase separation in a binary fluid, the ILG is also a model of the hydrodynamics of two-phase flow.

B. Liquid-gas model

In our second model of a multiphase fluid, a *liquid-gas* (LG) model, there is only one species of particle, but two "thermodynamic" phases (Appert and Zaleski, 1990). One phase—liquid—has a high density of particles, while the other phase—gas—is

relatively rarefied. The two phases result from a rule that exchanges momentum between sites separated by one or more lattice units, which, as we shall show later, modifies the relationship between pressure and density (the "equation of state") in such a way as to allow coexistence of the dense and rarefied phases.

Figure 7 illustrates the dynamics. The initial state and the hopping step are precisely the same as in Figure 1. There are, however, now two collision steps. The first collision step, Figure 7c, is the same as in the FHP model. We write the outcome of this "classical" collision as

$$n_i' = n_i + \Delta_i(\mathbf{n}). \tag{III.10}$$

In the second, interacting, collision step (Figure 7d), sites at locations $\mathbf{x}$ and $\mathbf{x} + r\mathbf{c}_i$ (where here we choose $r = 2$) trade particles moving in directions $-\mathbf{c}_i$ and $\mathbf{c}_i$, respectively, if and only if both particles exist prior to the exchange *and* the exchange can be performed without violating the exclusion rule. Figure 8 illustrates the rule in detail. In terms of Boolean variables, we define

$$\gamma_i = \bar{n}_i'(\mathbf{x}) n_{i+3}'(\mathbf{x}) n_i'(\mathbf{x} + r\mathbf{c}_i) \bar{n}_{i+3}'(\mathbf{x} + r\mathbf{c}_i), \tag{III.11}$$

where overbars indicate the Boolean operator "not" and the circular shift $i + 3$ is defined as in equations (II.3) and (II.4). The ability to perform the interaction is thus given by the Boolean variable γ_i, and the microdynamical equation describing the complete sequence of propagation followed by classical and interacting collisions becomes

$$n_i(\mathbf{x} + \mathbf{c}_i, t + 1) = n_i'(\mathbf{x}, t) + \gamma_i - \gamma_{i+3}. \tag{III.12}$$

The liquid-gas models that were originally proposed contained more interactions, requiring both a more complicated analysis and implementation (Appert and Zaleski, 1990; Appert et al., 1991; Appert and Zaleski, 1993). In this review, we discuss only the simpler model of Appert et al. (Appert et al., 1993b), given by equations (III.11) and (III.12). Though the old and new models differ quantitatively (e.g., the values of the transport coefficients), the qualitative behavior remains the same.

As in the ILG, the salient feature of the liquid-gas model is phase separation, which will occur for certain choices of the initial density of particles. This behavior is illustrated in Figure 9. Unlike the ILG, phase separation in the liquid-gas model manifests itself not as the segregation of two species of particles into separate regions, but as the segregation of a single species of particle into regions of high and low density. As we shall show, the relative volume of each region depends on the initial total density of the single species, rather than the relative concentration of two species as in the ILG.

Lastly, we note that, unlike the ILG, the hydrodynamic behavior of the bulk phases of the liquid-gas model do not automatically reduce to that of the FHP model. One must instead perform the same multiscale expansion used to analyze the plain lattice gas; the results (detailed in Section VI.) are then seen to differ only in terms such as the viscosity.

IV. Theory of simple lattice gas automata

In this section we review the theory that leads from the microscopic definition of simple, single-component lattice gases given below in section IV.A. to the large-scale hydrodynamic equations. A great simplification is achieved if one uses the Boltzmann molecular-chaos assumption, which is equivalent to considering that the particles entering a collision are not correlated. From this assumption one obtains the Fermi-Dirac equilibrium distribution for the lattice gas automaton. This equilibrium distribution allows one to find the hydrodynamical equations. The first result is the Euler equation for the lattice gas. The Fermi-Dirac equilibrium and the Euler equation appear at the lowest order of a multiple scale or Chapman-Enskog expansion for the lattice gas. At second order, this expansion yields the Navier-Stokes equations and explicit expressions for the viscosity of the model as we show in Section IV.B..

A more general statistical-mechanical approach abandons the molecular-chaos assumption and could yield a more rigorous theory for the lattice gas. However, this approach is only partially developed at present, and we review it only briefly in Section IV.C.. There we show, for example, that the equilibrium state may be obtained directly as a solution of a Liouville equation, instead of a Boltzmann equation. The discussion of more subtle effects of space discretization such as the doubling of the number of momentum-like invariants is also done in Section IV.C.. The reader interested only in general ideas about the derivation of the Navier Stokes equations may skip Section IV.C. and lose little of immediate relevance to the more complex lattice gas models described in the remainder of the review.

A. Some typical lattice gas automata

1. Regular Bravais lattices

The term *lattice* denotes a set of points $\mathcal{L}$ in D-dimensional space R^D. In a *Bravais lattice* each point has identical surroundings. Mathematically this means that the

lattice is invariant by a translation that brings any point of $\mathcal{L}$ on any other point. In equations, we let $T_{\mathbf{u}}$ be a translation of space by a vector $\mathbf{u}$. Then

$$T_{\mathbf{x}-\mathbf{y}}\mathcal{L} = \mathcal{L}$$

for any pair $(\mathbf{x}, \mathbf{y})$ of vectors of $\mathcal{L}$. We let $\{\mathbf{c}_i\}$ be the set of vectors joining a point to its nearest neighbors, in agreement with the notation introduced in Section II.. A lattice is *periodic* if it is invariant by a group of translations, i.e. by a set of translations $\{T_{\mathbf{w}}\}$ with

$$\mathbf{w} = n_1\mathbf{u}_1 + \cdots + n_k\mathbf{u}_k \tag{IV.13}$$

where all the n_i are variable integers and the $\mathbf{u}_i$ are arbitrary fixed vectors. It is easily proved that all Bravais lattices are periodic.

The notion of *regular polytope* generalizes to higher dimensions the notion of regular polygon or polyhedron. A more precise definition together with some geometrical facts is given in Appendix A. The *point symmetry group* $\mathcal{G}$ of a lattice is the group of *congruent transformations* (or *isometries* in French) leaving a lattice point fixed and the lattice globally invariant. It is easily proved that this is also the symmetry group of a polytope associated with the lattice. This is the polytope whose vertices are the vectors $\mathbf{c}_i$ connecting a site of the lattice to a set of neighbors (see Appendix A for more details). A *regular Bravais lattice* is a Bravais lattice in which the latter polytope is regular. Since we wish to consider models that yield sufficiently isotropic large-scale equations, we will restrict all developments to regular Bravais lattices. There are only two such lattices in 2D, the square and hexagonal lattices.

2. Models on the hexagonal lattice

a. Six-velocity model The six-velocity model was described in Section II.B.. The collision rules given in equations (II.3) and (II.4) correspond to the original FHP-I model. It is useful when discussing this and subsequent models to have in mind a classification of all configurations by classes of equal momentum and mass.

Then each configuration is characterised by 3 numbers (n, g_x^*, g_y^*) where the integers n, g_x^*, g_y^* label the particle number and momentum. They are defined by

$$\left.\begin{aligned} n(s) &= \sum_i s_i \\ g_x^*(s) &= 2g_x(s) \\ g_y^*(s) &= \frac{2}{\sqrt{3}} g_y(s) \end{aligned}\right\} \qquad \text{(IV.14)}$$

where $\mathbf{g}(s) = \sum_i s_i \mathbf{c}_{i\alpha}$ is the momentum of configuration s and the factors 2 and $2/\sqrt{3}$ are added to obtain integer values for n, g_x^*, g_y^*.

The possible configurations for a six-velocity lattice gas are shown in Figure 10. It is immediately seen that the FHP-I model does not perform all possible collisions. There are for instance 2 members in class (3, 1, 1) which could be transformed into each other by collision. Including all such collisions leads to a six-velocity collision-saturated model (d'Humières and Lallemand, 1987). We return to the definition of these models below.

b. Seven-velocity model Although the FHP-I model is very simple, it has certain unwelcome features. For instance, the triple collision is relatively infrequent compared to the pair collisions. This is unfortunate, since pair collisions conserve not only mass and momentum but an additional invariant. As we shall see below this viciates the derivation of hydrodynamics. Another difficulty is that the compression viscosity is zero for the FHP-I model (Frisch et al., 1987). A simple improvement is to add one or several rest particles. In what follows we will restrict ourselves to only one rest particle.

At this point it is useful to introduce the standard notation (d'Humières and Lallemand, 1987) for multiple speed models. The particle velocities now optionally carry a double index $i = (k, j)$. The speed index k is 0 for rest particles and 1 for moving particles. The index j varies from 1 to 6 and indicates the direction of the velocity vector. Velocities are noted $\mathbf{c}_{kj}$ or $\mathbf{c}_i$ where in the latter case the single index i implies the two indices. Likewise particle Boolean variables are noted n_{kj} or n_i, etc. The $\mathbf{c}_{1j}$

are the 6 unit vectors parallel to the axes on the hexagonal lattice, and $\mathbf{c}_{01} = 0$.

The possible configurations for 7-bit models are shown in Figure 11. In this figure, we describe the configurations only up to a rotation or reflection. It is seen that there are two subgroups of class (3,0,0), which we call $(3,0,0)^A$ and $(3,0,0)^B$, containing 2 or 3 configurations which can be transformed into each other by rotations.

The *collision-saturated seven-velocity model* (also known as FHP-III) has the following collision rules. Configurations are transformed into any of the *other* configurations of the same class (n, g_x^*, g_y^*). However in some cases, such as class $(3,0,0)$, the collision output is chosen to be another member of the same subclass, either $(3,0,0)^A$ or $(3,0,0)^B$. There are at most $p = 3$ members of a class or subclass in this scheme. Thus there are at most 2 outputs to chose from. The choice is achieved with a random bit as described in Section II.B..

Another model which will be useful in what follows is the *random-collision seven-velocity model*. A configuration in a class (n, g_x^*, g_y^*) is transformed into any configuration in the same class, including the original one. There are at most $p = 5$ configurations to choose from (Figure 11). The collision rate for state s going into state s' is defined to be $A(s, s') = 1/p$. More than one random bit is now needed. In practice a random number generator is used to choose from the p configurations.

3. A three dimensional model: the face-centered hypercubic lattice

Three-dimensional lattice-gas automata were first introduced by d'Humières et al. (d'Humières et al., 1986). 3D models are constructed on the the face-centered hypercubic (FCHC) lattice, a generalisation to 4D of the face centered cubic lattice. The latter is already the most symmetric of the 3D lattices (it has dodecahedral symmetry) but fails to ensure the symmetry of fourth-order tensors such as $\lambda_{\alpha\beta\gamma\delta}$ defined in Section II.. The FCHC lattice is generated by the set of 24 velocity vectors $\mathbf{c}_i$ of the form $(\pm 1, \pm 1, 0, 0)$ together with all permutations of the four components. It is also the set of points $\mathbf{x} = (a, b, c, d)$ with integer coordinates and $a + b + c + d$ even. The

"visualisation" of such a lattice is difficult if not impossible. However a good grasp of the nature of the FCHC lattice may be obtained from an analogy with staggered lattices in 2D or 3D. In particular, the face-centered cubic (FCC) lattice is made of all the points $\mathbf{x} = (a, b, c)$ with $a + b + c$ even. Notice in Figure 12 that the FCC lattice is not the entire cubic lattice with all points of integer coordinates (a, b, c) but just half of it. In a similar way the FCHC lattice forms a staggered subset of the hypercubic lattice, just as the FCC lattice is half of the cubic lattice. When projected onto the 3D hyperplane $d = 0$ the velocity vectors in the FCHC lattice fall in the two sets depicted in Figure 13: 12 diagonal vectors lie in the plane $d = 0$ while the 12 other vectors fall on the Cartesian axes with $d = \pm 1$. It is interesting to note that the generating vectors $\mathbf{c}_i$ are also vertices of the four dimensional polytope defined by the Schläfi symbol $\{3, 4, 3\}$. (See Appendix A for a definition of the Schläfi symbol.) A projection of the $\{3, 4, 3\}$ polytope is shown in Figure 14.

Although the FCHC collisions must be performed in 4D, simulations of 3D flow may be performed on lattices which are only a few layers wide in the fourth dimension. Because of the staggered nature of the lattice, the thinnest possible slab is two lattice spacings wide in the fourth dimension. Although such slabs are commonly used, Brito and Ernst (Brito and Ernst, 1991b) pointed out that excess correlations may appear in such thin slabs.

Finally, we note that the definition of a collision operator for the FCHC lattice with 24 velocities requires the specification of the possibly random output for each of 2^{24} possible configurations. Many proposals, some of which are reviewed in Section IX.A.2., have been made for the definition of such operators and the algorithms to calculate them on computers.

B. A derivation of hydrodynamics from the Boltzmann equation

In this section we derive the Euler equations and the Navier Stokes equations for the simple lattice gas with a single mass and at most one rest particle.

1. The microdynamical equation

We consider a single or multiple speed model. The velocities will still be noted $\mathbf{c}_i$ although i may now denote a multiple index. We denote by b the number of particles of all velocities. The local configuration will be a Boolean b-vector $\mathbf{n}(\mathbf{x}, t)$ depending on space and time. Since the collision rates $A(s, s')$ defined as in Section IV.A.2.b. are not 0 or 1 we need to define a field of "rate bits," denoted by $a_{ss'}$, which are equal to 1 with probability $A(s, s')$:

$$\langle a_{ss'} \rangle = A(s, s').$$

Rate bits should yield a single output for any input state s and space-time location $\mathbf{x}, t$. This is expressed by

$$\sum_{s'} a_{ss'}(\mathbf{x}, t) = 1. \tag{IV.15}$$

Then the microdynamical equation may be generalized to read

$$n_i(\mathbf{x} + \mathbf{c}_i, t + 1) = n_i(\mathbf{x}, t) + \sum_{s,s'} a_{ss'}(\mathbf{x}, t)(s'_i - s_i) \prod_j n_j(\mathbf{x}, t)^{s_j} \overline{n}_j(\mathbf{x}, t)^{\overline{s}_j}, \tag{IV.16}$$

where we use again the notation $\overline{x} = 1 - x$. In the above expression the Boolean product $P = \prod_j n_j(\mathbf{x}, t)^{s_j} \overline{n}_j(\mathbf{x}, t)^{\overline{s}_j}$ is a generalisation of the products given in (II.3) and (II.4). The product P is in fact a delta function that tests the equality of s and $\mathbf{n}$.

2. The lattice-Boltzmann equation

In Boltzmann's molecular chaos assumption particles entering a collision are not correlated before they collide. For any combination of particles $a, b, \ldots, x$ entering a

collision one assumes

$$\langle n_a n_b \cdots n_z \rangle = \langle n_a \rangle \langle n_b \rangle \cdots \langle n_z \rangle. \qquad \text{(IV.17)}$$

The rate of collision can then be determined by averaging equation (IV.16). The resulting *lattice-Boltzmann equation* has the form:

$$N_i(\mathbf{x} + \mathbf{c}_i, t+1) = N_i(\mathbf{x}, t) + \Delta_i[\mathbf{N}(\mathbf{x}, t)] \qquad \text{(IV.18)}$$

where $\mathbf{N} = (N_i)_{i=1,b}$ is the population b-vector, the elements of which are $N_i = \langle n_i \rangle$, and Δ is the Boltzmann collision operator defined by

$$\Delta_i(\mathbf{N}) = \sum_{ss'} (s'_i - s_i) A(s, s') \prod_j N_j^{s_j} \overline{N}_j^{\overline{s}_j}. \qquad \text{(IV.19)}$$

The above equation is identical to (IV.16) with the Boolean vectors n replaced by distributions N and the random rate bits $a_{ss'}$ replaced by the transitions rates $A(s, s')$. Equations (IV.18) and (IV.19) are themselves the basis for what is known as the lattice-Boltzmann method, which is briefly described in Appendix C.

3. Equilibrium distributions

The equilibrium distributions are solutions N_i^{eq} of (IV.18), uniform in time and space. They are thus the solutions of

$$\Delta_i(\mathbf{N}^{eq}) = 0. \qquad \text{(IV.20)}$$

A number of interesting results are known about these solutions under some conditions on the transition rates, which we explain below.

a. Semi-detailed balance and uniqueness A first condition is the conservation of probability, a direct consequence of equation (IV.15):

$$\sum_{s'} A(s, s') = 1 \quad \text{for all} \quad s. \qquad \text{(IV.21)}$$

The condition of *semi-detailed balance* is the symmetric condition

$$\sum_{s} A(s, s') = 1 \quad \text{for all} \quad s'. \qquad \text{(IV.22)}$$

A stronger condition would be *detailed balance*: $A(s, s') = A(s', s)$. However semi-detailed balance suffices to obtain all the results we present in what follows.

It may be proven (Frisch et al., 1987) that if the rates A are positive and obey (IV.21), as befits probabilities, and if the semi-detailed balance condition (IV.22) holds, then the solutions of (IV.20) are of the form

$$N_i^{eq} = \frac{1}{1 + \exp(h + \mathbf{q}.\mathbf{c}_i)}. \qquad \text{(IV.23)}$$

The functions h and q are arbitrary parameters that define the distributions. That the above factorized Fermi-Dirac measure is indeed a solution of equation (IV.20) may be shown easily (Frisch et al., 1987). It is also the only solution, a fact related to the H-theorem in the kinetic theory of gases (Hénon, 1987a; Gatignol, 1975). The parameters h and q are related to the observable properties of the distribution, i.e. the mass and momentum densities. From Section II., mass and momentum densities are related to N_i by:

$$\rho = \sum_i N_i^{eq} \qquad \text{(IV.24)}$$

and

$$\rho \mathbf{u} = \sum_i N_i^{eq} \mathbf{c}_i. \qquad \text{(IV.25)}$$

The expressions (IV.23), (IV.24), and (IV.25) define implicitly $h(\rho, \mathbf{u})$ and $\mathbf{q}(\rho, \mathbf{u})$ and thus the uniform distribution N_i^{eq}.

b. Low-velocity expansion It is useful to represent explicitly the equilibrium distributions as the following series in powers of the velocity u:

$$h(\rho, \mathbf{u}) = h_0 + h_2 u^2 + \mathcal{O}(u^4) \qquad \text{(IV.26)}$$

$$\mathbf{q}(\rho, \mathbf{u}) = q_1 \mathbf{u} + \mathcal{O}(u^3). \qquad \text{(IV.27)}$$

We used symmetry properties of the lattice to obtain the above expressions. Let the Fermi-Dirac function f be defined by

$$f(x) = \frac{1}{1 + e^x}. \qquad \text{(IV.28)}$$

Expanding (IV.23) we obtain

$$N_i^{eq} = f(h_0) + f'(h_0)(q_1 \mathbf{u}\cdot \mathbf{c}_i + h_2 u^2) + \frac{1}{2} f''(h_0) q_1^2 (\mathbf{u}\cdot \mathbf{c}_i)^2 + \mathcal{O}(u^3). \qquad \text{(IV.29)}$$

From (IV.24) and (IV.25) we get the coefficients of this small velocity expansion (IV.29). The expressions for a single-speed gas (i.e., no rest particles) are calculated in Frisch et al. (Frisch et al., 1987). The result is

$$N_i^{eq} = d\left[1 + \frac{D}{c^2} c_{i\alpha} u_\alpha + G(d) Q_{i\alpha\beta} u_\alpha u_\beta\right] + \mathcal{O}(u^3), \qquad \text{(IV.30)}$$

where $i = 1$ to b, summation on repeated Greek indices is implied, and

$$G(d) = \frac{D^2}{2c^4} \frac{1-2d}{1-d}, \qquad d = \rho/b, \quad \text{and} \quad Q_{i\alpha\beta} = c_{i\alpha} c_{i\beta} - \frac{c^2}{D}\delta_{\alpha\beta}. \qquad \text{(IV.31)}$$

Two symmetry properties of tensors constructed with generating vectors of the lattice were used to obtain (IV.30). We define the rth order tensor formed with the lattice directions:

$$E^{(r)}_{\alpha_1 \cdots \alpha_r} = \sum_i c_{i\alpha_1} \cdots c_{i\alpha_r}. \qquad \text{(IV.32)}$$

It is shown in Appendix A that

$$E^{(2)}_{\alpha\beta} = \frac{bc^2}{D}\delta_{\alpha\beta}, \qquad \text{(IV.33)}$$

where $c = ||\mathbf{c}_i||$. Furthermore all odd-order r-tensors of the form $\mathbf{E}^{(r)}$ vanish.

For models with a single rest particle n_{01} and $b_m = b-1$ moving particles the expressions corresponding to equation (IV.30) are obtained in a similar fashion (d'Humières and Lallemand, 1987). We use the double index notation defined above in Section IV.A.. For moving particles

$$N_{1j}^{eq} = d\left[1 + \frac{Db}{c^2 b_m} c_{1j\alpha} u_\alpha + G(d)\frac{b^2}{b_m^2}\left(Q_{1j\alpha\beta} + \frac{c^2}{Db}\delta_{\alpha\beta}\right) u_\alpha u_\beta\right] + \mathcal{O}(u^3) \qquad \text{(IV.34)}$$

for $j = 1$ to b_m , and for the rest particle

$$N_{01}^{eq} = d\left[1 - G(d)\frac{bc^2}{Db_m} u^2\right] + \mathcal{O}(u^3) \qquad \text{(IV.35)}$$

with the notations of (IV.31) and $Q_{1j\alpha\beta} = c_{1j\alpha}c_{1j\beta} - (c^2/D)\delta_{\alpha\beta}$.

4. Chapman-Enskog expansion

We now expand the solutions starting from slowly varying equilibrium fluctuations. This Chapman-Enskog expansion is (Chapman and Cowling, 1970)

$$N_i = N_i^{(0)} + N_i^{(1)} + \cdots + N_i^{(n)} + \cdots \qquad \text{(IV.36)}$$

where the 0-order term is the local equilibrium density

$$N_i^{(0)}(\mathbf{x}, t) = f[h(\rho, \mathbf{u}) + \mathbf{q}(\rho, \mathbf{u})\cdot \mathbf{c}_i], \qquad \text{(IV.37)}$$

and the densities ρ and u fluctuate in space and time. The space and time scale of these fluctuations is large, and thus derivatives—or gradients—of the $N_i^{(n)}$ are small. We introduce the idea of small gradients and also the connected multiple-time concept in a heuristic way. We postulate

$$N_i^{(k)} = \mathcal{O}(\nabla^k).$$

Time derivatives are also small with $\partial_t = \mathcal{O}(\nabla)$. Moreover it will appear useful in what follows to couple the gradient expansion of equation (IV.36) with a multiple time scale expansion. We let

$$\partial_t = \partial_{t_1} + \partial_{t_2} + \cdots \qquad \text{(IV.38)}$$

where $\partial_{t_1} = \mathcal{O}(\nabla)$, $\partial_{t_2} = \mathcal{O}(\nabla^2)$, etc.

Insertion of expansions (IV.36) and (IV.38) into the lattice-Boltzmann equation (IV.18) produces at each order b equations. It is useful to introduce the linearized Boltzmann collision operator

$$\Lambda_{ij} = \left.\frac{\partial \Delta_i}{\partial N_j}\right|_{\mathbf{N}^{(0)}}. \qquad \text{(IV.39)}$$

The above derivative is estimated at the zero-velocity equilibrium $\mathbf{N} = \mathbf{N}^{(0)} \simeq (d, d, \cdots, d)$. In Appendix B it is shown, using semi-detailed balance, that

$$\left.\frac{\partial \Delta_i}{\partial N_j}\right|_{\mathbf{N}=(d)} = \sum_{ss'} (s_i' - s_i) s_j A(s, s') d^{n-1} (1-d)^{b-n-1} \qquad \text{(IV.40)}$$

where $n = \sum_k s_k$ is the number of particles. Furthermore, using invariance under the symmetry group of the lattice, we show in Appendix B that

$$\left.\frac{\partial \Delta_i}{\partial N_j}\right|_{\mathbf{N}=(d)} = -\frac{1}{2}\sum_{ss'}(s'_i - s_i)(s'_j - s_j)A(s,s')d^{n-1}(1-d)^{b-n-1}. \qquad \text{(IV.41)}$$

Notice that the operator is symmetric.

At order 1 the following equation is obtained:

$$\partial_{t_1} N_i^{(0)} + c_{i\alpha}\partial_\alpha N_i^{(0)} = \sum_j \Lambda_{ij} N_j^{(1)}. \qquad \text{(IV.42)}$$

The operator Λ_{ij} is not in general invertible and a solvability condition needs to be satisfied in order to ensure the existence of a vector $\mathbf{N}^{(1)}$ obeying (IV.42). As is the case in multiple-scale expansions in other branches of physics, the solvability conditions are associated with a continuous symmetry of the solutions or a conservation law, as we show below. From the conservation of mass and momentum, $D+1$ vectors which are left-null-eigenvectors of Λ_{ij} are produced. These vectors are $\mathbf{1} = (1,...,1)$ and D vectors of the form $(c_{i\alpha})_{\alpha=1,...,D}$. Indeed, mass conservation implies

$$\sum_i \Delta_i(\mathbf{N}) = 0 \qquad \text{(IV.43)}$$

for any N. Hence setting $\mathbf{N} = \mathbf{N}^{eq} + \epsilon\mathbf{X}$ with X an arbitrary b-vector we find

$$\sum_{ij} \Lambda_{ij} X_j = 0 \qquad \text{(IV.44)}$$

and thus 1 is a left-null-eigenvector of Λ_{ij}. Similarly momentum conservation implies

$$\sum_i c_{i\alpha}\Delta_i(\mathbf{N}) = 0 \qquad \text{(IV.45)}$$

and hence

$$\sum_i c_{i\alpha}\Lambda_{ij} X_j = 0 \qquad \text{(IV.46)}$$

for any X. Since Λ_{ij} is symmetric, we also have the right-null-eigenvectors.

5. First order conservation laws

a. Mass conservation Multiplying (IV.42) by 1 we get the first solvability condition:

$$\partial_{t_1}\sum_i N_i^{(0)} + \partial_\beta \sum_i c_{i\beta} N_i^{(0)} = 0. \qquad \text{(IV.47)}$$

Using the definitions of mass and momentum and the distributions defined by (IV.23), (IV.24) and (IV.37) order by order, we obtain easily

$$\sum_i N_i^{(0)} = \rho \qquad \text{(IV.48)}$$

$$\sum_i N_i^{(1)} = 0, \qquad \text{(IV.49)}$$

and from (IV.25),

$$\sum_i N_i^{(0)} \mathbf{c}_i = \rho\mathbf{u} \qquad \text{(IV.50)}$$

$$\sum_i N_i^{(1)} \mathbf{c}_i = 0. \qquad \text{(IV.51)}$$

From equations (IV.47), (IV.48), and (IV.50) we obtain the mass-conservation equation

$$\partial_{t_1}\rho + \mathrm{div}\,(\rho\mathbf{u}) = 0. \qquad \text{(IV.52)}$$

b. Euler equation Multiplying (IV.42) by the eigenvectors $\mathbf{c}_{i\alpha}$ we obtain the momentum sol ability condition already indicated in Section II.B.2.:

$$\partial_{t_1}\sum_i c_{i\alpha} N_i^{(0)} + \partial_\beta \sum_i N_i^{(0)} c_{i\alpha} c_{i\beta} = 0. \qquad \text{(IV.53)}$$

At this order the momentum flux is expressed as

$$\Pi_{\alpha\beta} = \sum_i N_i^{(0)} c_{i\alpha} c_{i\beta}.$$

Expanding equation (IV.53) and using equation (IV.30) we get the momentum-conservation equation

$$\partial_{t_1}\rho u_\alpha + \partial_\beta[g(\rho)\rho u_\alpha u_\beta] = -\partial_\alpha[p(\rho, u^2)] \qquad \text{(IV.54)}$$

where we have used the following identity derived in Appendix A for hexagonal and FCHC lattices:

$$\mathrm{E}^{(4)} = \sum_i c_{i\alpha}c_{i\beta}c_{i\delta}c_{i\gamma} = \frac{b_m}{D(D+2)}(\delta_{\alpha\beta}\delta_{\gamma\delta} + \delta_{\alpha\delta}\delta_{\beta\gamma} + \delta_{\alpha\gamma}\delta_{\beta\delta}). \qquad \text{(IV.55)}$$

The relation above expresses the isotropy of $\mathrm{E}^{(4)}$. The parameter $g(\rho)$ and the pressure $p(\rho, u^2)$ are generally expressed in terms of the coefficients in the low velocity expansion (IV.30). If we restrict ourselves to at most one rest particle they may be expressed as

$$g(\rho) = \frac{D}{D+2}\frac{b}{b_m}\frac{1-2d}{1-d} \qquad \text{(IV.56)}$$

$$p(\rho, u^2) = c_s^2\rho - \rho g(\rho)\frac{c_s^2}{c^2}\left(1 + \frac{D}{2} - \frac{c^2}{2c_s^2}\right)u^2 \qquad \text{(IV.57)}$$

where $c_s^2 = \frac{b_m}{bD}c^2$ is the square of the sound speed. Equation (IV.57) is a kind of equation of state which we discuss in more detail in the next section.

The above conservation laws have been derived in the context of the Boltzmann molecular chaos assumption (IV.17). It is interesting to note however that they may be derived from the general standpoint of equilibrium statistics as done for single-speed gases (Frisch et al., 1987). Indeed the Fermi-Dirac assumption which was obtained from the Boltzmann equation may also be obtained from a quite general setting of statistical mechanics, using Gibbs distributions (Zanetti, 1989).

6. Incompressible limit

The momentum-conservation equation does not involve viscosity. It represents inviscid flow for the lattice gas and is similar to the Euler equation for gas flow with two differences: the $g(\rho)$ factor and the dependence of the pressure on the speed. These differences disappear however in the incompressible limit. The dependence of pressure on density in equation (IV.57) is a simplified equation of state. It also appears in the artificial compressibility model of Chorin (Chorin, 1967). Indeed, Chorin's finite difference algorithm for the numerical solution of the Navier Stokes equations closely resembles equations (IV.54) and (IV.57).

To see how compressibility becomes irrelevant at low fluid speeds we now assume that $\mathbf{u}$ is small with respect to the sound speed. Define the Mach number

$$\epsilon = u/c_s \qquad \text{(IV.58)}$$

where u is typical speed scale. Temam (Temam, 1969) has shown how the incompressible limit is approached in Chorin's artificial compressibility model. A discussion of the limit of small Mach number in real fluids may also be found in Tritton (Tritton, 1988). In the lattice gas context, we define a new time $t' = \epsilon t$ and a new pressure $p' = \mathbf{u}/\epsilon$. We expand velocity and density as

$$\left.\begin{aligned} \mathbf{u}(\mathbf{x}, t) &= \epsilon\mathbf{v}_1(\mathbf{x}, t) + \epsilon^3\mathbf{v}_2(\mathbf{x}, t) + \mathcal{O}(\epsilon^5) \\ \rho(\mathbf{x}, t) &= \rho_0 + \epsilon^2\rho_1(\mathbf{x}, t) + \mathcal{O}(\epsilon^4)\cdots \end{aligned}\right\} \qquad \text{(IV.59)}$$

where at first order the density ρ_0 is a constant. Inserting equation (IV.59) into (IV.54) we obtain at order ϵ^2 the following incompressible flow equations in terms of the fields $\mathbf{v}_1$ and the pressure $p' = c_s^2\rho_1$:

$$\mathrm{div}\ \mathbf{v}_1 = 0 \qquad \text{(IV.60)}$$

and

$$\partial_{t'}\mathbf{v}_1 + g(\rho_0)\mathbf{v}_1 \cdot \nabla\mathbf{v}_1 = -\frac{1}{\rho_0}\nabla p'. \qquad \text{(IV.61)}$$

Equation (IV.61) is the lattice gas equivalent of the Euler equation for incompressible flow. For a given density ρ_0 such that $g(\rho_0)$ does not vanish, define

$$\mathbf{u}' = g(\rho_0)\mathbf{v} \quad \text{and} \quad p'' = g(\rho_0)p'. \qquad \text{(IV.62)}$$

Then

$$\partial_{t'}\mathbf{u}' + \mathbf{u}' \cdot \nabla\mathbf{u}' = -\frac{1}{\rho_0}\nabla p'' \qquad \text{(IV.63)}$$

and

$$\mathrm{div}\ \mathbf{u}' = 0. \qquad \text{(IV.64)}$$

The above are the usual, Galilean-invariant, Euler equations. It is interesting to remark that the limit $\epsilon \ll 1$ is not relevant when the Reynolds number is small (Tritton, 1988) (section 5.8). Incompressibility is then obtained when

$$\epsilon^2 \ll Re \tag{IV.65}$$

when the Reynolds number $Re = uL/\nu$, L is a length scale, and ν is the shear viscosity. This remark may be of some interest in the lattice-gas context since one often finds the lattice gas to be an interesting model at low Reynolds numbers. When the limit of low Mach number is obtained by letting u vanish leaving ν fixed there is no difficulty and equation (IV.65) is satisfied. However letting ν increase at constant u might create problems.

7. Navier-Stokes equation and viscous terms

Most of the derivation that follows was done by Hénon (Hénon, 1987b) for models with a single particle speed. The extension to models with rest particles was done by d'Humières and Lallemand (d'Humières and Lallemand, 1987).

a. Inversion of first-order equation Viscosity appears at the second order of the Chapman-Enskog equation. But before we write conservations equations at second order, we need to invert (IV.42) for $\mathbf{N}^{(1)}$. To perform this inversion we need to be more specific about the operator Λ_{ij} defined in (IV.39). When there is one rest particle we find from the symmetry of the operator that

$$\Lambda = \begin{pmatrix} \lambda_{01} & (\lambda_{1j}) \\ (\lambda_{1i}) & (A_{ij}) \end{pmatrix} \tag{IV.66}$$

The coeficients λ_{kj} and A_{ij} are simply a new notation for the coefficients Λ_{ij} given by equation (IV.41). The coefficients A_{ij} involve moving particles only, λ_{01} involves the single rest particle and the λ_{1j} describe the "coupling" between the single rest particle and moving particles. These coefficients obey two sets of constraints:

- *Angle dependence.* The matrix Λ_{ij} must be invariant under the action of the symmetry group $\mathcal{G}$. In particular, the element A_{ij} may depend only on the angle $(\mathbf{c}_i, \mathbf{c}_j)$. All coefficients λ_{1j} must be equal.

- *Conservation laws.* Mass conservation expressed in equation (IV.44) implies that

$$\sum_j A_{ij} + \lambda_{11} = 0 \tag{IV.67}$$

and

$$\lambda_{01} + b_m \lambda_{11} = 0. \tag{IV.68}$$

From momentum conservation as expressed in equation (IV.46),

$$\sum_j A_{ij} \mathbf{c}_j = 0. \tag{IV.69}$$

We first insert equation (IV.30) into the left-hand-side of equation (IV.42). Using the equilibrium distribution (IV.34) and (IV.35), the first order mass-conservation law (IV.52) and the Euler equation (IV.54) itself, we find for moving particles

$$(\partial_t + c_{i\alpha}\partial_\alpha)N_i^{(0)} = \left(\frac{D}{c^2 b_m}Q_{i\alpha\beta} + \frac{1}{b b_m}\delta_{\alpha\beta}\right)\partial_\beta(\rho u_\alpha) \qquad \text{(IV.70)}$$

and for rest particles

$$\partial_t N_{01}^{(0)} = -\frac{1}{b}\mathrm{div}(\rho \mathbf{u}). \qquad \text{(IV.71)}$$

From the first-order equat.on (IV.42), the above equations (IV.70) and (IV.71) and the definition (IV.66) of the linearized operator,

$$\begin{aligned}\left(\frac{D}{c^2 b_m}Q_{i\alpha\beta} + \frac{1}{b b_m}\delta_{\alpha\beta}\right)\partial_\beta(\rho u_\alpha) &= \sum_{j=1}^{b_m} A_{ij}N_{1j}^{(1)} + \lambda_{11}N_{01}^{(1)} \\ -\frac{1}{b}\mathrm{div}(\rho \mathbf{u}) &= \lambda_{11}\sum_{j=1}^{b_m} N_{1j}^{(1)} - b_m\lambda_{11}N_{01}^{(1)}. \qquad \text{(IV.72)}\end{aligned}$$

We save a lot of effort if we first determine the general form of $\mathrm{N}^{(1)}$ from symmetry. Since the left-hand-side of (IV.72) depends on the symmetric part of $\partial_\beta(\rho u_\alpha)$, $\mathrm{N}^{(1)}$ must have the form

$$N_{1i}^{(1)} = t_{i\alpha\beta}^{(2)}\partial_\beta(\rho u_\alpha) + t_{i\alpha}^{(1)}\partial_\alpha\rho \qquad \text{(IV.73)}$$

where $t_{i\alpha\beta}^{(2)}$ is a general tensor of second order, invariant by all lattice isometries that leave c_i invariant and symmetric in the Greek indices, and $t_{i\alpha}^{(1)}$ is similarly a vector invariant by all lattice isometries that leave c_i invariant. Also $N_{01}^{(1)} = K_{\alpha\beta}\partial_\beta(\rho u_\alpha)$ where $K_{\alpha\beta}$ is a general symmetric second order tensor invariant by all lattice isometries. In Appendix A we show that such a tensor must be of the form $K_{\alpha\beta} = Y\delta_{\alpha\beta}$ where Y is an arbitrary constant. We also show in Appendex A that for all regular Bravais lattices

$$t_{i\alpha\beta}^{(2)} = \psi Q_{i\alpha\beta} - X\delta_{\alpha\beta} \qquad \text{(IV.74)}$$

and

$$t_{i\alpha}^{(1)} = T c_{i\alpha} \qquad \text{(IV.75)}$$

with arbitrary coefficients ψ, X, T. Using also the mass and momentum normalisations (IV.49) and (IV.51), we obtain $X = Y$ and $T = 0$. We then obtain

$$N_{1i}^{(1)} = \left[\psi Q_{i\alpha\beta}\partial_\beta(\rho u_\alpha) - X\delta_{\alpha\beta}\right]\partial_\beta(\rho u_\alpha) \qquad \text{(IV.76)}$$

$$N_{01}^{(1)} = b_m X\delta_{\alpha\beta}\partial_\beta(\rho u_\alpha) \qquad \text{(IV.77)}$$

where the coefficients ψ and X depend on the operator Λ. Inserting these two equations into (IV.72) and using (IV.67) we find

$$\begin{aligned}X &= \frac{1}{b^2 b_m \lambda_{11}} \\ \frac{D}{c^2 b_m}Q_{i\alpha\beta}\partial_\beta(\rho u_\alpha) &= \psi\sum_j \Lambda_{ij}Q_{j\alpha\beta}\partial_\beta(\rho u_\alpha). \qquad \text{(IV.78)}\end{aligned}$$

Thus the b_m-vector $Q_{i\alpha\beta}$ is an eigenvector of Λ and

$$\lambda = \frac{D}{c^2 b_m}\psi^{-1} \qquad \text{(IV.79)}$$

is the corresponding eigenvalue.

b. Second order equation Substituting the general Chapman-Enskog expansion (IV.36) into (IV.18) we obtain at second order

$$\begin{aligned}&\left[N_i^{(0)}(\mathbf{x}+\mathbf{c}_i, t+1) - N_i^{(0)}(\mathbf{x},t) + N_i^{(1)}(\mathbf{x}+\mathbf{c}_i, t+1) - N_i^{(1)}(\mathbf{x},t)\right]^{(2)} \qquad \text{(IV.80)} \\ &= \sum_j \Lambda_{ij}N_j^{(2)} + \tfrac{1}{2}\sum_{jk}\frac{\partial^2\Phi_i}{\partial N_j \partial N_k}N_j^{(1)}N_k^{(1)}\end{aligned}$$

where the notation $[\cdots]^{(2)}$ means that we collect all terms of order 2 in the expression in brackets. A solvability condition for momentum is obtained by multiplying equation (IV.80) by the momentum eigenvector:

$$\sum_i \left[N_i^{(0)}(\mathbf{x}+\mathbf{c}_i, t+1) - N_i^{(0)}(\mathbf{x},t) + N_i^{(1)}(\mathbf{x}+\mathbf{c}_i, t+1) - N_i^{(1)}(\mathbf{x},t)\right]^{(2)} c_{i\alpha} = 0. \qquad \text{(IV.81)}$$

After some manipulation, using the first order momentum balance (IV.53) and the momentum normalisation condition (IV.51) one obtains

$$\begin{aligned}\partial_{t_0}\rho u_\alpha + \frac{1}{2}\partial_{t_1}\sum_i c_{i\alpha}(\partial_{t_1} &+ c_{i\beta}\partial_\beta)N_i^{(0)} + \frac{1}{2}\partial_\beta\sum_i c_{i\alpha}c_{i\beta}(\partial_{t_1} + c_{i\gamma}\partial_\gamma)N_i^{(0)} \\ &+\partial_\beta\sum_i c_{i\alpha}c_{i\beta}N_i^{(1)} = 0. \qquad \text{(IV.82)}\end{aligned}$$

From the expansion of the streaming operator (IV.70) and the first order in the Chapman-Enskog expansion, equation (IV.42), we obtain

$$\partial_{t_2}\rho u_\alpha + \frac{1}{2}\partial_{t_1}\sum_i \Lambda_{ij}c_{i\alpha}N_j^{(1)} + \frac{1}{2}\partial_\beta\sum_i c_{i\alpha}c_{i\beta}\left(\frac{D}{c^2 b_m}Q_{i\gamma\delta}+\frac{1}{b b_m}\delta_{\gamma\delta}\right)\partial_\gamma(\rho u_\delta) + \partial_\beta\sum_i c_{i\alpha}c_{i\beta}N_i^{(1)} = 0. \quad \text{(IV.83)}$$

Then, using the existence of a null eigenvector for momentum expressed in (IV.46) and the fourth order tensor expression (IV.55) again, and inserting the low velocity expansion (IV.34) and (IV.35) of $\mathbf{N}_i^{(0)}$ in the above equation, we obtain

$$\partial_{t_2}\rho u_\alpha = \partial_\beta\left\{\nu_1[\partial_\beta(\rho u_\alpha)+\partial_\alpha(\rho u_\beta)]\right\} + \partial_\alpha[\nu_2 \mathrm{div}(\rho \mathbf{u})] \quad \text{(IV.84)}$$

where

$$\nu_1 = -\frac{b_m c^4}{D(D+2)}\psi - \frac{c^2}{2(D+2)} \quad \text{(IV.85)}$$

$$\nu_2 = \frac{b_m c^2}{D}X + \frac{2b_m c^4}{D^2(D+2)}\psi + \frac{c^2}{D(D+2)} - \frac{c^2}{2bD}. \quad \text{(IV.86)}$$

A similar calculation may be performed starting from the mass solvability condition. Multiplying (IV.80) by 1 yields

$$\partial_{t_2}\rho = 0. \quad \text{(IV.87)}$$

Adding (IV.84) to the Euler equation (IV.54) and using the mutiple time scale expansion (IV.38) we get the full Navier Stokes equations

$$\partial_t\rho u_\alpha + \partial_\beta[g(\rho)\rho u_\alpha u_\beta] = -\partial_\alpha[p(\rho,u^2)] + \partial_\beta\left\{\nu_1[\partial_\beta(\rho u_\alpha)+\partial_\alpha(\rho u_\beta)]\right\} + \partial_\alpha[\nu_2\mathrm{div}(\rho\mathbf{u})] \quad \text{(IV.88)}$$

and from the first and second order of mass conservation, equations (IV.52) and (IV.87), we obtain the continuity equation

$$\partial_t\rho + \mathrm{div}\,(\rho\mathbf{u}) = 0. \quad \text{(IV.89)}$$

Equations (IV.88) and (IV.89) are one of the main results of lattice gas theory. They are close to the Galilean invariant compressible equations for fluid flow (Landau and

Lifshits, 1959a; Tritton, 1988). In the low Mach number limit we can perform the same changes of variable as in Section IV.B.6. and obtain the incompressible Navier-Stokes equations. The form of these equations is universal. It does not depend on the collision operator, except through the parameters ψ and X. These equations hold for all the lattice geometries whose symmetry properties imply isotropy of 4th order tensors.

8. Viscosity

a. Expression of the viscosity coefficients From equation (IV.79) and (IV.85)

$$\nu_1 = -\frac{c^2}{\lambda(D+2)} - \frac{c^2}{2(D+2)}. \quad \text{(IV.90)}$$

From equation (IV.78), λ may be expressed as

$$\lambda = \frac{\sum_i Q_{i\alpha\beta}^2}{\sum_{ij} Q_{i\alpha\beta}\Lambda_{ij}Q_{j\alpha\beta}}. \quad \text{(IV.91)}$$

After some calculations detailed in Appendix B, one obtains

$$\lambda = \frac{b_m c^4(D-1)}{D\sum_{s,s'}A(s,s')d^{n-1}\overline{d}^{2-n-1}(Y'_{\alpha\beta}-Y_{\alpha\beta})Y_{\alpha\beta}} \quad \text{(IV.92)}$$

where $Y_{\alpha\beta}=\sum_i s_i Q_{i\alpha\beta}$, $Y'_{\alpha\beta}=\sum_i s'_i Q_{i\alpha\beta}$, and $n=\sum_k s_k$. Several transformations of equation (IV.91) may be found in Hénon (Hénon, 1987b). In particular it may be shown (Hénon, 1987b) that the shear viscosity ν is always positive. More elaborate expressions of the viscosity also allow to attempt minimisation of ν, a useful endeavor when the objective is to reach high Reynolds numbers.

The values of the shear viscosity for several classical models are summarized in Table 1.

b. Comparison of viscous equations with simulations We have described the issue of the general comparison of the viscous equations (IV.88) and (IV.89) with simulations of the lattice gas in Section II.C.. Here we only discuss simulations aimed at the measurement of viscosity. One possible method is the Poiseuille viscometer

	FHP-I	FHP-III	Random 7-velocity
ρ	$6d$	$7d$	7d
c_s	$1/\sqrt{2}$	$\sqrt{3}/\sqrt{7}$	$\sqrt{3}/\sqrt{7}$
ν_1	$\frac{1}{12}\frac{1}{d(1-d)^3} - \frac{1}{8}$	$\frac{1}{28}\frac{1}{d(1-d)}\frac{1}{1-8d(1-d)/7} - \frac{1}{8}$	—
$\nu_1(d=0.3)$	0.685	0.0988	0.236
$\nu_1(d=0.5)$	1.21	0.0750	0.191
$\nu_1(d=0.7)$	4 28	0.0988	0.236

Table 1. Viscosity values for the simple models described in Section IV.A.2..

experiment of McNamara, Kadanoff, and Zanetti described in Section IX.A.1.b.. The measured viscosities agree within a few percent with the predicted ones. However the difference is outside of the error bars. In fact viscosity diverges logarithmically with length in 2 dimensions, a fact that precludes any agreement with the Boltzmann values. We shall discuss this divergence further in Section IV.C.

Another type of measurement may be performed using decaying shear waves (d'Humières and Lallemand, 1987). Because the shear waves eventually decay to below noise levels, such experiments cannot be sustained indefinitely and are in our opinion less accurate than Poiseuille viscometers. However they have the advantage that forcing is not required.

C. Statistical description beyond the Boltzmann approximation

We now review the statistical description of a general lattice gas. The statistical description has several levels. At the level of the Liouville equation we look for an invariant or equilibrium measure that would generalize the Fermi-Dirac distribution. The description of that measure will be made following the ideas of Hardy, de Pazzis

and Pomeau (Hardy et al., 1973), Zanetti (Zanetti, 1989) and Bernardin (Bernardin, 1992).

1. Liouville equation

As in Section IV.A.1., let $\mathcal{L}$ be the lattice, considered either infinite in space or of very large volume. A configuration over the entire set $\mathcal{L}$ is a function $\mathbf{n}(\mathbf{x})$ of lattice position $\mathbf{x}$. We shall write functions $\mathbf{n}(\cdot)$, $\mathbf{m}(\cdot)$, etc., to distinguish them from their value at $\mathbf{x}$. For instance $\mathbf{n}(\cdot, t)$ is the configuration of the model at time t. It is of some interest to study in detail the evolution of $\mathbf{n}(\cdot, t)$ as given by the microdynamical equation (IV.16). It is equivalent to the composition of two operators: a streaming operator $\mathcal{S}$ and a collision operator $\mathcal{C}$. Streaming is simply the propagation of particles. The distribution $\mathbf{n}(\cdot)$ yields $\mathbf{m}(\cdot) = \mathcal{S}\mathbf{n}(\cdot)$ if

$$m_i(\mathbf{x} + \mathbf{c}_i) = n_i(\mathbf{x}). \tag{IV.93}$$

The collision operator is defined by $\mathbf{m}(\cdot) = \mathcal{C}\mathbf{n}(\cdot)$ and

$$m_i(\mathbf{x}) = n_i(\mathbf{x}) + \sum_{s,s'} a_{ss'}(\mathbf{x})(s'_i - s_i) \prod_j n_j^{s_j}(\mathbf{x}) \bar{n}_j^{\bar{s}_j}(\mathbf{x}). \tag{IV.94}$$

Obviously the collision operator $\mathcal{C}$ is a random operator. Let $\mathcal{A}(X \to Y)$ be the transition rate corresponding to the random operator $\mathcal{E} = \mathcal{C}\mathcal{S}$. The explicit expression of these transition rates is cumbersome and does not play a rôle in the discussion that follows. The time dependent function $P(\cdot, t)$ gives the probability $P(\mathbf{n}(\cdot), t)$ of observing configuration $\mathbf{n}(\cdot)$ at time t. The function $P(\cdot, t)$ is called the *state* of the lattice in the classical terminology of statistical physics (Kadanoff and Swift, 1968) and should not be confused with a configuration $\mathbf{n}(\cdot)$. The state obeys a Liouville or Chapman-Kolmogorov equation (Frisch et al., 1987; Zanetti, 1989):

$$P[\mathbf{n}(\cdot), t+1] = \sum_{\mathbf{m}(\cdot)} \mathcal{A}(\mathbf{m}(\cdot) \to \mathbf{n}(\cdot)) P[\mathbf{m}(\cdot), t]. \tag{IV.95}$$

2. Equilibrium states

The invariant measures, or steady distributions, are fixed points P of the evolution (IV.95). It is not known in general what the invariant measures are (Hardy et al., 1973; Bernardin, 1992) When the quantities $J_i[\mathbf{m}(\cdot)]$ left invariant by the microdynamics are known and the microscopic motion is reversible a standard conjecture of statistical mechanics (Landau and Lifshitz, 1986) is that the relevant fixed points, called *equilibrium states*, are the Gibbs distributions

$$P = \frac{\exp\{-\sum_i \mu_i J_i[\mathbf{n}(\cdot)]\}}{Z}, \tag{IV.96}$$

where the *partition function*

$$Z = \sum_{\mathbf{m}(\cdot)} \exp\left\{\sum_i -\mu_i J_i[\mathbf{m}(\cdot)]\right\} \tag{IV.97}$$

and the μ_i are chemical potentials associated with the J_i.

In standard models such as FHP, $D+1$ invariant densities have been *built* into the system; i.e.,

$$J_0[\mathbf{n}(\cdot)] = \sum_{\mathbf{x}\in\mathcal{L}} n[\mathbf{n}(\mathbf{x})], \quad \text{and} \quad J_\alpha[\mathbf{n}(\cdot)] = \sum_{\mathbf{x}\in\mathcal{L}} g_\alpha(\mathbf{n}(\mathbf{x})) \quad \text{where} \quad 1 \le \alpha \le D \tag{IV.98}$$

where the particle number n and the momentum $\mathbf{g}$ are defined by

$$n(\mathbf{n}) = \sum_i n_i, \qquad \text{and} \qquad \mathbf{g}(\mathbf{n}) = \sum_i n_i \mathbf{c}_i. \tag{IV.99}$$

A remarkable fact shared by all lattice-gas automata with semi-detailed balance is that they possess a factorized invariant measure. When the only invariant densities are mass and momentum, we find the same Fermi-Dirac distribution as in Section IV.B. Indeed, by substituting the invariants of equation (IV.98) in the Gibbs distribution (IV.96), we find

$$P(X) = \prod_{\mathbf{x}\in\mathcal{L}} \prod_{i=1}^{b} f(h + \mathbf{q}.\mathbf{c}_i)^{n_i(\mathbf{x},t)}[1 - f(h + \mathbf{q}.\mathbf{c}_i)]^{1-n_i(\mathbf{x},t)} \tag{IV.100}$$

where f is defined as in equation (IV.28) above.

3. Spurious invariants

We shall call *spurious invariants* those invariants J_i which appear in the probabilistic Liouville dynamics (IV.95) but were not built intentionally into the model. It has long been known, for instance, that the model of Hardy, de Pazzis and Pomeau (Hardy et al., 1973) conserved the total momentum on each lattice line, creating infinitely many spurious invariants. The FHP model has 3 staggered time-dependent invariants of the form (Zanetti, 1989)

$$J_{D+k} = \sum_{\mathbf{x}} (-1)^t (-1)^{(\mathbf{b}_k.\mathbf{x})} \mathbf{g}(\mathbf{x}).\mathbf{c}_k^\perp \tag{IV.101}$$

for $k = 1$ to 3 where $\mathbf{c}_k^\perp$ is the unit vector orthogonal to $\mathbf{c}_k$ and $\mathbf{b}_k$ is the reciprocal vector $\mathbf{b}_k = 2/\sqrt{3}\mathbf{c}_k^\perp$. That these expressions are in fact invariant may be verified by inspection. Notice that the local expression $\mathbf{g}(\mathbf{x})\cdot\mathbf{c}_k^\perp$ is invariant by the local collision operator. The global expression in (IV.101) is also invariant by the streaming operator S, as easily seen by inspection. Thus the spurious invariants J_k are invariant by the composition of streaming and collision.

These invariants may be given the following meaning: the momentum projected on directions perpendicular to a lattice line, i.e. $\mathbf{g}(\mathbf{x})\cdot\mathbf{c}_k^\perp$, may be split between even numbered and odd numbered lines. The odd-line momentum is exchanged with the even-line momentum at each time step.

Following the accidental discovery of the staggered invariants (IV.101) several studies were made to find an exhaustive list of invariants. Systematic numerical searches for linear invariants have been performed (d'Humieres et al., 1989; d'Humieres et al., 1990; Zanetti, 1991). Staggered invariants were found in multiple-velocity square-lattice models (Brito and Ernst, 1991a) and in the FCHC model (Brito et al., 1991). Invariants may have period higher than 2: counting period 3 invariants, 11 invariants were found in the 4-bit model of Qian et al. (Qian et al., 1992a). The decomposition into streaming and collision operator used above is the source of efficient algorithms for invariant search (d'Humières, pers. comm.).

4. Euler equations and Boltzmann approximation

In a manner similar to the derivation from the Boltzmann equation in Section IV.B., a Chapman-Enskog expansion of the densities $N_i = \langle n_i \rangle$ may be performed. The first-order equations are obtained directly by substitution of the expansion given by equation (IV.36) in the mass and momentum conservation equations. When the spurious invariants are all of chemical potential 0 or somehow destroyed[2] the zeroth order distribution is the Fermi-Dirac distribution of equation (IV.37) and Euler equations identical to those of Section IV.B. are obtained. Thus the Euler equations are really independant of the Boltzmann approximation.

A description of hydrodynamics that includes staggered invariants was given by Zanetti (Zanetti, 1989). The standard hydrodynamic description, however, excludes staggered invariants. The consensus among practioners is that this exclusion does not affect is relevance. Staggered invariants are not created by hydrodynamic modes. If they initially have zero density they will remain there, except when small scale excitations are present in the system such as strong shock waves or special boundaries (Cornubert, 1991).

5. Estimations of viscosity beyond the Boltzmann approximation

In classical kinetic theory, viscosity may be related to fluctuations of the velocity by so-called Green-Kubo relations. For a simple fluid the shear viscosity takes the form (Hansen, 1976)

$$\nu = \frac{\beta}{\rho m} \int_0^\infty \langle \sigma^{xy}(t) \sigma^{xy}(0) \rangle_{eq} dt \qquad \text{(IV.102)}$$

where β is the inverse temperature, m the molecular mass, ρ the mass density, $\sigma^{xy}(t)$ the xy component of the microscopic momentum flux tensor related to a given particle at time t. The symbol $\langle \cdot \rangle_{eq}$ means that fluctuations are taken in equilibrium.

Such a relation was obtained by Rivet (Rivet, 1987) in the lattice-gas context.

[2] No known model is so far free of spurious invariants.

This formalism may be a starting point for the computations of exact expressions for the viscosity. Another issue of interest is the behavior of long-time correlations of the form $C_{ij}(\mathbf{x}, t) = \langle n_i(0,0) n_j(\mathbf{x}, t) \rangle$, and in particular the appearance of long-time tails of the form $C(\mathbf{x}(t), t) \sim t^{-\alpha}$, where $\mathbf{x}(t)$ is the trajectory of a particle. The study of transport coefficients and of these correlations has motivated a lot of work in lattice gases since the earliest times (Kadanoff and Swift, 1968; Hardy et al., 1973; Hardy et al., 1976; Kadanoff et al., 1989; Frenkel and Ernst, 1989; Frenkel, 1990; Ernst and Dufty, 1990; Van der Hoef and Frenkel, 1990; Naitoh et al., 1990; Noullez and Boon, 1991; Van der Hoef and Frenkel, 1991; Van der Hoef and Frenkel, 1991; Naitoh and Ernst, 1991; Naitoh et al., 1991; Brito and Ernst, 1991b; Ernst, 1991). We cannot review this topic here. However we note that there is a remaining quantitative disagreement between the kinds of mode-coupling theories used and the very precise numerical experiments performed in the study of long-time tails.

Methods for the construction of systematic corrections to the Boltzmann values of the viscosity have been proposed. A *ring kinetic theory* expresses time correlation functions in terms of ring-collision integrals (Kirkpatrick and Ernst, 1991). The results for long time reduce to those found from the phenomenological mode-coupling theory. Other diagrammatic expansions also give autocorrelation functions (Taylor and Boghosian, 1992). They are found to improve the prediction of transport coefficients for some simple one dimensional models.

V. On three levels: introduction to phase separating systems

Phase separation occurs when the mixed state of a mixture is unstable, so that its components spontaneously segregate into bulk phases composed primarily of one species or the other (Gunton et al., 1983). If the instability results from a finite, localized perturbation of concentration in the mixture, it is known as *nucleation*. If instead the perturbation is infinitesimal in amplitude, not localized, and of sufficiently long wavelength, the instability is known as *spinodal decomposition*.

In the remainder of this review we concentrate on the statistical mechanics and hydrodynamics of the lattice-gas models of phase separation introduced in Section III.. To set the stage for what follows, we first briefly review certain aspects of phase separation, and classify them according to the spatial scale at which they act: macroscopic, mesoscopic, or microscopic.

At a macroscopic scale and within contiguous domains, phase separation may be described by the partial-differential equations of continuum mechanics. An additional complexity, however, is brought to the problem by the presence of interfaces separating each phase from the other. Continuum mechanics considers these interfaces to be vanishingly thin, and constructs *jump conditions* to connect solutions of the partial-differential equations across the interfaces. These jump conditions are the postulated basis for many applications of the fluid dynamics of multiphase systems.

At a smaller scale interfaces have a finite thickness. This thickness, however, is assumed to be much larger than the microscopic length scale of the system. Thus the fluid behavior may still be described by continuum equations. A simple example of such an approach is the Ginzburg-Landau model for phase transitions or the Cahn-Hilliard equation for phase separation in a binary mixture (Gunton et al., 1983). Such a level of description is intermediary between continuum mechanics and microscopic modelling and may appropriately be deemed mesoscopic.

At a yet smaller scale the behavior of the system is that of a collection of discrete particles. At this level of description we find the two lattice-gas models of phase separation introduced in section III.. Although describing the microscopic dynamics of these models is one of the main objectives of this review, it is nevertheless useful to discuss the connection of these models to the two other levels of description described above. The merit of the connection to the macroscopic, continuum-mechanics approach is obvious. Continuum mechanics is widely verified experimentally and may be seen as the expression of the fundamental conservation laws and symmetries of classical physics. On the other hand the usefulness of the connection to the mesoscopic level is more subtle. At this mesoscopic scale, we can most clearly describe our discrete models as analogous to bifurcating dynamical systems. Just as in such systems, our discrete particle models may fall into either the *potential* or *non-potential* category. In the potential category we find those systems that derive from a thermodynamic potential and obey classical thermodynamic rules for phase transitions. In the non-potential category we find systems that may not obey some of these rules. The applicability of such concepts for partial-differential equations is well demonstrated by the theory of instabilities in extended systems out of equilibrium (Manneville, 1990).

In what follows we discuss the three levels of description, beginning with the largest scale and ending with the smallest.

A. Macroscopic description: hydrodynamics with jump conditions

In this section we recall how thin interfaces are classically described in the continuum mechanics of two-phase flow (Drew, 1983). For simplicity we consider a mixture of two phases, noted 1 and 2, with densities ρ_1 and ρ_2. We will assume for the moment that no change of phase is permitted. The vector n is the normal to the interface.

Then we expect the Navier-Stokes equation,

$$\partial_t u_\alpha + u_\alpha \partial_\beta u_\beta = -\frac{1}{\rho}\partial_\alpha p(\rho) + \partial_\beta S_{\alpha\beta} \tag{V.1}$$

to be valid in the bulk of each phase, where the viscous stress tensor is

$$S_{\alpha\beta} = \eta(\partial_\alpha u_\beta + \partial_\beta u_\alpha) + \zeta \mathrm{div}\, u\, \delta_{\alpha\beta}, \tag{V.2}$$

where for simplicity we have taken the bulk and shear viscosities in each phase to be equal. The mass conservation or continuity equation (II.12) is also obeyed in each phase. On the interfaces between the two fluids a number of fields obey *jump conditions*. We write $[X] = X_1 - X_2$ to signify the difference between the limit of quantity X when the interface is approached from side 1 and the corresponding limit when the interface is approached from side 2. The jump conditions are then:

1. Fluid velocities are equal:

$$[\mathbf{u}] = 0. \tag{V.3}$$

2. Interface velocity is equal to the fluid velocity. This means that

$$\mathbf{u}_i \cdot \mathbf{n} = V_I, \tag{V.4}$$

   where V_I is the velocity of the interface in the direction of its normal $\mathbf{n}$.

3. Momentum flux across the interface is continuous except for the capillary force term:

$$[p\delta_{\alpha\beta} + S_{\alpha\beta}] = n_\alpha n_\beta \sigma \kappa. \tag{V.5}$$

   Here σ is the capillary or surface tension, and $\kappa = 1/R_1 + 1/R_2$ is the curvature.

A requirement for consistency (in the sense used in numerical analysis) of a lattice-gas scheme for the simulation of multiphase flow is that on the large scale it obeys the above set of equations. Although such consistency may not always be achieved in lattice-gas models, we emphasise that this consistency may not be necessary (or indeed desirable) if one's objective is to gain insight into phase transitions in such discrete systems.

B. Mesoscopic description: continuum models of phase transitions

In this section we discuss phase-separating systems at a mesoscopic scale where interfaces are no longer of negligible width. Nevertheless, we still work with continuum models, under the assumption that interfaces are much wider than the characteristic microscopic scale. After first introducing the the classical models of thermodynamics and statistical physics for phase-transition dynamics, we describe two analog continuum models, one for binary fluids and the other for a liquid-gas transition.

1. Mesoscopic theory for binary mixtures

Our goal in this brief section is to demonstrate, via a linear theory due originally to Cahn and Hilliard, the origin of the instability that leads to spinodal decomposition in real systems (Gunton et al., 1983). As is customary in such formulations, we begin with a definition of a free-energy density $f(\theta)$, where $\theta(\mathbf{x})$ is a concentration field that may vary in both space and time. Considerations of symmetry lead to the following expression for a double-well potential (Landau and Lifshitz, 1986):

$$f(\theta) = -h_2\theta^2 + h_4\theta^4, \tag{V.6}$$

where $h_4 > 0$ and, for $T < T_c$, $h_2 > 0$. The free energy F of the system is then the integral over space of the sum of f and an additional spatial term chosen to favor smooth concentration fields. This results in the Ginsburg-Landau free-energy functional

$$F[\theta] = \int d\mathbf{x}[\xi_1^2|\nabla\theta|^2 + f(\theta)], \tag{V.7}$$

where ξ_1 is a parameter proportional to the width of interfaces. A dynamical model for the evolution of the concentration field is the continuity equation

$$\frac{\partial\theta(\mathbf{x},t)}{\partial t} = -\nabla\cdot\mathbf{J}(\mathbf{x},t), \tag{V.8}$$

coupled with an expression for the current J of concentration,

$$\mathrm{J}(\mathrm{x}) = -M\nabla\frac{\delta F}{\delta\theta(\mathrm{x})} = M\nabla\left(-\xi_1^2\nabla^2\theta + \frac{\partial f}{\partial\theta}\right), \tag{V.9}$$

where $M > 0$ is a mobility. Substitution of equation (V.9) into equation (V.8) then yields the nonlinear equation we shall call Model A (Hohenberg and Halperin, 1977):

$$\frac{\partial\theta(\mathrm{x})}{\partial t} = M\nabla^2\left(-\xi_1^2\nabla^2\theta + \frac{\partial f}{\partial\theta}\right). \tag{V.10}$$

To determine the condition under which spinodal decomposition is initiated, we consider the evolution of small perturbations $\tilde{\theta}(\mathrm{x})$ to the average concentration field θ_0. Thus we write

$$\theta(\mathrm{x}) = \theta_0 + \tilde{\theta}(\mathrm{x}) \tag{V.11}$$

and linearize equation (V.10) about θ_0 to obtain

$$\frac{\partial\tilde{\theta}(\mathrm{x})}{\partial t} = M\nabla^2\left[-\xi_1^2\nabla^2 + \left(\frac{\partial^2 f}{\partial\theta^2}\right)_{\theta_0}\right]\tilde{\theta}(\mathrm{x}). \tag{V.12}$$

In the initial stages of spinodal decomposition, one expects $\tilde{\theta}$ to be everywhere small. Thus, for sufficiently long wavelengths, the first term in the brackets above can be neglected, and we obtain the diffusion equation

$$\frac{\partial\tilde{\theta}(\mathrm{x})}{\partial t} = D\nabla^2\tilde{\theta}(\mathrm{x}), \tag{V.13}$$

where the diffusion coefficient is given by

$$D = M\left(\frac{\partial^2 f}{\partial\theta^2}\right)_{\theta_0}. \tag{V.14}$$

Since D can be either positive or negative, we see that the initial stages of spinodal decomposition (i.e., the growth of the fluctuations $\tilde{\theta}$) may be characterised by "uphill diffusion," which is possible everywhere inside the spinodal curve defined by the locus of points for which $\partial^2 f/\partial\theta^2 = 0$. We return to this point in Section VIII.B..

2. A non-potential model

In the context of a microscopically-irreversible lattice-gas model, there is no compelling argument for the existence of a thermodynamical potential. Thus we now generalize equation (V.9) to illustrate an example of a non-potential model. We keep the symmetries of the problem intact, and still limit ourselves to second order in gradient. The resulting model, which we call Model A', is

$$\mathrm{J} = \nabla\left[f(\theta) + \xi_1^2\nabla^2\theta + \xi_2^2(\nabla\theta)^2\right]. \tag{V.15}$$

For an equilibrium interface, J = 0; if this interface is perpendicular to the z-direction then

$$f(\theta) + \xi_1^2\frac{\partial^2\theta}{\partial z^2} + \xi_2^2\left(\frac{\partial\theta}{\partial z}\right)^2 = f_0, \tag{V.16}$$

where f_0 is the limiting value of $f(\theta)$ for $\theta \to \pm\infty$. For $\xi_2 = 0$ this model derives from the potential F, and may be integrated once. In this case we obtain a pair of equations that implicitly define θ_1 and θ_2, the equilibrium concentrations in phase 1 and 2, respectively:

$$\int_{\theta_1}^{\theta_2} d\theta\,[f(\theta) - f(\theta_1)] = 0, \qquad f(\theta_1) = f(\theta_2). \tag{V.17}$$

However, if $\xi_2 \neq 0$ then the above construction fails.

Using the terminology of dissipative dynamical systems (Manneville, 1990; Pomeau, 1986), we call "potential" those systems like Model A, equation (V.10), which may be obtained from a thermodynamic potential, while we refer to the others as "non-potential." For some functional F of a field ϕ, potential models satisfy

$$\frac{\partial\Phi}{\partial t} = -\frac{\delta F}{\delta\Phi}, \tag{V.18}$$

whereas non-potential models have no such evolution. There is very little numerical evidence as to which class our phase-separating automata belong. It would however be a remarkable accident if they fell into the potential class. We note that the non-potential Model A' (equation (V.15)) is related to a model recently explored by

Nozières and Quemada (Nozières and Quemada, 1986) in the context of diffusion of a collection of blood cells. In this nonequilibrium system, a macroscopically fluctuating suspension in a liquid, one expects equilibrium thermodynamical constructions to fail. However a surviving feature of such hydrodynamical systems is the uniqueness of the equilibrium interfaces.

3. Mesoscopic model of a liquid-gas transition

Models A and A' do not fully describe binary fluid mixtures since they lack a momentum balance equation. It is, however, relatively easy to write an isothermal model for a liquid-gas transition that conserves both mass and momentum. This model, which we call Model B, reads as follows:

$$\partial_t \rho u_\alpha + \partial_\beta \rho u_\alpha u_\beta = -\partial_\beta P_{\alpha\beta}[\rho] + \partial_\beta S_{\alpha\beta} \tag{V.19}$$

Here $S_{\alpha\beta}$ is the Navier-Stokes viscous stress tensor, $P_{\alpha\beta}[\rho]$ is a tensor, yielding anisotropic constraints inside interfaces as discussed in Section VI.. It is a functional of ρ that is given by

$$P_{\alpha\beta}[\rho] = \left[p_0(\rho) + \xi_1^2 \nabla^2 \rho + \xi^2 (\nabla\rho)^2\right] \delta_{\alpha\beta} - \xi_3^2 \left[(\nabla\rho)^2 \delta_{\alpha\beta} - \partial_\alpha \rho \partial_\beta \rho\right], \tag{V.20}$$

where the ξ_i are arbitrary coefficients. Coefficient ξ_3^2 has been added to allow a non-vanishing surface tension for the model, but will not be needed in the following. The equation of state is given by $p_0(\rho)$. In analogy with the free-energy density given by equation (V.6), we may consider a simple equation of state of the form $p_0(\rho) = -h_2(\rho - \rho_c) + h_4(\rho - \rho_c)^3$ where ρ_c is some critical density. The momentum equation (V.19) is of course coupled to a mass conservation equation.

Consider a flat equilibrium interface, parallel to the direction x. Let ρ depend on z alone. Then

$$\partial_z \left[p_0(\rho) + \xi_1^2 \frac{\partial^2 \rho}{\partial z^2} + \xi_2 \left(\frac{\partial \rho}{\partial z}\right)^2\right] = 0. \tag{V.21}$$

The system may be integrated once to yield

$$p^{eq} = p_0(\rho) + \xi_1^2 \frac{\partial^2 \rho}{\partial z^2} + \xi_2 \left(\frac{\partial \rho}{\partial z}\right)^2, \tag{V.22}$$

where p^{eq} is the equilibrium pressure. In a single interface solution we expect $\frac{\partial \rho}{\partial z} \to 0$ as $z \to 0$. We call ρ_1 and ρ_2 the densities of the two phases and we look for solutions such that $\rho(z) \to \rho_1$ when $z \to -\infty$ and $\rho(z) \to \rho_2$ when $z \to +\infty$. When $\xi_2 = 0$ we may integrate once to find

$$\int_{\rho_1}^{\rho_2} [p_0(\rho) - p^{eq}]\, d\rho = 0. \tag{V.23}$$

This equation is the analog of the Maxwell construction for Model B. If we define a "free energy" $f(\rho) = \int_0^\rho p(\rho')d\rho' - p(\rho)\rho$, then the coexistence condition is

$$f(\rho_1) = f(\rho_2) \tag{V.24}$$

together with the mechanical equilibrium condition equivalent to equation (V.5):

$$p(\rho_1) = p(\rho_2) = p^{eq}. \tag{V.25}$$

On the other hand, if $\xi_2 \neq 0$ then the system cannot be integrated as simply and it is non-potential. However there is still a single equilibrium solution.

C. Microscopic models

In this section we provide detailed definitions of the two phase-separation models introduced in Section III.. Then, in Sections VI., VII., and VIII., we consider the relation of these microscopic models to the macroscopic and mesoscopic theories described above.

1. Liquid-gas models

a. Minimal model In Section III.B. we defined a liquid-gas model in two-dimensions with interactions between sites. The model can be generalized to any dimension easily. To perform this generalisation we use the following notational trick. We let the

indices i and $-i$ denote opposite pairs of velocities, such that $\mathbf{c}_i = -\mathbf{c}_{-i}$. It is also useful to define a probabilistic rate of interaction. We define the interaction condition in terms of Boolean variables

$$\gamma_i = a'_i(\mathbf{x}, \mathbf{x} + r\mathbf{c}_i, t)\bar{n}'_i(\mathbf{x})n'_{-i}(\mathbf{x})n'_i(\mathbf{x} + r\mathbf{c}_i)\bar{n}'_{-i}(\mathbf{x} + r\mathbf{c}_i), \qquad (V.26)$$

where $\mathbf{n}'$ is the distribution of particles after the collision step, and $a'_i(\mathbf{x}, \mathbf{x} + r\mathbf{c}_i, t)$ is a random Boolean variable controlling the rate of interaction. We shall assume it corresponds to a uniform interaction rate $\mu = \langle a'_i(\mathbf{x}, \mathbf{x} + r\mathbf{c}_i, t)\rangle$. The microdynamical equation of the lattice gas is then

$$n_i(\mathbf{x} + \mathbf{c}_i, t + 1) = n'_i(\mathbf{x}, t) + \gamma_i - \gamma_{-i}. \qquad (V.27)$$

This modification of the basic FHP model is analogous to the addition of an attractive force between distant particles. This attraction occurs only at a fixed distance r. If we consider a one-dimensional version of the liquid-gas model, then the corresponding interaction potential between particles is akin to a square-well potential. In that sense the liquid-gas model is a discrete analog of the classical molecular-dynamics model of hard spheres in a square well.

b. Other liquid-gas models To date, most numerical studies with liquid-gas models have been done with more complex versions of the model stated above. In these models, transverse momentum (parallel to $\mathbf{x}, \mathbf{x} + r\mathbf{c}_i$) is exchanged between two sites by redistributing particles in a number of ways. Figure 15 shows a five-step model (Appert and Zaleski, 1990) in which interactions exchange the position of particles in full and dotted lines. These interactions imply a form of competition between interacting pairs. While in the minimal model calculations of γ_i and n'_i could be done in parallel, it must now be decided in which order the pairs must be investigated. This is a rather annoying complication of the model, which moreover is not as easily tractable as the minimal model.

Yet another model is the *maximal* model in which the largest possible amount of momentum is exchanged between sites (Appert et al., 1991). This model has the

advantage of displaying a liquid-gas transition in 2D at $r_c \simeq 2.8$, a relatively low value.

2. Immiscible lattice gas

Here we describe the detailed microdynamics of the immiscible lattice gas model, introduced earlier in Section III.A.. Analogous to our definition of a state in a single-component lattice gas, for immiscible lattice gases we define the 14-bit state

$$s = \{r, b\} = \{r_0, r_1, \ldots, r_6, b_0, b_1, \ldots, b_6\}, \qquad (V.28)$$

where, as described in Section III.A., bits with indices 0 represent rest particles, and higher indices refer to the lattice directions $\mathbf{c}_i$ given by equation (II.2). Since the red bit r_i and the blue bit b_i cannot both equal one for the same i, we have

$$n_i = r_i + b_i \qquad (V.29)$$

to indicate the presence of either a red or blue particle moving with velocity $\mathbf{c}_i$.

For completeness, we restate the microdynamical equations given in Section III.A.:

$$r_i(\mathbf{x} + \mathbf{c}_i, t + 1) = r'_i(\mathbf{x}, t), \qquad b_i(\mathbf{x} + \mathbf{c}_i, t + 1) = b'_i(\mathbf{x}, t). \qquad (V.30)$$

These two equations are coupled via a collision operator that depends on the entire state s and also the configurations at neighboring sites. Thus

$$r'_i = C^r_i(s(\mathbf{x}, t), f_s), \qquad b'_i = C^b_i(s(\mathbf{x}, t), f_s), \qquad (V.31)$$

where the collision operator $C^j_i \in \{0, 1\}$ takes as input the 14-bit state $s(\mathbf{x})$ and the discrete color-field angle f_s and gives as output the state of the ith element of species $j \in \{r, b\}$ after collisions have occurred. f_s is obtained from the color distribution at neighboring sites. The "true" color field $\mathbf{f}$ is given by

$$\mathbf{f}(\mathbf{x}) = \sum_{i=1}^{6} \mathbf{c}_i \phi_i, \qquad (V.32)$$

where the relative color density ϕ_i is

$$\phi_i = \sum_{j=0}^{6}[r_j(\mathbf{x}+\mathbf{c}_i) - b_j(\mathbf{x}+\mathbf{c}_i)] \quad (V.33)$$

$$= \mathcal{M}(s(\mathbf{x}+\mathbf{c}_i)). \quad (V.34)$$

Here the color-counting look-up table $\mathcal{M}$ has been implicitly defined. Since $\phi_i \in \{-7,-6,\ldots,6,7\}$, there are 15^6 possible color distributions $(\phi_i)_{i=1,\ldots,6}$, and therefore a similarly large number of possible values of $\mathbf{f}$. For efficient construction of collision tables, however, one may exploit the following observations: 1) many of these distributions yield the same $\mathbf{f}$, due to lattice symmetries; 2) only the direction, not the magnitude, of $\mathbf{f}$ enters in the maximization of equation (III.3), and therefore the outcome of a collision; and 3) small differences in the direction of $\mathbf{f}$ are insignificant for the creation of surface tension. Thus one need only work with a discretized version of the unit vector $\mathbf{f}/|\mathbf{f}|$, which amounts to using a scalar angle code, which is what we call f_*. Typically one allows for 36 values of f_*, uniformly distributed from 0 to 2π, plus an additional state to allow for the case $\mathbf{f}=0$ (Rothman and Keller, 1988); more severe discretizations, however, are possible. The transformation of the color distribution $(\phi_i)_{i=1,\ldots,6}$ to the discrete angle f_* is then symbolically represented by the operator (or look-up table) $\mathcal{T}$ such that

$$\mathcal{T}(\phi_1,\ldots,\phi_6) = f_*. \quad (V.35)$$

VI. Macroscopic limit of phase separating automata

In this section we review the macroscopic behavior of lattice-gas automata for multi-phase flow.

A. Navier-Stokes equation and jump conditions for the ILG

As we noted earlier, the hydrodynamic limit of the pure red or pure blue phase in the ILG is precisely that of the plain FHP lattice gas. The collision rule for a pure phase of the ILG is that of the random FHP model with 7 particles. Other than a specific viscosity resulting from the random collision rule, the hydrodynamics of a bulk phase do not differ from what was found for the FHP models of Section IV., and therefore do not require any new theory.

The velocity of the interfaces in the ILG is equal to the velocity of the fluid from the law of conservation of color. This creates a problem because it is now impossible to recover the real Galilean invariant equation by the change of variables (IV.62). Instead, if one wishes to use the ILG to simulate flows at significant Reynolds numbers, the models must be modified to let $g(\rho_0) = 1$ for some density (Gunstensen and Rothman, 1991a).

The continuity of stress on the interface is a consequence of the conservation of momentum. We here outline the proof of relation (V.5) in 2D. We start by defining a control volume $ABCD$ around a small piece of interface of arc length $\ell \ll R$ where R is the radius of curvature. We let $\alpha = \ell/R$. Pressure forces act on the inside (p_1) and outside (p_2) of the interface. Our control volume is thin around the interface so forces on the sides AB and CD can be neglected, except the capillary forces $\mathbf{f}_c$ (see Figure 16). From the definition of surface tension $\mathbf{f}_c = \sigma\mathbf{n}$, where $\mathbf{n}$ is a unit vector normal to the surface of the control volume (Rowlinson and Widom, 1982). In the absence of velocity these are all the stresses entering the control volume. Thus

$$2\sigma \sin\alpha/2 - (p_1 - p_2)\ell = 0 \quad (VI.36)$$

For small angles α we recover Laplace's law

$$p_1 - p_2 = \sigma/R. \tag{VI.37}$$

The argument follows the same lines in 3D or when viscous stresses are added. It does not however give us any way to obtain the value of the stress σ. Methods for calculating σ will be discussed in the following sections.

The absence of a jump in velocity cannot be demonstrated from first principles. It can however be discussed using symmetry arguments in the following way. Consider a uniform flow, parallel to the horizontal direction x on both sides of a horizontal interface, with velocity u_i in phase i. Suppose that the flow creates a velocity discontinuity with $u_1 > u_2$. Such a discontinuity may be interpreted loosely as meaning that the interface has vanishing viscosity allowing one phase to slip on the other. The symmetry of the red and blue phases indicates that a velocity discontinuity with $u_1 > u_2$ implies the existence of another solution with velocities u_1 and u_2 exchanged. However the solution for a flow parallel to the interface is probably unique, as is the case for pressure and color distribution in our experiments and mesoscopic models. Then we may only have a single solution with $u_1 = u_2$.

We note however that were we to extend ILG models to fluids with asymmetric phases the above arguments cease to be valid and a velocity jump is conceivable. Somers (pers. comm.) has reported difficulties with ILG models with asymmetric viscosity that may be due to such effects

B. Macroscopic limit for the liquid gas model

We now turn to the macroscopic limit for the liquid-gas model. It turns out to be much more difficult to discuss than in the case of the ILG. This difficulty arises because interactions deeply modify the nature of lattice gas automata.

1. Hydrodynamical equations away from interfaces

In order to obtain the macroscopic behavior of the liquid-gas model, we need to make a Boltzmann or factorization assumption, and then continue with a Chapman-Enskog expansion. Such a procedure cannot be valid near interfaces where the gradient of density is large and is only useful to describe the liquid-gas model away from interfaces. It is also a mean-field theory for the phase transition.

a. Boltzmann approximation The Boltzmann equation is obtained from 1) the molecular chaos assumption (IV.17) that indicates that incoming particles are independent and 2) the assumption that particles on interacting sites are factorized. Then the averaging of the liquid-gas microdynamical equation (V.27) is

$$N_i(\mathbf{x} + \mathbf{c}_i, t+1) = N_i(\mathbf{x}, t) + \Delta_i[\mathbf{N}] + \Gamma_i[\mathbf{N}'] - \Gamma_{-i}[\mathbf{N}'] \tag{VI.38}$$

where

$$\Gamma_i[\mathbf{N}'] = \mu(1 - N'_i(\mathbf{x}))N'_{-i}(\mathbf{x})(1 - N'_{-i}(\mathbf{x} + r\mathbf{c}_i))N'_i(\mathbf{x} + r\mathbf{c}_i), \tag{VI.39}$$

and

$$\mathbf{N}' = \mathbf{N} + \Delta[\mathbf{N}]. \tag{VI.40}$$

b. Equation of state and inviscid hydrodynamics A Chapman-Enskog expansion in the manner of Section IV.B.4. may performed:

$$\mathbf{N} = \mathbf{N}^{(0)} + \mathbf{N}^{(1)} + \cdots + \mathbf{N}^{(n)} + \cdots. \tag{VI.41}$$

In Section IV. the leading term of the expansion was an equilibrium solution of the probabilistic dynamics. For the interacting model there is however no equivalent of the existence and uniqueness results of Section IV., nor is there an H-theorem in the manner of M. Hénon's theorem (Hénon, 1987a). However we consider instead of the true probabilistic dynamics the Boltzmann evolution (VI.38). The Boltzmann equation has steady state, spatially homogeneous solutions of the form $\mathbf{N}(\mathbf{x}, t) = \mathbf{N}^{eq}$,

where N^{eq} in given by equation (IV.23). We may also define $N^{(0)}$ as in equations (IV.34) and (IV.37).

We also need to expand the interaction terms. This yields

$$\Gamma_i(\mathbf{x};r) - \Gamma_{-i}(\mathbf{x};r) = rc_{i\alpha}\partial_\alpha\Gamma_i^{(0)} + \mathcal{O}(\nabla^2)$$

where

$$\Gamma_i^{(0)}(\mathbf{x}) = (1 - N_i^{(0)}(\mathbf{x}))N_{-i}^{(0)}(\mathbf{x})(1 - N_{-i}^{(0)}(\mathbf{x}))N_i^{(0)}(\mathbf{x}). \tag{VI.42}$$

The post-collision distributions have the expansion

$$N' = N^{(0)} + \Lambda N^{(1)} + \cdots \tag{VI.43}$$

and the first order equation is obtained by inserting equations (VI.41) and (VI.42) into equation (VI.38) to yield

$$N_i^{(0)}(\mathbf{x} + \mathbf{c}_i, t+1) - N_i^{(0)}(\mathbf{x}, t) = \sum_j \Lambda_{ij}N_j^{(1)}(\mathbf{x}, t) + rc_{i\alpha}\partial_\alpha\Gamma_i(\mathbf{N}^{(0)}). \tag{VI.44}$$

A solvability condition is obtained as usual by multiplying equation (VI.44) by the mass and momentum eigenvectors. The usual mass conservation equation,

$$\partial_t\rho + \partial_\alpha(\rho u_\alpha) = 0, \tag{VI.45}$$

is obtained. The momentum equation is

$$\partial_t(\rho u_\alpha) = -\partial_\alpha\Pi_{\alpha\beta}^{(0)} \tag{VI.46}$$

where the momentum flux tensor is

$$\Pi_{\alpha\beta}^{(0)} = \sum_i \left[N_i^{(0)} - r\Gamma_i(\mathbf{N}^{(0)})\right] c_{i\alpha}c_{i\beta}. \tag{VI.47}$$

This momentum flux tensor may be found directly as for the non-interacting models by a simple count of the interaction crossing an imaginary hyperplane of the model. An important qualitative feature is that the intensity of the interaction term is proportional to r.

From the momentum balance equation (VI.46) and the momentum flux tensor (VI.47) the Euler equation

$$\partial_t\rho u_\alpha + \partial_\beta[g_{\alpha\beta}(\rho)\rho u_\alpha u_\beta] = -\partial_\alpha[p_{\alpha\beta}(\rho, u^2)] \tag{VI.48}$$

is obtained. This equation is parametrised by the interaction strength $z = \mu r$. The non-Galilean factor, sound velocity and pressure may all be expressed as functions of z:

$$g_s(\rho) = \frac{\rho}{\rho_m}\frac{D}{D+2}\frac{1-2d}{1-d}\left(1 + \frac{4zd^2(1-d)^2}{1-2d}\right) \tag{VI.49}$$

$$c_{ss}^2(\rho) = \frac{b_m}{b_m+1}\frac{1}{D}\left[1 - 2zd(1-d)(1-2d)\right] \tag{VI.50}$$

$$p_s(\rho, u^2) = c_{s0}^2\rho - \frac{b_m z}{D}d^2(1-d)^2 + \frac{1}{2}\rho\left(g_s(\rho) - g_0(\rho)c_{ss}^2(D+2)\right)u^2 \tag{VI.51}$$

where the soundspeed is $c_{ss}^2 = \frac{dp_s}{d\rho}$. At $r = 0$ one recovers the results for a non-interacting gas.

We notice that $g_s(\rho)$ contains corrections coming from the interactions. These are due to the fact that the rate of interaction depends on the distributions of particles and holes in the b directions of the lattice. Depending on the velocity and density there may be more or less particles and holes available for interaction in a given direction.

c. Viscous equation The viscous flow in the liquid-gas model has been studied in both the gas and the liquid phase of the maximal model of Section V.C.1.b.. The method of decaying sine waves has been used (Appert and Zaleski, 1993) as well as the observation of Poiseuille flows in 2D channels for the gas phase (Pot et al., 1993) and for the liquid phase (di Pietro et al., 1993).

Results in both the liquid and gas phases are in agreement. Viscosities may be found for the maximal model in tables given by Appert and Zaleski (Appert and Zaleski, 1993). An interesting effect is the growth of the viscosity like the square of the range r. This effect may predicted in a qualitative way by analogy with Maxwell's

estimate $\nu \sim \lambda U$ for the viscosity of gases, where λ is the mean free path and U the thermal velocity. Here we may argue that interactions carry momentum over distances of order r at a speed U which is also of order r, yielding $\nu \simeq r^2$.

Another derivation of viscosity may be made in the framework of the minimal model. Expanding the interacting terms at order 2 is straightforward if one notices the following identity for the Chapman-Enskog expansion of the interaction terms:

$$\Gamma_i(\mathbf{x}; r) - \Gamma_{-i}(\mathbf{x}, r) = r\frac{\partial \Gamma_i}{\partial r} + \frac{r^2}{2}\frac{\partial \Gamma_i}{\partial r^2} + \cdots + \frac{r^n}{n!}\frac{\partial^n \Gamma_i}{\partial r^n} + \cdots \qquad \text{(VI.52)}$$

Here each term in the expansion is of the corresponding order in gradient such that $(r^n/n!)(\partial^n \Gamma_i/\partial r^n) = \mathcal{O}(\nabla^n)$.

Writing the solvability condition at order 2 as in Section IV, we obtain the Navier Stokes equations

$$\partial_t \rho u_\alpha + \partial_\beta [g_{\mu r} \rho u_\alpha u_\beta] = -\partial_\alpha p_{\mu r} + \partial_\beta \left(\nu \partial_\beta (\rho u_\alpha)\right) + \partial_\alpha \left[\left(\frac{D-2}{D}\nu + \zeta\right)\partial_\beta (\rho u_\beta)\right] \qquad \text{(VI.53)}$$

where

$$\nu = \nu_0 + \frac{2\mu r}{D+2} d(1-d)(1-2d) + \mu r^2 d(1-d)\frac{b_m}{D(D+2)} \qquad \text{(VI.54)}$$

$$\zeta = \zeta_0 + \frac{1}{2}(c^2_{s\,\mu r} - c^2_{s0}) + \frac{2b_m \mu r}{b_m + 1} d(1-d)(1-2d) + \mu r^2 d(1-d)\frac{b_m}{D} \qquad \text{(VI.55)}$$

$$\nu_0 = -\frac{b_m}{D(D+2)}\psi - \frac{1}{2(D+2)} \qquad \text{(VI.56)}$$

$$\zeta_0 = \frac{b_m}{D} X - \frac{1}{2D} + \frac{1}{2} c^2_{s0}. \qquad \text{(VI.57)}$$

The dependence of ν with r is the most important qualitative feature of this expansion.

We now turn to another effect of the interactions on the viscous behaviour of the model. Measurements of the viscosity made using a Poiseuille viscometer were performed by di Pietro et al. (di Pietro et al., 1993). The Poiseuille viscometer is set up just as the analogous device of Kadanoff et al. (Kadanoff et al., 1989). The measured viscosity is plotted in Figure 17 for various flow speeds and channel widths. A variation of viscosity with velocity squared is observed. A similar effect is observed in non-interacting lattice gases (Diemer et al., 1990) but it is much weaker there.

Both the r^2 and the strong u^2 dependence of the measured viscosity are drawbacks of our model. Together with the non-Galilean $g(\rho)$ factor they limit the possibility of leaving the region of vanishingly small Reynolds numbers and they limit velocities to small values which slows down the simulations. Further exploration of modifications to interacting models is necessary to overcome these difficulties.

2. Jump conditions

Mass and momentum conservation imply as in the case of the ILG that the stress jump condition (V.5) is verified. In particular surface tension exists and leads to Laplace's law. This has been verified in numerical experiments that are reviewed in Section VII.A.. In what follows below we report on velocity jumps and equilibrium pressures.

a. Velocity jump In presence of a possible phase change conservation of mass now takes into account the rate at which molecules evaporate or condense on the interface. Instead of the continuity of normal velocity implied by equation (V.3), we have the Rankine-Hugoniot condition (Whitham, 1974)

$$[\rho \mathbf{u} \cdot \mathbf{n}] = [\rho] V_I, \qquad \text{(VI.58)}$$

where V_I is the velocity of the interface. In the liquid-gas model this equation holds as a consequence of the conservation of mass.

The continuity of tangential velocity is on the other hand in strong doubt. Consider again as in Section VI.A. the uniform flow parallel to an interface. The symmetry arguments invoked earlier cannot be used here. We instead try to discuss in a heuristic way the possible differences beteween the real-world jump conditions and those likely to prevail in the liquid-gas model.

In steady parallel flow the momentum flux $\Pi_{xy} = 0$. In the liquid-gas model we have not calculated the stress Π_{xy} on the interface. However when interactions have a small effect on the distribution, as in the Boltzmann case (Appert, 1993), the non-

interacting case still holds and $\Pi_{xy} = \nu\frac{\partial(\rho u)}{\partial y}$. Thus we obtain $\frac{\partial(\rho u)}{\partial y} = 0$. Integrating accross the interface we obtain the jump condition

$$[\rho \mathbf{u} \cdot \mathbf{t}] = 0 \tag{VI.59}$$

for all tangent vectors t.

b. Equilibrium pressures and Gibbs-Thomson relations In a real liquid-gas system in equilibrium, both phases are constrained to have equal chemical potentials as required by equation (V.24). This results in a macroscopic condition known as the Gibbs-Thomson relation for curved interfaces (Rocard, 1967). Let fluid 1 be on the concave side of the interface and fluid 2 on the convex side. Then

$$p_1 = p^{eq} + \sigma\kappa\frac{\rho_2}{\rho_1 - \rho_2} \tag{VI.60}$$

$$p_2 = p^{eq} + \sigma\kappa\frac{\rho_1}{\rho_1 - \rho_2} \tag{VI.61}$$

Note that by subtracting those two equations one obtains Laplace's law (VI.37).

These relatively little known conditions have a major importance in determining the rate of nucleation of phase 1 in phase 2. We have not been able so far to determine their validity from first principles for the liquid-gas model. However numerical experiments on curved surfaces in equilibrium have been performed in 2D (Appert and Zaleski, 1993; Pot et al., 1993; Appert et al., 1993c). The results in the 3D case are shown in Figure 18. They result in a slightly different correlation

$$p_1 = p^{eq} + \alpha\sigma\kappa\frac{\rho_2}{\rho_1 - \rho_2} \tag{VI.62}$$

$$p_2 = p^{eq} + \sigma\kappa\left[1 + \alpha\frac{\rho_2}{\rho_1 - \rho_2}\right]. \tag{VI.63}$$

Subtracting these two equations still yields Laplace's law.

We believe that this disagreement with the classical thermodynamical relation is an effect of the "non-potential" character of our model in the sense of Section V.B..

VII. Interfaces in phase-separating automata

Having given the macroscopic description of phase-separating automata in the previous two sections in terms of hydrodynamics and jump conditions, we now discuss in detail the jump conditions themselves. Specifically, in this section we derive expressions for surface tension for both immiscible lattice-gas and liquid-gas models, we present empirical measurements of surface tension, and, where applicable, we compare theory with simulation. In closing this section we look briefly at interface fluctuations, and find, somewhat surprisingly, that interface fluctuations in a non-potential lattice-gas model are reasonably well described by classical theory.

A. Surface tension in immiscible lattice gases

1. Boltzmann approximation

To obtain an estimate of surface tension in the ILG, we first need to express equations (V.30) and (V.31) in terms of the evolution of a probability field (Adler et al., 1994). In a manner analogous to that used in Section IV. for simple lattice gases, we define the average quantities

$$R_i = \langle r_i \rangle, \qquad B_i = \langle b_i \rangle \tag{VII.1}$$

and also

$$N_i = \langle n_i \rangle = R_i + B_i, \tag{VII.2}$$

which are, respectively, the probability of observing $r_i = 1$, $b_i = 1$, and $n_i = 1$. We then neglect correlations, as in the Boltzmann approximation of Section IV.. While necessary to simplify theoretical calculations, the neglect of correlations is a potentially serious deficiency because the presence of interfaces may significantly increase correlations. Nevertheless such an approximation allows us to make progress, and serves as a useful reference for better approximations that may follow. Thus,

specifically, for the evolution of the red particles we write

$$R_i(\mathbf{x}+\mathbf{c}_i, t+1) = \sum_{s,s',f_s} r_i' A(s,s',f_s) P(s;\mathbf{x},t) Q(f_s;\mathbf{x},t), \qquad \text{(VII.3)}$$

and for evolution of the blue particles we have

$$B_i(\mathbf{x}+\mathbf{c}_i, t+1) = \sum_{s,s',f_s} b_i' A(s,s',f_s) P(s;\mathbf{x},t) Q(f_s;\mathbf{x},t). \qquad \text{(VII.4)}$$

Here the sums are taken over all possible states s that may enter a collision, all possible states s' that may result from a collision, and all possible discrete field angles f_s. The factor $A(s,s',f_s)$ represents the probability of obtaining state s' when state s enters a collision at a site with a neighborhood configuration indexed by f_s. The probability that state s actually enters the collision at time t at the site located at position $\mathbf{x}$ is given by

$$P(s;\mathbf{x},t) = \prod_{i=0}^{6} R_i^{r_i} B_i^{b_i} (1-N_i)^{1-r_i-b_i}. \qquad \text{(VII.5)}$$

The probability that the discrete field angle is f_s is

$$Q(f_s,\mathbf{x}) = \sum_{(\phi_i):\mathcal{T}(\phi_1,\ldots,\phi_6)=f_s} \left(\prod_{i=1}^{6} W(\phi_i;\mathbf{x}) \right), \qquad \text{(VII.6)}$$

where the relative color density ϕ_i was defined in equation (V.33). Here the sum is taken over all possible combinations of $(\phi_i)_{i=1,\ldots,6}$ that correspond to f_s, and the product is taken over the probabilities $W(\phi_i)$ of observing the relative color density ϕ_i at the ith neighbor. Specifically, $W(\phi_i)$ is given by the sum of the probabilities of all states that yield the color density ϕ_i:

$$W(\phi_i;\mathbf{x}) = \sum_{s:\mathcal{M}(s)=\phi_i} P(s;\mathbf{x}+\mathbf{c}_i). \qquad \text{(VII.7)}$$

2. Surface tension

To calculate the surface tension, we note that in the vicinity of an interface the pressure is locally anisotropic, since the pressure in the direction parallel to the interface is reduced by the tension on the interface itself. For the case of a flat interface perpendicular to the x-axis, the surface tension σ is given by the integral over x of the

difference between the component P_N of pressure normal to the interface and the component P_T transverse to the interface (Rowlinson and Widom, 1982):

$$\sigma = \int_{-\infty}^{\infty} [P_N(x) - P_T(x)]\,dx. \qquad \text{(VII.8)}$$

In mechanical equilibrium one has $P_N(x) = P$, the (isotropic) pressure far from the interface. Equation (VII.8) gives the surface tension as a function of the pressure. As defined in Section IV., the pressure tensor, or momentum-flux density tensor, is

$$\Pi_{\alpha\beta} = \sum_{i=0}^{6} c_{i\alpha} c_{i\beta} N_i; \qquad \text{(VII.9)}$$

P_N and P_T are therefore equivalent to Π_{xx} and Π_{zz}, respectively, where the x-axis is taken parallel to the interface. Prediction of the surface tension is thus a problem of predicting the distribution of the populations N_i near an interface.

Below we review a recent theoretical calculation of surface tension and then summarize a comparison of these theoretical results with measurements obtained from simulations (Adler et al., 1994).

a. Theoretical calculation Because the evaluation of equation (VII.8) may depend on the orientation of the interface, it has been studied both for the case in which the interface is parallel to a lattice direction (say, $\mathbf{c}_6$), and for the case in which the perpendicular to the interface is parallel to a lattice direction. We refer to the former case as the "0-degree interface," while calling the latter the "30-degree interface." An example of each is shown in Figure 19. Here we summarize the calculation for the 0-degree interface only; details of the calculation for the 30-degree interface are given by Adler et al. (Adler et al., 1994).

As shown in Figure 19a, the center of the 0-degree interface is taken to be between and parallel to two (horizontal) lattice lines. The upper line is labeled y_1 and the lower line is labeled y_{-1}. We assume an average of $7d$ particles per site far from the interface; in equilibrium, therefore, we must have particles arriving at interface sites

with probability d, independent of time. This fixes the boundary conditions

$$N_i(y_1, t) = d, \qquad i = 4, 5 \ \forall t \tag{VII.10}$$

at all sites in layer y_1 and

$$N_i(y_{-1}, t) = d, \qquad i = 1, 2 \ \forall t \tag{VII.11}$$

at all sites in layer y_{-1}. Here the direction index i has the same sense at that defined in equation (II.2). These boundary conditions require that the populations N_i be symmetric across the center of interface after rotation through 180 degrees. Thus for the moving particles

$$N_i(y_1, t) = N_{i+3}(y_{-1}, t), \qquad i = 1, \ldots, 6, \tag{VII.12}$$

where, as before, the circular shift $i + 3 = j$ such that $c_j = -c_i$, $j = 1, \ldots, 6$, while for the rest particles

$$N_0(y_1, t) = N_0(y_{-1}, t). \tag{VII.13}$$

Thus in this two-layer case, the dynamics of the interface can be completely determined by solving only for the populations in layer y_1. Within this layer, requirements of symmetry and mechanical stability further reduce the remaining five populations to only two independent populations. Specifically, mechanical stability requires that the pressure be divergence-free, and therefore that $P_N = P = 3d$. This gives, by virtue of the boundary condition (VII.10),

$$N_1 = N_2 = N_4 = N_5 = d. \tag{VII.14}$$

In addition, since there is no current parallel to the interface (or, equivalently, by symmetry with respect to the perpendicular to the interface), we have

$$N_3 = N_6. \tag{VII.15}$$

Thus the two free population variables are the rest-particle population, N_0, and one of the laterally moving populations, say N_3. These populations evolve according to

$$N_i(y_1, t + 1) = N_i'(y_1, t), \qquad i = 0, 3, 6, \tag{VII.16}$$

where the post-collision state is denoted by

$$N_i'(\mathbf{x}, t) = \sum_{s, s', f_\sigma} n_i' A(s, s', f_\sigma) P(s; \mathbf{x}, t) Q(f_\sigma; \mathbf{x}, t), \tag{VII.17}$$

in which we have also used $n_i' = r_i' + b_i'$.

The evolution of color, or concentration $\theta_i = R_i/N_i$, must also be specified. In addition to the symmetry given by equations (VII.12) and (VII.13), we also have

$$\theta_i(y_1, t) = 1 - \theta_{i+3}(y_{-1}, t), \qquad i = 1, \ldots, 6, \tag{VII.18}$$

and

$$\theta_0(y_1, t) = 1 - \theta_0(y_{-1}, t). \tag{VII.19}$$

Additional symmetries and stationarity of the interface allow the seven concentration variables in layer y_1 to be reduced to three independent variables. First, we note that symmetry with respect to the perpendicular to the interface gives

$$\theta_3 = \theta_6, \qquad \theta_1 = \theta_2, \qquad \theta_4 = \theta_5. \tag{VII.20}$$

Together with the concentration θ_0 for the rest-particle population, the first of these three pairs evolve according to

$$\theta_i(y_1, t + 1) = \theta_i'(y_1, t), \qquad i = 0, 3, 6 \tag{VII.21}$$

where we have used $\theta_i' = R_i'/N_i'$. The evolution of the second pair of concentrations is determined by particles that cross the interface; using equation (VII.18), we obtain

$$\theta_i(y_1, t + 1) = 1 - \theta_{i+3}'(y_1, t), \qquad i = 1, 2. \tag{VII.22}$$

Since the stationarity of the interface requires that no net concentration crosses it, in steady state we must have

$$\theta_4'(y_1) = \theta_5'(y_1) = \frac{1}{2}, \tag{VII.23}$$

and therefore, by equation (VII.22),

$$\theta_1(y_1) = \theta_2(y_1) = \frac{1}{2}. \tag{VII.24}$$

It remains only to specify the red concentration coming in from afar. Since in equilibrium the concentration that leaves the interface must be equal to the concentration that enters it, we set

$$\theta_i(y_1, t-1) = \theta'_{i+3}(y_1, t), \qquad i = 4, 5. \tag{VII.25}$$

Thus two of the three free concentration variables may be taken to be θ_0 and θ_3, which enter via equation (VII.21), while the third may be taken to be θ_4, which enters equation (VII.25) above.

To complete the specification of the problem we need an expression for $Q(f_s)$, the probability of the discrete field angle f_s. From equation (VII.6), one sees that all that is required is required is knowledge of $W(\phi_i)$, for $i = 1, \ldots, 6$. These quantities may each be obtained from the symmetries and boundary conditions of the problem. Noting that $W(\phi_0)$ is the probability distribution for relative color density for the interface site in layer y_1, one finds

$$W(\phi_3) = W(\phi_6) = W(\phi_0) \tag{VII.26}$$

for the neighboring sites in layer y_1, and

$$W(\phi_4) = W(\phi_5) = W(-\phi_0) \tag{VII.27}$$

for the neighboring sites across the interface in layer y_{-1}. For the sites on the boundary (i.e., layer y_2), one has, assuming that the chosen site in layer y_1 is at position $\mathbf{x}_1$,

$$N_i(\mathbf{x}_1 + \mathbf{c}_j, t) = d, \qquad i = 0, \ldots, 6, \qquad j = 1, 2 \tag{VII.28}$$

for the populations, and

$$\theta_i(\mathbf{x}_1 + \mathbf{c}_j, t) = \theta_{j+3}(\mathbf{x}, t), \qquad i = 0, \ldots, 6, \qquad j = 1, 2 \tag{VII.29}$$

for the concentrations. $W(\phi_1)$ and $W(\phi_2)$ may then be calculated directly from equations (VII.5) and (VII.7).

The dynamics of the interface are thus fully specified by equation (VII.16) for the two free populations N_0 and N_3, equations (VII.21) and (VII.25) for the three free concentrations θ_0, θ_3, and θ_4, and equations (VII.26), (VII.27), (VII.28), and (VII.29) for the determination of the color field angle. Adler et al. (Adler et al., 1994) solved this system by numerically determining the steady-state post-collision populations N_i^*. The surface tension is then obtained from equations (VII.8) and (VII.9), which yields

$$\sigma = \sqrt{3} \sum_{i=0}^{6} (c_{i\perp}^2 - c_{i\parallel}^2) N_i^*, \tag{VII.30}$$

where $c_{i\perp}$ and $c_{i\parallel}$ are the components of $\mathbf{c}_i$ perpendicular and parallel to the interface, respectively.

b. Comparison with simulation Figure 20 compares results from the Boltzmann approximation for both the 0-degree and 30-degree interfaces with results from three different empirical measurements from simulations (Adler et al., 1994). We comment first on the theoretical predictions, and then on each of the empirical measurements.

Perhaps the most interesting feature of the theoretical calculation is the phase transition at $d = d_c \approx 0.25$. Below d_c surface tension vanishes, while above d_c the surface tension rises to a peak at about $d = 0.6$ and then falls to zero at $d = 1.0$. (Surface tension vanishes at $d = 1.0$ because each N_i must equal one.) One sees also that the 30-degree interface has a surface tension which is usually greater than that of the 0-degree interface, with a maximum deviation of about 20%.

The first of the three empirical measurements consists of the simulation of a red bubble of radius R in a blue box with periodic boundary conditions, of size greater than or equal to $4R$. The pressure P_{in} inside the bubble is compared to the pressure P_{out} outside the bubble. One expects adherence to Laplace's formula:

$$P_{in} - P_{out} = \frac{\sigma}{R}. \tag{VII.31}$$

Figure 21 shows this pressure difference as a function of $1/R$ for the case $d = 0.7$.

The best-fitting straight line passing through the origin is also shown. The fit to the straight line is good; thus the slope of this line gives the empirical estimate of σ. Similar measurements, the results of which are shown in Figure 20, were made at other values of d, ranging from $d = 0.5$ to $d = 0.9$.

While the bubble tests should, in theory, provide a measure of the average surface tension, integrated over all angles, one may also make measurements of the surface tension on interfaces that are, on average, flat, by numerical integration of equation (VII.8). Figure 20 shows two such measurements, one set for a zero-degree interface, and the other for a 30-degree interface. These "integral tests" display approximately the same magnitude of anisotropy that was determined from the Boltzmann approximation, with the 30-degree interface usually yielding the greater surface tension, as predicted. Moreover, within the margin of error of the measurements, the integral tests approximately bracket the results of the bubble tests, as one expects.

Although the theoretical predictions and empirical measurements are always in qualitative agreement, quantitative agreement is lacking. The poor quantitative accord could be due to several reasons. First, the Boltzmann estimate was obtained by neglecting correlations. However, correlations are likely to be strong near an interface, and thus contribute significantly to the surface tension. Second, because the integral tests were made on fluctuating, rather than purely flat, interfaces (see Section VII.C.), the results of these tests are necessarily approximate. Third, the Boltzmann approximation reviewed here considered only the thinnest interfaces possible. Calculations with thicker interfaces for $d \geq 0.7$ show that differences are negligible, but significant increases to the surface tension are possible with thicker interfaces, particularly as d approaches d_c (Adler et al., 1994). Moreover, when one layer of sites is added on each side of the interface, d_c decreases from 0.25 to 0.22.

B. Interfaces in liquid-gas models

The analysis of surface tension in liquid-gas models also uses the Boltzmann approximation. It thus bears some similarity with the analysis reported above. This analysis has only been carried out for the FCHC lattice gas with liquid-gas interactions. It is at present quite sketchy, as only a single value of the interaction range r and of the interface angle with the lattice has been investigated. However, we expect on theoretical grounds that there is a limit where r becomes large and the interfaces become wide where the Boltzmann approximation yields a precise estimate for surface tension and density profiles. Thus, because interfaces in the liquid-gas model are relatively wide compared to those in the ILG, this calculation brings something new compared to the previous one. Specifically, it predicts the density profile inside the interface with good accuracy.

In what follows we briefly review the existing work. We follow closely Appert et al. (Appert et al., 1993c).

To simplify the calculations we consider the FCHC lattice projected in 3D. All populations N_i depend only on x. The normal pressure is defined by $P_N = \Pi_{xx}$ while the tangential pressure is related to the other diagonal components, i.e., $P_T = \Pi_{yy} = \Pi_{zz}$. We will find the following notation useful. We let $\Gamma(\mathbf{x}_1, \mathbf{x}_2)$ be the amount of momentum exchanged by an interaction between sites $\mathbf{x}_1$ and $\mathbf{x}_2$. From equation (VI.39) this is

$$\Gamma(\mathbf{x}_1, \mathbf{x}_2) = \mu[1 - N'_i(\mathbf{x}_1)]N'_{-i}(\mathbf{x}_1)[1 - N'_{-i}(\mathbf{x}_2)]N'_i(\mathbf{x}_2). \qquad \text{(VII.32)}$$

In the above definition i is defined implicitly as the index of the velocity direction $\mathbf{c}_i$ parallel to $\mathbf{x}_2 - \mathbf{x}_1$ and μ is the rate of interaction. The populations N'_i are the after-collision populations as in Section VI.. We consider an imaginary surface Σ located at $x = x_0$ between two layers of sites (Figure 22). Points on these layers have abscissa $(x_0 - 1/2)$ or $(x_0 + 1/2)$. Then

$$\Pi_{\alpha\beta} = \sum_i c_{i\alpha} c_{i\beta} \left\{ N_i(\mathbf{x} + \mathbf{c}_i/2) - \sum_{k=0}^{r-1} \Gamma[\mathbf{x} - (k + \frac{1}{2})\mathbf{c}_i, \mathbf{x} + (r - k - \frac{1}{2})\mathbf{c}_i] \right\} \qquad \text{(VII.33)}$$

where $\mathbf{x} = (x_0, y, z)$ is an arbitrary point on Σ. This expression is obtained by noticing that as for the usual lattice gas, particle propagation contributes $c_{i\alpha}c_{i\beta}$ to the momentum transfer, while an interaction contributes $-2c_{i\alpha}c_{i\beta}$. The factor of 2 disappears as interactions are counted twice in the sum.

From this expression a necessary condition for equilibrium can be written

$$P_N(x) = P_N(x+1). \qquad \text{(VII.34)}$$

This equation is the equivalent of equation (V.21) for our model. To solve it we make the additional assumption that the populations are close to Fermi-Dirac equilibrium. This assumption is perhaps best verified in the limit $r \to \infty$, $\mu \to 0$ and $z = r\mu$ constant. Indeed as we approach this limit the equation of state remains unchanged while the interaction range increases.

Expression (VII.34) can be developed after some simplifications coming from the FCHC lattice are noticed. The principal simplification is that all particles crossing a surface Σ at x (we drop the subscript in x_0 from now on) originate either from the line at $x - 1/2$ or the line at $x + 1/2$. Then

$$\begin{aligned} P_N(x) &= 6[d(x-\frac{1}{2}) + d(x+\frac{1}{2})] \\ &- 12\mu \sum_{k=0}^{r-1} d(x-\frac{1}{2}-k)[1-d(x-\frac{1}{2}-k)]d(x+r-\frac{1}{2}-k)[1-d(x+r-\frac{1}{2}-k)] \end{aligned} \qquad \text{(VII.35)}$$

A solution to equations (VII.34) and (VII.35) has been found numerically by a relaxation method (Appert et al., 1993c). Solutions are found for large boxes (128 layers wide) and moderately wide interfaces ($r = 8$ and $\mu = 1$). The result is shown in Figure 23.

A unique solution is found by the relaxation procedure. This is not a numerical proof of the existence of a unique stable solution of equation (VI.38) but comes close to it since our relaxation procedure resembles the actual timestepping of the Boltsmann equation (see Appert et al. (Appert et al., 1993c) for details). One result

TABLE 2

	d_{gas}[a]	d_{liq}[b]	p_{eq}[c]
prediction	0.033	0.523	0.148
measurements	0.031	0.525	0.143 ± 0.003

[a]Equilibrium gas density for the 3D FCHC liquid-gas model (r=8).

[b]Equilibrium liquid density

[c]Equilibrium pressure

of the calculation is the equilibrium pressure p_{eq} and the equilibrium liquid and gas densities given in Table 2. There is a qualitatively good agreement for the density profile and the equilibirium quantities but the result is still outside the error bars of the measurements. The possible reason for that discrepancy is discussed below.

The resulting density profile allows one to compute, using the same Fermi-Dirac approximation and equation (VII.33), the other independent component P_T . From that component a value of surface tension may be calculated.

Comparison with numerical simulations is in progress. Surface tension has been estimated using Laplace's law from measurements of equilibrium pressures across curved interfaces. This measured surface tension yields $\sigma = 1.19$ for $r = 8$. The theoretical surface tension is $\sigma = 1.82$. Agreement here is much worse than for the equilibrium densities and pressure. However the model may have a strong anisotropy, as was observed numerically for the maximal model of Appert and Zaleski (Appert and Zaleski, 1993). To be more specific, our theory gives the surface tension for a 0-degree angle only while the theoretical calculation for a 45-degree angle is missing. It is likely that there is a large difference between the surface tensions for various angles. The estimate from Laplace's law is expected to interpolate between these various values. This would be one explanation of the large error we have at this stage. Another possible source of error is the assumption of factorisation or lack of

correlation between sites. It has already been observed in other liquid-gas models that correlations tend to appear as the interaction distance r becomes large but μ stays fixed to 1 (Appert and Zaleski, 1993). It is possible that the FCHC model with $r = 8$ has similar correlations.

At this point it is interesting to notice that the origin of surface tension in the liquid-gas model is different than that in the ILG. In the ILG the pressure tensor comes only from propagation. It is anisotropic because populations are themselves anisotropic inside the interface. On the other hand in the liquid-gas model we find surface tension with isotropic populations estimated from the Fermi-Dirac equilibrium. It is the nonlocal interaction terms that contribute to the pressure tensor and bring the necessary anisotropy.

C. Interface fluctuations

As emphasized in Section IV., the Boolean nature of lattice gases creates statistical fluctuations that, in reversible models, may be understood as the fluctuations of Gibbs states (Zanetti, 1989). Such a classical description is not possible, however, in our irreversible phase-separating automata. Thus it is of interest to ask how the fluctuations of interfaces in these models compares to the fluctuations predicted by classical theory. Below, after first reviewing the classical viewpoint, we summarize a recent empirical measurement of interface fluctuations in the ILG (Adler et al., 1994). A related study of lattice-gas interfaces (in which the interfaces are contructed by the explicit definition of a flexible boundary) has been performed by Burgess et al. (Burgess et al., 1989).

Classical interface fluctuations may be understood in terms of fluctuations of surface energy (Ma, 1985). For a one-dimensional interface in a two-dimensional space, the energy, H, of the interface is proportional to its length L. If the interface has length L_0 when it is flat, and its fluctuations are sufficiently small such that they may be decomposed into Fourier modes of amplitude $|A_q|$ much less than the wavelength $2\pi/q$, then the interfacial energy is, to leading order,

$$H = \sigma L \approx \sigma L_0 + \frac{\sigma}{2} L_0 \sum_q q^2 |A_q|^2. \tag{VII.36}$$

By the equipartition theorem, one has

$$\frac{1}{2}\sigma L_0 q^2 |A_q|^2 = \frac{1}{2} kT, \tag{VII.37}$$

or

$$|A_q|^2 = \frac{kT}{L_0 \sigma q^2}. \tag{VII.38}$$

Figure 24 compares this prediction with measurements made from simulations of ILG interface fluctuations. The ILG was initialised with a flat interface of length $L_0 = N\sqrt{3}/2$ dividing the red fluid from the blue fluid in a box of height $N = 256$, with particle density $d = 0.7$. The boundary conditions were periodic in the direction

parallel to the interface, while walls were placed above and below the interface. After allowing the system 1000 time steps to relax to equilibrium, the power spectrum

$$|A_q|^2(t) = \left| \frac{2}{N} \sum_{n=0}^{N-1} h_n(t) \exp(-iqn/N) \right|^2 \qquad \text{(VII.39)}$$

was computed from measurements $h_n(t)$ of the interface heights at each time step t, and then averaged over 10^5 time steps. Figure 24 shows $\log(|A_q|^2)$ as a function of $\log q$, compared to the theoretical curve obtained from equation (VII.38). To compute the theoretical curve, we have used $\sigma = 0.403$, the prediction obtained from the Boltzmann approximation described in Section VII.A.. For an estimate of kT, we have chosen the equal-time momentum-momentum correlation function

$$\sum_i \sum_j \langle [c_{i\alpha}(n_i - N_i)][c_{j\beta}(n_j - N_j)] \rangle = 3d(1-d)\delta_{\alpha\beta}, \qquad \text{(VII.40)}$$

or, equivalently, the variance of momentum fluctuations at a site (Kadanoff et al., 1989). Comparing the two curves, one finds that the slope of the empirical curve is indeed approximately -2 for wavenumbers below a high-wavenumber cutoff, and that the prefactor (and thus our estimate of kT from the equipartition theorem) is approximately correct (within about 25%). We conclude, then, that ILG interface fluctuations are qualitatively in accord with the statistical mechanics of classical interfaces.

How could such an agreement be possible? We believe that the fact that the fluctuations scale like q^{-2} probably only indicates that ILG interfaces are "rough," in the sense that their slopes are random and uncorrelated. In other words, $h(x)$ is just a random walk in one dimension, and $|A_q|^2 \propto q^{-2}$ results from the usual considerations of diffusive processes. However, the fact that the equipartition theorem works to obtain a reasonable estimate of kT is relatively remarkable. The Gibbs probabilities that this result implies may arise from an effective time-reversible behavior that exists in a kind of subspace of the larger region of phase space that satisfies the conservation of mass, momentum, and color. Such a behavior could be due to the fact that the

noise arises mostly in the bulk phases, which are time-reversible, while the irreversible noise generated at the interface is bounded by the finite thickness of the interface, and is thus possibly negligibly small.

VIII. Phase transitions in phase-separating automata

In this section we address specific aspects of phase transitions in phase-separating automata, and where possible we illustrate comparisons between theoretical predictions and empirical results from computer simulations of the models. For the case of the liquid-gas model, we find an excellent agreement between direct measurements of the pressure-density relation and the theoretical prediction of the equation of state. This equation of state resembles a Van der Waals equation and allows prediction of a phase transition. In the case of the immiscible lattice gas, we can find, albeit qualitatively, the two-phase region of its phase diagram by determining under which conditions the diffusivity of the minority phase becomes negative. In closing this section, we address dynamical aspects of phase transitions in lattice gases by empirical investigations of scaling properties during phase separation.

A. Liquid-gas transition in the liquid-gas model

The equation of state was obtained for the liquid-gas model in Section VI.B.1.b.. For a lattice gas at rest it reads

$$p(d) = \frac{b_m c^2}{D}\left[d - z d^2 (1-d)^2\right] \qquad \text{(VIII.1)}$$

where $d = \rho/b$ is the reduced density and $z = r\mu$ is a control parameter that plays the rôle of temperature in a classical phase-transition model. This equation of state presents a critical point at $z_c \simeq 5.2$. The location of this critical point is independent of dimension and number of particles. It is interesting to point out the analogy beween this equation and a Van der Waals equation of state. For vanishing d we have

$$p(V) \simeq \frac{b_m c^2}{D}\left(\frac{1}{V} - z\frac{1}{V^2}\right). \qquad \text{(VIII.2)}$$

Below the critical point, for $z < z_c$, there is a range of values of d for which $\frac{\partial p}{\partial d} < 0$ and the homogenous phase of density d is unstable. This range of values of d is called the

spinodal region for our model. As in a real liquid-gas system the model then splits into two phases, one of high density and another of low density. The separation of the two phases occurs through the spinodal decomposition process described in Section III.B..

The validity of equation (VIII.1) is verified by direct numerical simulations (Appert et al., 1993c). In these simulations the system is initialized with particles placed at random on the lattice. Two series of measurement are made and the results are plotted in Figure 25. In the first series, measurements are made immediately after initialisation and show agreement with equation (VIII.1) for all densities. The second series of measurements is made after the system has gone through spinodal decomposition and equilibrated. These measurements show a *Maxwell plateau* for the pressure in the spinodal region. Outside the spinodal region the separated equilibrium state may coexist with a homogeneous metastable stable. As seen in Section VII.B., these states coexist at a unique equilibrium pressure and corresponding equilibrium liquid and gas densities.

B. Spinodal decomposition in immiscible lattice gases

Classical phase separation occurs when the free energy of mixture, $F = U - TS$ (U is internal energy, S is entropy), has a minimum for two separated phases. Typical free energy curves are shown in Figure 26. Above T_c, the free energy has a single minimum, corresponding to a perfectly mixed state. In the simplest case of a symmetric binary fluid, this mixed state corresponds to a thermodynamic phase in which a single fluid consists of 50% of the "red" species and 50% of the "blue." Below T_c, however, the free energy curve develops a double well; the stable state now corresponds to a new thermodynamic phase in which a "red-rich" fluid coexists with a "blue-rich" fluid. The two fluids are separated from each other by interfaces, and the relative purity of each fluid (i.e., the redness of the red phase) increases with decreasing temperature.

Although ILG dynamics do not derive from a thermodynamic potential, the model exhibits to a surprising extent much the same behavior of classical binary fluids. For example, we have already seen in Figure 6 how the ILG may exhibit spontaneous phase separation from an initial mixed state. Below we show, both theoretically and empirically, that the existence of the phase separation instability depends on both the population density d and the relative concentration of the two fluids. This analysis results in a phase diagram in the plane of density and concentration, in which the phase boundary demarcates the two-phase, or phase-separated state, from the one-phase, or mixed state. We argue that this phase boundary is the athermal ILG's analog of the classical thermodynamic spinodal curve. In the classical view, summarized in Section V.B.1., the spinodal curve is obtained from the locus of points in the plane of temperature and concentration for which the free energy density has a point of inflection. As shown in equation (V.14), this corresponds to a change in sign of the diffusivity of concentration. Thus our prediction of the ILG phase diagram amounts to a calculation of the ILG diffusivity as a function of concentration and density.

Rather than representing the current of concentration in the ILG in terms of the

variation of a potential F as in equation (V.9), we instead assume a Fickian, or linear, relation between concentration current and concentration gradient:

$$\mathbf{J} = -D(d,\theta)d\nabla\theta. \tag{VIII.3}$$

Here $\mathbf{J} = \langle \mathbf{q} \rangle$, a coarse-grained average of the color flux defined by equation (III.1), and D, the diffusion coefficient, depends on both the particle density and concentration. In lattice-gas models satisfying microscopic time-reversibility (or, more generally, semi-detailed balance), an H-theorem exists to show that transport coefficients are necessarily positive (Hénon, 1987a). The ILG collision rules, however, are time-irreversible and do not satisfy semi-detailed balance; thus D may be either positive or negative. That D can be negative is readily apparent from the rules expressed by equations (III.1), (III.2), and (III.3): as long as there are two colors present at a site, the collision rule *always* chooses to maximize the alignment of the flux q with the color gradient, or field, f. The question that remains is whether J and $\nabla\theta$, the coarse-grained averages of q and f, are themselves aligned. Thus we seek an estimate of D, or, more specifically, its sign, as a function of d and θ.

1. Chapman-Enskog estimate of the diffusion coefficient

To estimate the diffusion coefficient (Rothman and Zaleski, 1989), we first rewrite equation (VII.3) in a way that explicitly notes changes in both space and time, and moreover allows for explicit consideration of populations at neighboring sites:

$$R_i(\mathbf{x}+\mathbf{c}_i, t+1) - R_i(\mathbf{x},t) = \sum_{s,s',S} (r_i' - r_i) A(s,s',S) P(s) H(S). \tag{VIII.4}$$

Here $H(S)$ is the probability of neighboring configurations $S = (s^j)_{j=1,\ldots,6}$ given explicitly by

$$H(S) = \prod_{j=1}^{6} \prod_{i=0}^{6} R_i^{r_i^j}(\mathbf{x}+\mathbf{c}_j,t) B_i^{b_i^j}(\mathbf{x}+\mathbf{c}_j,t)[1 - N_i(\mathbf{x}+\mathbf{c}_j,t)]^{1-s_i^j}, \tag{VIII.5}$$

where r_i^j, b_i^j, and s_i^j describe the state of the particle moving with velocity $\mathbf{c}_i$ at site $\mathbf{x}+\mathbf{c}_j$. To solve the Boltzmann equation (VIII.4), one assumes that both R_i and B_i

may be expanded around a state of local equilibrium. Thus we write

$$R_i = R_i^{(0)} + R_i^{(1)} + \ldots, \qquad B_i = B_i^{(0)} + B_i^{(1)} + \ldots, \tag{VIII.6}$$

where $R_i^{(n)}$ is of order n. We assume the local equilibrium

$$R_i^{(0)} = \theta d, \qquad B_i^{(0)} = (1-\theta)d. \tag{VIII.7}$$

At next order in the gradient expansion we have

$$R_i^{(1)} = \gamma c_{i\alpha}\partial_\alpha(\theta d), \qquad R_i^{(1)} = -\gamma c_{i\alpha}\partial_\alpha(\theta d), \tag{VIII.8}$$

where γ is a constant to be determined. We also define $P^{(0)}(s)$ and $H^{(0)}(S)$ to be zero-order expressions obtained by substituting equation (VIII.7) into equations (VII.5) and (VIII.5).

Substituting equation (VIII.6) into the Boltzmann equation (VIII.4) and equating terms of first order in gradient, one obtains

$$\sum_\alpha c_{i\alpha}\partial_\alpha R_i^{(0)} = \sum_{s,s',\mathcal{S}} (r_i' - r_i) A(s,s',\mathcal{S}) \left[\mathcal{B}_1 H^{(0)}(\mathcal{S}) + (\mathcal{B}_2 + \mathcal{B}_3) P^{(0)}(s)\right] \tag{VIII.9}$$

where

$$\mathcal{B}_1 = \left[\frac{\partial P(s)}{\partial R_j(\mathbf{x})} R_j^{(1)}(\mathbf{x}) + \frac{\partial P(s)}{\partial B_j(\mathbf{x})} B_j^{(1)}(\mathbf{x})\right], \tag{VIII.10}$$

$$\begin{aligned}\mathcal{B}_2 \;=\; & \frac{\partial H(\mathcal{S})}{\partial R_j(\mathbf{x}+\mathbf{c}_k)}\left[R_j^{(0)}(\mathbf{x}+\mathbf{c}_k) - R_j^{(0)}(\mathbf{x})\right] + \\ & \frac{\partial H(\mathcal{S})}{\partial B_j(\mathbf{x}+\mathbf{c}_k)}\left[B_j^{(0)}(\mathbf{x}+\mathbf{c}_k) - B_j^{(0)}(\mathbf{x})\right],\end{aligned} \tag{VIII.11}$$

and

$$\mathcal{B}_3 = \frac{\partial H(\mathcal{S})}{\partial R_j(\mathbf{x}+\mathbf{c}_k)} R_j^{(1)}(\mathbf{x}+\mathbf{c}_k) + \frac{\partial H(\mathcal{S})}{\partial B_j(\mathbf{x}+\mathbf{c}_k)} B_j^{(1)}(\mathbf{x}+\mathbf{c}_k). \tag{VIII.12}$$

The term $\mathcal{B}_1$ does not include interactions with the neighborhood distribution $H(\mathcal{S})$, and is thus related to ordinary lattice-gas diffusion (Burges and Zaleski, 1987). $\mathcal{B}_2$ is specific to the ILG. The terms in brackets in equation (VIII.11) arise from the fact that θ can vary in space, while $\mathcal{B}_2$ itself results from the tendency of the ILG collisions to

maximize color flux in the direction of like color. Lastly, $\mathcal{B}_3$ just indicates the change in neighbor configurations due to a distortion of equilibrium at the neighboring sites. Consideration of the symmetries in equations (VIII.8) shows that terms on the right-hand-side of equation (VIII.12) cancel, and thus $\mathcal{B}_3 = 0$.

Substitution of equations (VIII.10) and (VIII.11) in equation (VIII.9) then yields

$$c_{i\alpha} = \left(\gamma \mathcal{A}_{ij}^{(1)} + \mathcal{A}_{ij}^{(2)}\right) c_{j\alpha}, \tag{VIII.13}$$

in which $\mathcal{A}_{ij}^{(1)}$ and $\mathcal{A}_{ij}^{(2)}$ are complicated expressions containing contributions from $\mathcal{B}_1$ and $\mathcal{B}_2$, respectively (Rothman and Zaleski, 1989). To calculate the evolution of θ, and therefore the diffusivity, one notes that

$$\sum_{i=0}^{6} R_i(\mathbf{x}+\mathbf{c}_i, t+1) = \sum_{i=0}^{6} R_i(\mathbf{x}, t), \tag{VIII.14}$$

or, in words, that collisions conserve the number of red particles. Expanding this equation via substition of equations (VIII.6), (VIII.7), (VIII.8), and (VIII.13), and using the scaling $\partial_t = \mathcal{O}(\nabla^2)$, one obtains

$$\partial_t \theta = D\nabla^2\theta, \tag{VIII.15}$$

where

$$D = -\frac{3}{14} - \frac{3\gamma}{7}. \tag{VIII.16}$$

Solution of equation (VIII.13) for γ thus gives the diffusion coefficient D. Note that, as we have seen in earlier calculations of viscosity and diffusivity, we have once again a "propagation" contribution given by the first term in equation (VIII.16). The second term, via γ, thus determines the sign of D. Numerical solutions for $D(d,\theta)$ are described below.

2. ILG phase diagram: the spinodal curve

Figure 27 shows solutions to $D(d,\theta) = 0$ (Rothman and Zaleski, 1989). The region of $D > 0$ corresponds to combinations of d and θ for which the mixed state is stable,

while the region where $D < 0$ corresponds to instability of the mixed state, and thus stability of the two-phase, or phase-separated, state.

Figure 27 also compares this theoretical estimate of the phase boundary to results of numerical *domain growth* experiments (Rothman and Zaleski, 1989). In these experiments, the ILG was initialized as a homogeneous mixture for various combinations of d and θ, and the two-dimensional power-spectrum,

$$S(\mathbf{k},t) = \frac{1}{n_x n_y} \left| \sum_{\mathbf{x}} e^{i2\pi \mathbf{k}\cdot\mathbf{x}} \{[\rho_r(\mathbf{x},t) - \rho_b(\mathbf{x},t)] - \rho(2\theta - 1)\} \right|^2, \qquad \text{(VIII.17)}$$

was computed at discrete time intervals. Here ρ is again the average number of particles per site, ρ_r and ρ_b are the number of red particles and blue particles, respectively, at time t at a site with coordinates given by $\mathbf{x}$, $\mathbf{k}$ is the discrete wave vector, and n_x and n_y are the number of lattice sites in the x and y direction, respectively. To determine whether the mixed state is stable or unstable, the circular average $\hat{S}(k,t) = \langle S(\mathbf{k},t) \rangle$, where $k = |\mathbf{k}|$, was computed, from which the time-varying length-scale,

$$R(t) = \frac{1}{\sum_k k \hat{S}(k,t)} \qquad \text{(VIII.18)}$$

was obtained. Regions in the d, θ plane for which $R(t)$ grows with time are the regions where the mixed state is unstable, and correspond in principle to the regions where $D < 0$. Comparison of the empirical curve bounding the region of growing $R(t)$ with the Boltzmann approximation of the $D(d,\theta) = 0$ is seen to be qualitatively, but not quantitatively, good.

As in the estimates of surface tension described in Section VII., one factor limiting the accuracy of quantitative comparison of the theoretical and empirical curves in Figure 27 is the nature of the Boltzmann approximation: the correlations that were neglected may play a significant role in the mechanisms that drive phase separation. A second limiting factor is the quality of the empirical curve itself, which necessarily involves some subjective judgment for the location of the points of marginal stability. However, independent empirical measurements of $D(d, \theta = 0.5)$ qualitatively confirm the empirical estimates of $D(d,\theta) = 0$ obtained from measurements

of $R(t)$ (Rothman and Zaleski, 1989). Moreover, the same critical density, $d_c \approx 0.2$ for $\theta = 0.5$, was obtained not only from the Boltzmann approximation for D, the domain-growth experiments, and the numerical measurements of D, but also the theoretical surface-tension calculation detailed in Section VII.2.. We have thus described four independent means of quantifying the phase transition from the mixed to the unmixed state in the ILG. (A fifth method, the direct measurement of surface tension, could also be cited, but its accuracy near the critical point is suspect.)

We believe that this phase transition is analogous to the spinodal decomposition described in Section V.B.1.. Specifically, the early stages of spinodal decomposition in both the real world and the ILG are the result of uphill diffusion. However, one major difference remains: real spinodal decomposition is driven energetically, while ILG spinodal decomposition is driven by its time-irreversible microdynamics.

C. Isotropy and self-similarity

The characterisations of phase-separating automata given above in Sections VIII.A. and VIII.B. relate only to equilibrium aspects of phase transitions in these models. Below, we consider some dynamical aspects. Specifically, we ask whether the phase separation patterns are self-similar with respect to time, as is known both from experiments and calculations from other, non-hydrodynamic models (Gunton et al., 1983). We also consider whether these phase separation patterns are isotropic. We summarise calculations made with the ILG (Rothman, 1990a), but note that similar results have been obtained with the liquid-gas model (Appert et al., 1991).

To investigate the question of isotropy, an ensemble of 1500 independent realizations of the 2-D power spectrum $S(\mathbf{k},t)$ of equation (VIII.17) were computed and then averaged, for the case $n_x = n_y = 128$, $d = 0.7$, and $\theta = 0.33$. In each of the 1500 simulations, the initial condition was a homogeneous random mixture. A typical result of this averaging is shown in Figure 28a, where here $t = 1000$ time steps after initialisation of the simulation. Inspection of the spectral contours shows that

although at high wavenumbers one can see a trace of the hexagonal symmetry of the triangular lattice, at low wavenumbers the contours are circular, and therefore indicative of low-wavenumber isotropy. The high-wavenumber anisotropy is expected, not only because of the anisotropy of the lattice itself, but also because of the anisotropy of surface tension detailed earlier in Section VII.2.. At low wavenumbers the isotropy of viscous stress appears to win over the anisotropy of surface tension. Indeed, one may show that in a system with 6-fold anisotropy of surface tension of a magnitude comparable to the maximum anisotropy derived in Section VII.2., the resulting angle-dependence in radius should be less than 1% (Appert and Zaleski, 1993).

Assuming isotropy, one may, as already detailed above, compute circular averages $\hat{S}(k,t)$ for different time steps t. A typical result is in Figure 28b, where the parameters are again the same as in Figure 28a, and the averages are computed at times $t = 100, 200, \ldots, 1000$. One sees that as time progresses, the wavenumber k_m of the maximum value of $\hat{S}(k)$ decreases, while $\hat{S}(k_m)$ itself increases.

The phase separating mixture should be self-similar with respect to time: small bubbles should interact with small bubbles at early times in much the same way that big bubbles interact with other big bubbles at late times. In other words, given the characteristic size k_m^{-1}, there should be a scaling function $F(k/k_m)$ such that (Marro et al., 1979; Lebowitz et al., 1982; Furukawa, 1985; Fratzl and Lebowitz, 1989)

$$\hat{S}(k,t) = Ak_m^{-2}(t)F(k/k_m(t)), \qquad \text{(VIII.19)}$$

where A is a time-independent constant chosen to make $F(1) = 1$. Figure 28c shows precisely this behavior: the scaled structure functions $A^{-1}k_m^2\hat{S}(k,t)$ are plotted as a function of the dimensionless wavenumber $k/k_m(t)$, showing no discernible dependence on time. The scaled structure functions also qualitatively conform to a scaling function F proposed recently by Fratzl and Lebowitz (Fratzl and Lebowitz, 1989).

IX. Numerical simulations

As we state in the introduction, lattice-gas models of fluids serve not only as interesting conceptual, or "toy," models, but also as tools for the numerical simulation of certain problems in hydrodynamics. In this section, we review some recent work in which numerical experiments with lattice gases have illustrated this dual role.

Generally, computer simulations of lattice gases have been performed to either verify theoretical predictions for the behavior of the models, or to explore new areas of hydrodynamics and statistical mechanics. Here we emphasise the latter, with particular reference to numerical experiments with multiphase lattice gases. However, as we have made clear in the previous sections, multiphase lattice gases are predicated on the simpler, FHP models. It is thus instructive to first review some of the simulation work that has been performed with these simpler models.

A. Simulations of single-component fluids

1. Two-dimensional fluids

a. Flows in simple geometries After the introduction of the FHP model in 1986, a flurry of papers followed that demonstrated, with varying degrees of quantitative analysis, the striking similarity between lattice-gas simulations and known solutions of the Navier-Stokes equations. The first such work, an oft-referenced but unpublished report by d'Humières, Lallemand, and Shimomura (d'Humières et al., 1985a), verified the Boltzmann estimates of the shear and bulk viscosities of the FHP model, thus testing linear hydrodynamics. Later work by d'Humières and Lallemand qualitatively verified nonlinear hydrodynamics by investigating flow in the inlet length of a channel (d'Humières and Lallemand, 1986), flow past a backward-facing step (d'Humières and Lallemand, 1987), and the von Karman street resulting from two-dimensional flow past a flat plate (Figure 3) (d'Humières et al., 1985b). The work on channel flow is particularly notable for its successful quantitative comparison with

the analytic solution due to Schlichting (Schlichting, 1979).

b. Statistical mechanics and hydrodynamics To date, probably the most precise quantitative investigation of the hydrodynamic properties of the two-dimensional FHP gas is the work of Kadanoff, McNamara, and Zanetti (Kadanoff et al., 1989). By simulating Poiseuille flow in a channel, they not only qualitatively verified hydrodynamics—i.e., the predicted parabolic profile—but they also probed the dependence of the shear viscosity on the size of the system. Earlier studies (Alder and Wainwright, 1970; Dorfman and Cohen, 1970; Pomeau and Résibois, 1975; Forster et al., 1977) had predicted a logarithmic divergence of the viscosity of two-dimensional fluids as the system size increases. This divergence arises from microscopic fluctuations; crudely speaking, it results from the fact that fluctuations create eddies, which then advect the fluctuations elsewhere, creating new fluctuations and new eddies. The prediction of the divergence of 2-D transport coefficients relies on a first-order perturbation theory and mode-mode coupling (Pomeau and Résibois, 1975; Forster et al., 1977). Though the prediction had been motivated by observations of power-law decays of correlation functions of fluctuations in molecular dynamics (the so-called "long-time tails" (Alder and Wainwright, 1970)), no hydrodynamic simulation had ever been performed to verify it. The molecular dynamics method contains too much detail to efficiently perform such a test, whereas direct numerical solutions of the Navier-Stokes equations do not include microscopic fluctuations, making them inappropriate for studying such phenomena. The problem thus appeared well-suited for the lattice-gas method, and results of the work did indeed confirm the predicted logarithmic divergence. However, discrepancies between theory and simulation found in the course of the work were due in part to the spurious "staggered-momentum" invariant (Section IV.C.3.) in the two-dimensional FHP model, and thus required some reworking of the hydrodynamic theory of lattice gases (Zanetti, 1989) to improve the correspondence between the predicted logarithmic divergence and the behavior actually obtained in the simulations.

Simulations of a similar spirit have also been performed to measure the velocity-velocity autocorrelation function for a single tagged particle (Frenkel and Ernst, 1989; Van der Hoef and Frenkel, 1990; Noulles and Boon, 1991). The lattice gas is a particularly useful tool for such measurements because of the vast gain in efficiency compared to classical simulations of molecular dynamics. In particular, the fast algorithm of Frenkel and Ernst (Frenkel and Ernst, 1989) is of general interest. To describe it, consider the dynamics of a model with a single colored particle. Let $\nu_i(\mathbf{x}, t)$ be the Boolean variable indicating the presence of that particle. A Green-Kubo integral of the form of equation (IV.102) relates the correlation function

$$C_{ij}(t) = \langle \nu_i(\mathbf{x}, t)\nu_j(0, 0)\rangle_{eq} \qquad \text{(IX.1)}$$

to the self-diffusion coefficient (Brito et al., 1991). In collisions involving the tagged particle we consider that the model is *colorblind*; i.e., that the dynamics are indistinguishable from that of a given one-color model. Let the one-color model be FHP-I. In head-on collisions, the tagged particle may leave in one of four possible directions, depending on which pair collision is chosen and where in the pair the tagged particle goes. Consider that the direction is chosen at random among the two possible directions. The fast algorithm of Frenkel and Ernst may be defined as follows.

Notice that in equilibrium, the correlation function $C_{ij}(\mathbf{x}, t)$ we want to compute is identical to the the conditional probability $W_{ij}(\mathbf{x}, t)$ of finding the particle at $\mathbf{x}$ at time t provided it was initially at $\mathbf{x} = 0$; thus

$$C_{ij}(\mathbf{x}, t) = W_{ij}(\mathbf{x}, t)\langle \nu_j(0, 0)\rangle. \qquad \text{(IX.2)}$$

This conditional probability may be approached using a single simulation of the one-color model. To perform such a simulation, all particle variables n_i (without tags) are defined. We know that $C_{ij}(\mathbf{x}, 0) = 1$ for $\mathbf{x} = 0$ and 0 otherwise. For time 1, we may compute the probability W_{ij} of finding the tagged particle in one of the sites adjacent to 0, *given the evolution of the colorblind model*. At each of the subsequent steps a real number W_{ij} is propagated from site to site.

This method is far superior to a method which would propagate ν_i, as one has to do in molecular dynamics. A speed up of 6-10 orders of magnitude may be obtained (Frenkel and Ernst, 1989; Frenkel, 1990). Using this method, a $1/t$ decay at intermediate ranges and an asymptotic $1/[t\sqrt{(t)}]$ decay was found by Naitoh (Naitoh et al., 1990). Comparison with Boltzmann predictions at short times and mode-coupling theory at longer times were made (Naitoh and Ernst, 1991; Naitoh et al., 1991), and although in qualitative agreement, they showed a quantitative disagreement with mode-coupling theory. Fully four-dimensional calculations also yield correct scaling of the correlations, which decay like t^{-2}, but the amplitude differs by 15-60% from the predictions of mode-coupling theory (Van der Hoef et al., 1992).

c. **Flows in complex geometries** Although the original interest in lattice-gas simulations was motivated in part by the desire for a new tool for the simulation of turbulence, it soon became evident that the method offered important advantages for the simulations of flows through complex geometries, whether turbulent or not. Indeed, in the first published report of lattice-gas simulations, it was stated in the conclusion that "the microscopic nature of collisions with walls permits the placement of obstacles [in the flow] of any shape without any difficulty (d'Humières et al., 1985b)," contrary, for example, to the more "traditional" finite-element method. As introduced at that time and studied in detail later (Cornubert et al., 1991), the "no-slip" boundary condition is easily implemented simply by having particles bounce back from a wall with a velocity opposite to that with which they arrive at the wall.

The relative algorithmic ease with which flows through complex geometries could be simulated soon led to two important applications of the lattice-gas method: simulations of flows through porous media (Rothman, 1988; Chen et al., 1991a; Kohring, 1991b; Kohring, 1991c; Kohring, 1991a), and simulations of suspensions (Ladd and Colvin, 1988; Ladd and Frenkel, 1990). In both of these applications, the emphasis has been on the empirical investigation of the dependence of bulk properties of flows on aspects of microscopic disorder.

In typical lattice-gas studies of flow through porous media (for example, see Figure 4), one constructs a geometric model of a disordered porous geometry, simulates the flow through this complex medium, and then measures the functional dependence of flow rate on the applied force. The linear relation,

$$J = \frac{k}{\mu} X, \tag{IX.3}$$

known as *Darcy's law*, is expected to relate the flux J to the force X, via the dynamic viscosity μ and the conductivity, or *permeability*, coefficient k. In general, the objective is to determine how the permeability varies with some characteristic of geometric disorder. Early two-dimensional results served first to verify that Darcy's law is indeed observed in lattice-gas simulations of flow through porous media (Rothman, 1988), and, later, to measure, for example, the dependence of permeability on void fraction in a random 2-D array of cylinders (Kohring, 1991a). However, due to topological limitations, studies of flow through 2-D microscopic models of porous media have limited physical significance, and the most important work in this area has been three dimensional (see, for example, the lattice-Boltzmann simulations of Cancelliere et al. (Cancelliere et al., 1990)).

Work with suspensions has proceeded along similar lines. One creates, for example, a suspension of hard disks by allowing the boundaries of the disks to move in response to linear and angular momentum absorbed by the disks. The first such work resulted in a measurement of the dependence of the bulk (suspension) viscosity on the concentration of the suspension, and included not only an observation of Einstein's low-concentration estimate of the viscosity, but also measurements at high concentrations (Ladd and Colvin, 1988). Subsequent work (in three dimensions) has included measurements of the drag coefficient of dilute and concentrated suspensions (Ladd and Frenkel, 1990).

2. Three-dimensional fluids

The current vanguard of lattice-gas simulations is three-dimensional flows. Work in 3-D requires considerably more algorithmic sophistication than in 2-D, for many reasons. The root of the problem is the FCHC lattice (Section IV.A.3.): because there are 24 vertices per node, there are thus $2^{24} \approx 1.6 \times 10^7$ possible configurations at each site. This poses two practical problems. The first, and more fundamental, problem is to choose the collision rules. Whereas the possible choices are relatively easily enumerated in two dimensions, this is not the case for the FCHC lattice, nor is it *a priori* obvious which among the possible outcomes of a conservative collision to choose. The second problem is the implementation of the collision rules. A naive formulation of a collision table would require 2^{24} entries, which may be prohibitively large, particularly on parallel computing architectures. Decomposition of the collision rules into Boolean logic likewise appears formidable, though some interesting ideas have recently been advanced (Molvig et al., 1992; Teixeira, 1992).

Fortunately, however, much progress has been made toward the resolution of these practical problems. In a series of early papers, Hénon showed how one may estimate, via a Boltzmann approximation, the viscosity that results from any set of collision rules for the FCHC model (Hénon, 1987b), after which he presented a method for choosing the particular set of collision rules that minimises viscosity (and thus maximizes the Reynolds number) (Hénon, 1989). Hénon's work also detailed many of the symmetries inherent in the FCHC lattice, thus guiding the development of memory-efficient collision tables. The most substantial reduction in the size of the FCHC collision tables, however, was achieved only recently, by Somers and Rem (Somers and Rem, 1992). They made the remarkable observation that, because any pair of velocities $\mathbf{c}_i$ and $-\mathbf{c}_i$ is unchanged by any isometry (i.e., any sequence of rotations and inversions) of the FCHC lattice, the FCHC collision rules can be encoded as a sequence of tables that are themselves encoded by at most 12 bits of information, rather than the naive requirement of 24 bits. This clever trick was then shown to

result in a memory requirement of only about 100 kilobytes for the collision tables.

Although the outlook for FCHC lattice-gas simulations is now encouraging, lattice-gas simulations to date in 3-D are much less numerous than in two dimensions. Some work may nonetheless be noted (see also Section IX.B.4.). For example, following the first published simulations of the FCHC model by Rivet and his collaborators (Rivet et al., 1988), Rivet has recently performed an extensive lattice-gas study of 3-D flows past a cylinder (Rivet, 1991). His results show spontaneous symmetry breaking leading to oblique vortex shedding.

B. Simulations of multicomponent fluids

Lattice-gas simulations of multicomponent fluids—in particular, the interacting lattice gases discussed in the previous sections—have to date generally focused on one of two goals. In the first, interest has centered on the statistical-mechanical properties of the models, notably their ability to simulate phase transitions in conjunction with hydrodynamics. In the second, the objective has been to determine aggregate properties of flows of multiphase fluids, with special emphasis on multiphase flow through porous media. In this section, we review recent highlights of both aspects of this work. We begin with a summary of work on pattern formation in sheared fluids undergoing phase separation. We then review recent lattice-gas studies of multiphase flow through porous media. Finally, we conclude with brief remarks on how this work may be extended to hydrodynamic applications of greater complexity, and include in that discussion a brief description of recently introduced 3-D multiphase lattice-gas models.

1. Phase separation and hydrodynamics

In Section VIII.C. we have already discussed dynamical aspects of phase separation in lattice-gas models. However, the patterns of growth due to phase separation were discussed in the absence of any external hydrodynamic forcing. It is also interesting

to ask how growth, itself a nonlinear, nonequilibrium process, interacts with hydrodynamics. One experimental setting in which to consider this question is phase separation during pipe (or channel) flow. In this case, simulations of an immiscible lattice-gas mixture of fluids of different viscosities have demonstrated the tendency of the more viscous fluid to flow in the center of the channel (Stockman et al., 1990).

Another experimental setting of interest is phase separation in a shear flow (Chan et al., 1988; Imaeda et al., 1984; Ohta et al., 1990; Hashimoto et al., 1988). Perhaps most fundamentally, one can ask whether the role of fluctuations in initiating phase separation is enhanced, diminished, or unchanged in the presence of a weak or strong shear flow. Somewhat more practically, one may also investigate rheological properties of the sheared mixture (Onuki, 1987; Krall et al., 1989; Krall et al., 1992). Lastly, one can ask how the pattern formation due to growth is itself affected by a shear flow (Chan et al., 1988). Thus far, lattice-gas simulations have been performed to address the latter two of these three issues (Rothman, 1990a; Rothman, 1991); here we review the work on patterns.

A 2-D shear flow was created with the ILG with the geometry shown in Figure 29 (Rothman, 1990a). Specifically, on a lattice with $L = n_y$ lattice units in the vertical direction and $W = n_x\sqrt{3}/2 = n_y\sqrt{3}$ lattice units in the horizontal direction, the average y-velocity in the vertical column located at $x = 0$ is held at $u_y = -u_0$, while the average y-velocity in the middle column, located at $x = W/2$, is held at $u_y = u_0$. By making boundaries periodic in both directions, a "V"-shaped velocity profile,

$$u_y = \begin{cases} C(x - W/4) & 0 \le x < W/2 \\ -C(x - 3W/4) & W/2 \le x < W, \end{cases} \qquad \text{(IX.4)}$$

is obtained, where the shear rate $C = 4u_0/W$.

Phase separation patterns produced in real space are shown in Figure 30. Here $d = 0.70$, $\theta = 0.35$, $n_x = 512$, $n_y = 256$, and the viscosities are equal. There are 3 cases. In the first, for purposes of comparison, there is no shear. The state of the system is shown at an early and late time; one sees a system of circular bubbles, the

size of which grow with time. In the second case, the shear rate $C = C_0 = 9.02 \times 10^{-4}$ results from setting $u_0 = 0.10$, while in the third case $C = 1.5C_0$. The patterns with shear are markedly different than those without. Two features stand out in the sheared patterns. First, after a sufficiently long time, the normally circular bubbles are deformed into elliptical bubbles, each of which is approximately oriented at 45 degrees to the flow direction. This *orientational* order is a simple consequence of expansion and compression along the principal axes of strain; it manifests itself at approximately the time when the differential velocity CR across a bubble of size R becomes greater than the rate of bubble growth, dR/dt. The second, and more interesting, feature of the sheared growth is the *positional* ordering that results at late times. This structure appears as the ordered stacks of elliptical bubbles, each stack being separated from the nearest stack by a distance comparable to the length of the major axis of the average ellipse.

Both the positional and orientational ordering are quantified by the computations of the power spectra $S(\mathbf{k}, t)$ (see equation (VIII.17)) shown in Figure 31. $S(\mathbf{k})$ is computed by calculating the power spectra $S_L(\mathbf{k})$ and $S_R(\mathbf{k})$ of the left and right halves of the box, respectively, and then averaging the two by setting $S(\mathbf{k}) = (1/2)[S_L(\mathbf{k}) + S_R(-\mathbf{k})]$. Again, there are three cases, corresponding to the three cases of Figure 30; now, however, the results represent the average of 40 independent simulations rather than just one. The first spectrum (Figure 31a) shows the isotropic unsheared case: one sees roughly circular contours. In the two cases of shear, however, one sees the signature of both the orientational and positional ordering. The former appears simply as elliptical contours. The latter, however, is somewhat more subtle: it manifests itself in $S(\mathbf{k})$ as the dropoff of spectral power in the region roughly aligned along the major axes of the elliptical spectra. This corresponds to a relative lack of correlation in the patterns along the direction parallel to the minor axes of the real-space elliptical bubbles, and a relatively high correlation in the direction parallel to their major axes.

These details of the power spectra in Figure 31 qualitatively match the results from light-scattering experiments performed by Chan, Perrot, and Beysens (Chan et al., 1988). The real-space patterns in Figure 30, obtained only by simulation, allow interpretation of those results. Bubbles separated by a distance less than a bubble size will interact strongly in a shear flow, causing them to be relatively frozen in place compared to bubbles far from one another. Thus one obtains the positional ordering. Similar effects are also known in sheared colloidal suspensions (Brady and Bossis, 1988), granular fluids (Hopkins and Louge, 1991), and molecular dynamics (Evans et al., 1984; Loose and Hess, 1989).

2. Multiphase flow through porous media

The second principal problem area in which lattice-gas models of fluid mixtures have provided useful tools for simulation is multiphase flow through porous media. Here the origin of complexity in the problem lies not so much with the fluid mixture itself but rather with the disordered medium through which it flows.

The problem of multiphase flow through porous media appears in varied contexts in both the natural sciences and engineering applications (Sheidegger, 1960; Bear, 1972). It is perhaps most ubiquitous in the earth sciences, where it appears, for example, in hydrological studies of the flow of aqueous mixtures through sand, soil, and rocks near the earth's surface, in geophysical studies of the flow of magmatic mixtures in the earth's mantle (Richter and McKensie, 1984), and in petroleum-engineering studies of the flow of oil, water, and gas through the pore space of sandstones in hydrocarbon reservoirs. There are principally two areas of interest for physics here. First, as summarised in the book by Feder (Feder, 1988), despite the fact that flow through porous media is slow and viscous and the Reynolds number is quite low, multiphase flow through porous media can result in fascinating interfacial instabilities, many of which can have a fractal geometry. Second is the estimation of constitutive equations. Although it is well understood that multiphase flow at the pore scale obeys the Navier-

Stokes equations, the equations obeyed by the *volume-averaged* multiphase flow at a scale much larger than that of a pore remain unknown.

Of these two issues, thus far only the question of constitutive equations has been addressed by lattice-gas simulations. The macroscopic equation typically employed to describe immiscible multiphase flow through porous media is based on the assumption that the volume-averaged flow of the two fluids obeys a multiphase extension of Darcy's law, equation (IX.3), given by (Sheidegger, 1960; Bear, 1972)

$$J_i(\theta) = l_i(\theta)\frac{k}{\mu_i}X_i. \qquad \text{(IX.5)}$$

Here the flux J_i of the ith fluid is proportional to the force X_i applied to the ith fluid as in Darcy's law, but with an additional prefactor $0 \le l_i \le 1$ that depends on the portion θ of the void space occupied by, say, fluid 1. Thus equation (IX.5) describes a two-fluid flow in which each fluid flows through a fictitious porous medium constructed from the union of the real porous medium and the void space occupied by the other fluid, with the same boundary condition at solid-fluid and fluid-fluid interfaces. The so-called "relative-permeability" coefficient l_i is then thought to describe empirically how the flux of the ith fluid depends on the portion of the void space that it occupies.

Although equation (IX.5) has survived as an engineering approximation (with varying degrees of success) for well over 50 years, it has been subjected to much criticism. For example, Adler and Brenner (Adler and Brenner, 1988) point out that equation (IX.5) implicitly assumes that fluid-fluid interfaces do not change with increasing force (or flow rate), thereby justifying the assumption of a linear force-flux relation. Moreover, de Gennes (de Gennes, 1983) remarks that equation (IX.5) can be valid only if contact angles are finite, in which case neither fluid completely wets the solid surface, the fluid-fluid interfacial area is small, and thus viscous fluid-fluid coupling is negligible. If this were not the case, then one would instead expect that the appropriate multiphase generalisation of Darcy's law would be

$$J_i = \sum_j L_{ij}(\theta)X_j, \qquad \text{(IX.6)}$$

where

$$L_{ij}(\theta) = l_{ij}(\theta)\frac{k}{\mu_j}. \qquad \text{(IX.7)}$$

Then, by an extension of Onsager's reciprocity principle to a system far from equilibrium, one would expect that

$$L_{ij} = L_{ji}. \qquad \text{(IX.8)}$$

Because of the aforementioned confusion concerning the theoretical description of the macroscopic flow, lattice-gas simulations have been able to make considerable progress. Two questions have been addressed (Rothman, 1990b; Gunstensen and Rothman, 1993). First is the question of whether the force-flux relation is indeed linear. Second is the question of whether the Onsager reciprocity (IX.8) holds, if there is indeed a linear regime of the flow.

The work was carried out first in two dimensions, using the immiscible lattice gas (Rothman, 1990b), and then in three dimensions, using a lattice-Boltzmann model of immiscible fluids (Gunstensen and Rothman, 1993). An example of a 3-D lattice-Boltzmannn simulation of multiphase flow thorough a porous medium is shown in Figure 32. The results from extensive simulations performed at constant concentration were contrary to either equation (IX.5) or (IX.3). Specifically, the simulations showed that at low flow rates and at intermediate concentrations of non-wetting fluid, the response of flux to force can be highly nonlinear. The source of the nonlinearity is capillarity: bubbles of a size larger than a characteristic pore size require a finite driving force to be pushed through the porous medium, or otherwise they do not move. This behavior can be interpreted as the physical manifestation of a failure to meet the implicit assumption, mentioned above, of interfacial configurations that are independent of the driving force.

Simulations did show, however, that for sufficiently strong forcing such that the nonlinearity due to surface tension is overcome, the fluxes are indeed related linearly to the forces. Interestingly, in both 2-D and 3-D the cross terms L_{ij} were found to exhibit a magnitude that could be comparable to the diagonal coefficients, showing clearly

that equation (IX.6) is a better description of the macroscopic flow than equation (IX.5). Moreover, within the limitations of the accuracy of the numerical experiments, the cross terms were found to be equal, thereby confirming the expectation of the Onsager reciprocity. Previous laboratory experiments by Kalaydjian (Kalaydjian, 1990) had also observed the Onsager reciprocity, allowing both results to qualitatively confirm each other.

3. Three-phase flow, emulsions, and sedimentation

The previous examples have shown how multiphase lattice gases may be used to study flows of two kinds of two-phase fluids; in one case, a phase-separating fluid which is itself subjected to external forcing, and in the other case an immiscible fluid mixture flowing through a complex geometry. Here we discuss examples of how fluid mixtures of an even greater complexity may be simulated using models based on the ILG.

Our point of departure for these more complex fluids is a model of a mixture of three immiscible fluids (Gunstensen and Rothman, 1991b). A three-phase model is easily constructed from a generalisation of the ILG collision rule given by equations (III.1), (III.2), and (III.3). The three species of fluids are represented by Boolean variables $(n_{ij})_{0\le i\le 6}$, where the additional subscript $j = 1,2,3$ is used to index the fluid species, say, red, green, or blue, and an exclusion rule holds such that for any velocity i, at most one n_{ij} may equal one. On the two-dimensional triangular lattice, the flux of species j is then

$$\mathbf{q}_j[n_{0j}(\mathbf{x}),\ldots,n_{6j}(\mathbf{x})] = \sum_{i=1}^{6}\mathbf{c}_i n_{ij}(\mathbf{x}), \qquad j = 1,2,3, \qquad \text{(IX.9)}$$

while the local gradient of the jth species is proportional to

$$\mathbf{f}_j = \sum_k \mathbf{c}_k \sum_i n_{ij}(\mathbf{x}+\mathbf{c}_k), \qquad j = 1,2,3. \qquad \text{(IX.10)}$$

The result of a collision, $(n_{ij}) \to (n'_{ij})$, is then the choice of configuration that maximises the weighted sum

$$\sum_j \alpha_j \mathbf{f}_j \cdot \mathbf{q}_j(n'_{0j},\ldots,n'_{6j}), \qquad \text{(IX.11)}$$

subject to conservation of each species,

$$\sum_i n'_{ij} = \sum_i n_{ij}, \qquad j = 1, 2, 3, \tag{IX.12}$$

and conservation of total momentum,

$$\sum_i \sum_j \mathbf{c}_i n'_{ij} = \sum_i \sum_j \mathbf{c}_i n_{ij}. \tag{IX.13}$$

The coefficients α_j are chosen to set the three surface tensions, σ_{12}, σ_{13}, and σ_{23}. If the α_j's are all equal, then so are the surface tensions, and three-phase contact lines (or points in two dimensions) are not only stable, but act as the point of contact for three interfaces, each making an angle of $2\pi/3$ with respect to the others. If, on the other hand, the α_j are chosen so that the surface tensions are such that, say, $\sigma_{13}+\sigma_{12} < \sigma_{23}$, i.e., the sum of two are less than the third, then three-phase contact points are not stable, and the mixture is in equilibrium when a bubble of species 2 and another bubble of species 3 reside in a "sea" of species 1. One choice of coefficients that yields this situation is $\alpha_1 = -0.5$, $\alpha_2 = 1$, and $\alpha_3 = 1$ (Gunstensen and Rothman, 1991b).

The three-fluid model has met with preliminary success for both phase separation and flow through porous media (Gunstensen and Rothman, 1991b). Three-fluid phase separation is of intrinsic interest because the pattern formation can be considerably different than in the two-fluid counterpart, due to the influence of the relative values of the surface tensions. The problem of three-phase flow through porous media is, on the other hand, of significant practical interest, since it concerns how oil, water, and gas flow in subterranean reservoirs. Here basic questions concern the form of the three-fluid analog of Darcy's law, and how it depends not only on the relative concentrations of the three fluids and their surface tensions, but also on their wetting properties. Some progress towards unraveling some of these issues has been achieved with a lattice-Boltzmann version of the three-fluid model (Gunstensen, 1992).

While three fluids may seem complicated enough, an important extension to the three-phase model is made by allowing for N fluids, where N is arbitrarily large (Rothman, 1992). Such a model follows from the observation that, for the case of

one rest particle, at most 7 different fluid species may be present at any site on the two-dimensional triangular lattice. Then, by defining one of the N species to always be the suspending or interstitial fluid (species 1), and the two locally most numerous species other than the interstitial fluid to be species 2 and 3, a collision may be performed using the three-fluid rule detailed above, in which the weights α_j are set to make three-phase contact points unstable. We refer to this model as a *many-bubble model*, because $N-1$ bubbles are formed in a sea of the Nth fluid.

An example of a typical unforced simulation of the many-bubble model is shown in Figure 33. Each bubble, shown in black, undergoes a random walk due to the statistical noise of the lattice gas, and is unable to coalesce with any of the other bubbles. This model thus simulates the hydrodynamic interactions of $N-1$ deformable bodies, or, in other words, certain aspects of the hydrodynamics of emulsions. In real emulsions, chemical agents on interfaces, such as surfactants, act to impede the coalescence of bubbles. Here instead bubble coalescence is disallowed by the surface tension that is created between different phases.

Figure 34 shows an application of the many-bubble model to a problem of two-component sedimentation (Rothman and Kadanoff, 1993). Here the red bubbles are positively buoyant and rise, while the blue bubbles are negatively buoyant and fall. The initial condition of the simulation was a random mixture of red and blue bubbles. One finds that for this concentration of bubbles and acceleration of gravity, the mixture is unstable and segregrates into regions composed primarily of red bubbles or blue bubbles, as shown in Figure 34. Such instabilities in two-component sedimentation are known from experiments and, to a lesser extent, from theory (Whitmore, 1955; Weiland et al., 1984; Batchelor and Janse van Rensburg, 1986). Insight gained from an understanding of the sedimentation instability in Figure 34 allowed the construction of an interesting model of high-Prandtl number thermal convection (Rothman and Kadanoff, 1993).

4. Three-dimensional flows

Three-dimensional work with the lattice-gas models of mixtures introduced in Section III. remains in its infancy, but some progress may nonetheless be reported.

a. Liquid-gas model Construction of a 3-D liquid-gas model requires little complexity beyond that of the plain FCHC lattice gas (Appert et al., 1993a). After performing the "standard" FCHC collisions, the interacting collisions are performed by implementing equations (V.26) and (V.27) in the FCHC geometry. Figure 35 illustrates an example of phase separation in the 3-D liquid-gas model. For this simulation the interaction range is $r = 8$ and the box size is 64^3. Because the range of the interaction is large, the most unstable wavelength for the initial stage of spinodal decomposition is of the order of the size of the box. Thus the system decomposes into just one lump of liquid and one lump of gas.

b. Immiscible lattice gas In contrast to the liquid-gas model, the ILG requires some significant reworking to allow for practical implementation in three dimensions. The first 3-D ILG was proposed and implemented by Rem and Somers (Rem and Somers, 1989). They used a model, subsequently explained in more detail in 2-D (Somers and Rem, 1991), that employs colored "holes" in addition to colored particles. The use of holes allowed them to obtain an estimate of the color gradient from the local site itself, rather than having to obtain information from neighboring sites as in equation (III.2).

An alternative model for a 3-D ILG has recently been proposed (Olson and Rothman, 1993). If only one color is present at a site, then the model performs the usual FCHC collision. If instead two colors are present, then the model splits the ILG collision into two steps in the following way. Colorless particle pairs $n_i = r_i + b_i$ and $n_{-i} = r_{-i} + b_{-i}$ are formed, where, as in Section V.C.1.a., $\mathbf{c}_i = -\mathbf{c}_{-i}$. In the first step, occupied pairs ($n_i = n_{-i} = 1$) and unoccupied pairs ($n_i = n_{-i} = 0$) are rearranged to new values n'_i, n'_{-i}, such that only exchanges between occupied and unoccupied pairs

are allowed, and that the exchange maximises

$$\sum_{i=1}^{24}(c_{i\parallel}^2 - c_{i\perp}^2)n'_i. \qquad \text{(IX.14)}$$

The quantities $c_{i\parallel}$ and $c_{i\perp}$ are the projection of velocity $\mathbf{c}_i$ on the direction parallel and perpendicular, respectively, to a previously obtained discretised color gradient. Performing this rearrangement of occupied and unoccupied pairs requires the construction of a lookup table indexed by only 12 bits, rather than the full 24 bits of the FCHC model itself, or the 48 bits of the colored FCHC model. The second step of the collision is the redistribution of color (i.e., $r'_i \to r''_i$ and $b'_i \to b''_i$). This is performed such that the flux of color $\sum_i \mathbf{c}_i(r''_i - b''_i)$ is as much as possible in the direction of the discretised color gradient, under the constraints that color is conserved and that $n''_i = n'_i$. Thus the colorblind configuration changes only in step one, which provides surface tension, whereas the color is rearranged on the new colorblind configuration in step two, which acts to minimize the diffusivity of color.

Figure 36 shows an example of an immiscible mixture in a shear flow simulated with the two-step 3-D ILG described above. The simulation shown is a 3D version of the 2D sheared phase separation of Figure 30. Due to the competition between shear and surface tension in 3D, the bubbles reach a characteristic size R after which, statistically, they grow no larger. The capillary number $\mathrm{Ca} = \mu RC/\sigma \sim 1$, where C is the shear rate and μ is the viscosity of both fluid phases.

X. Conclusions

This review has had two principal objectives. First, we have attempted to give a broad overview of the achievements to date that have followed the introduction of lattice-gas automata as a model of the Navier-Stokes equations. Second, we have emphasized the contributions to the field that have come from lattice-gas models of phase separation. In concluding, it seems appropriate to objectively evaluate the progress that has been made, and to point out some interesting areas of research that lie ahead. We do not repeat any bibliographic citations below that have already been given; the reader is instead referred to the detailed descriptions given in the body of the review.

To an extent, progress within the field of lattice-gas automata may be considered to lie within either statistical mechanics, hydrodynamics, or both. In addition, one may speak of purely methodological advances that create progress in either of these two disciplines. Below we follow such a categorisation with the hope of creating some order in an otherwise highly interdisciplinary field.

A. Statistical mechanics

It is perhaps easy for the casual observer of the field to overlook the connection of lattice-gas automata to statistical mechanics in favor of its relation to hydrodynamics. Nevertheless, many of the more impressive achievements to arise from the field have been of considerable importance to statistical mechanics.

First, as already emphasised in the introduction and detailed in Section IV., lattice gases have provided a simplified microscopic model from which the hydrodynamic equations may be derived. An understanding of this "discretised" molecular dynamics then leads a researcher to consider one of two directions. The first path, perhaps the longer of the two, leads to gratification that the macroscopically complex world is really not so complicated after all, and encourages one to find equally simple models

of complexity in other fields. The second path is somewhat more practical: it leads one to consider what questions, if any, this simplified molecular dynamics can help answer.

We have already indicated, primarily in Section IX.A.1.b., how lattice-gas simulations have helped address basic questions in statistical mechanics. We simply reiterate here that one of the major achievements has been the experimental (i.e., numerical) verification of the prediction of the divergence of transport coefficients in two-dimensional fluids, while another has been the observation of long-time tails in velocity autocorrelation functions. Results such as these have been possible precisely because the lattice gas acts as a kind of midway point between molecular dynamics and the Navier-Stokes equations, and therefore serves as an efficient tool to investigate problems where microscopic fluctuations interact with macroscopic hydrodynamics.

The lattice gas is also an interesting conceptual tool with which to consider not only the relationship between the microscopic and macroscopic levels of hydrodynamics, but also the microscopic and macroscopic descriptions of phase transitions in hydrodynamic models. The models of phase separation discussed at length in the latter half of this review are unconventional in that they are microscopically irreversible. Precisely what impact this loss of reversibility has on the macroscopic aspects of phase transitions, however, remains to be quantified. Indeed, we find these dynamical models of phase transitions to lie somewhere in an imaginary continuum between the classical phase transitions of statistical physics and bifurcations in nonlinear dynamical systems.

As emphasised in this review, equilibrium aspects of phase transitions in lattice-gas models of phase separation are much better understood than nonequilibrium aspects. To gain some insight into both aspects of the phase transitions, and therefore make an attempt at understanding where the spectre of irreversibility might make itself known, models that are even simpler than the ones we have presented here have been proposed. These have, in one case, made it easier to prove theorems concerning

phase separation (Lebowitz et al., 1991), and in another, provided a somewhat greater efficiency of simulation (Alexander et al., 1992). It is fair to say, however, that despite much effort (see also Bussemaker and Ernst (Bussemaker and Ernst, 1993) and Gerits et al. (Gerits et al., 1993)), the effect of irreversibility remains to be quantified.

Also not yet systematically investigated is the behavior of lattice-gas models of phase transitions in the vicinity of their critical points. Whereas some work on critical exponents exists (Chan and Liang, 1990), the nature of hydrodynamic transport at the critical point is not yet known.

B. Hydrodynamics

Progress in lattice-gas methodology, though general in its applicability, is most obviously interwined with progress in hydrodynamics itself. Thus it .s appropriate to first make some observations about technical advances.

Progress in the development of lattice-gas methods has indeed been enormous. With respect to single-phase lattice gases, the lion's share of effort has been devoted to making 3-D computations practical. This has demanded not only a thorough understanding of the relationship of collision rules to transport coefficients, but even more importantly the invention of practical schemes for encoding these collision rules in lookup tables (or sequences of logical operations) that are of manageable size. Due to the advances reviewed in Sections IV.A.3. and IX.A.2., we can now say that these issues are resolved.

One methodological issue still in its infancy, however, is the use of special-purpose computers for lattice-gas (or, more generally, cellular automata) computations. Early attempts (Toffoli and Margolus, 1987; Clouqueur and d'Humières, 1987) led to excitement but not wide use. A more recent and much awaited machine (Toffoli and Margolus, 1991) has, at the time of writing, just led to its first prototype; its applicability to scientific computation appears promising, but remains to be exploited.

With respect to models of phase separation, much of the technical progress has

been devoted to the construction, and consequent understanding, of 2-D models. Three-dimensional models, however, are only beginning to be considered, and may appropriately be deemed to be at one of the methodological forefronts of the field. While formulations and preliminary simulations of these models exist, their properties remain to be characterized, both theoretically and empirically.

Given this wealth of models, a genuine practical concern is their relative efficiency compared to competing methods for the simulation of hydrodynamics. The efficiency of a given method involves the memory usage and central processor unit (CPU) time required by a simulation, the flexibility of the numerical scheme, and the cost of development and maintenance of the computer codes. The perceived elegance and simplicity of the method may also be of value.

A few attempts have been made to discuss specifically the memory and CPU costs of lattice-gas simulations. Orszag and Yakhot (Orszag and Yakhot, 1986) arrived at pessimistic conclusions for high Reynolds-number lattice-gas simulations of single-phase flow. However, a different estimate of the efficiency of the lattice gas arrived at mixed conclusions (Zaleski, 1989).

Aside from these semi-quantitative studies of efficiency, a consensus among workers in the field is emerging. First, for general-purpose simulations without geometric complexity, the lattice gas does not appear to have any computational advantages. In fact, CPU efficiency depends strongly on noise level and Mach number (Zaleski, 1989), and it is easy to reach values of these parameters for which lattice-gas simulations become much more costly than their classical counterparts. Second, flows in media with complex boundaries are easier to simulate, from the viewpoint of programming, with lattice gases, but may not have any particular advantages in speed. The same is probably roughly true for simulations of multiphase flow, especially with complex boundaries. However, compared to classical methods, there is the additional limitation that only certain specific parameter ranges can be simulated with lattice gases. Thus, as far as efficiency is concerned, the status of the lattice-gas method is not

unlike that of an analog device: it is very appealing for some specific problems, but not very flexible.

With these opinions stated, several caveats are in order. As emphasized in Section IX., if one desires only qualitative results for quantities obtained by averaging over an entire simulation box (as in, for example, many studies of single and multiple phase flow through porous media), the lattice gas may possibly be very efficient. This efficiency arises from the tradeoff of microscopic noise for algorithmic efficiency: in principle, one averages out the noise at the scale of the boxsize. Secondly, particular characteristics of lattice gases, such as fluctuations, or the phase transitions in the models discussed here, offer a natural framework for studying certain problems (e.g., the influence of fluctuations or phase transitions on hydrodynamics) that are relatively difficult to approach otherwise. Third, there is the hope that special-purpose computers for lattice-gas computations may someday lead to unprecedented efficiencies, but this has yet to be concretely established. Lastly, we note that the lattice-Boltzmann method (see Appendix C) overcomes many of the inefficiencies of the lattice-gas method. This gain in efficiency, however, comes at the cost of the loss of some of the more interesting properties of lattice gases, such as intrinsic fluctuations and phase transitions.

Thus we turn to the question of what has been learned about hydrodynamics from simulations of lattice gases. Here the results are quite positive, and perhaps reflect less any intrinsic efficiency of the method but more the fascination of physicists and others for its innate simplicity. We have already reviewed many of the principal achievements in Section IX.. Here we simply restate that in the majority of cases, the exciting lattice-gas simulations of hydrodynamics have exploited one of the strengths of the method: fluctuations (to excite bifurcations), complex geometries (to exploit the ease of coding boundary conditions), and phase transitions. In these areas, we find the field not only quite healthy, but in anticipation of more important, three-dimensional results yet to come.

XI. Acknowledgments

We are indebted to a large number of students and colleagues for advice, encouragement, ideas, and, above all, collaborations. Among the many, we wish to especially acknowledge our interactions with C. Adler, E. Aharanov, B. Alder, C. Appert, B. Boghosian, J.-P. Boon, C. Burges, G. Doolen, M. Ernst, U. Frisch, A. Gunstensen, F. Hayot, M. Hénon, D. d'Humières, L. Kadanoff, R. Kapral, J. M. Keller, A. Lawniczak, P. Lallemand, J. Lebowitz, D. Levermore, N. Margolus, J. Olson, L. di Pietro, Y. Pomeau, V. Pot, E. Presutti, P. Rem, A. Rucklidge, J. Somers, S. Succi, T. Toffoli, G. Vichniac, and G. Zanetti. We would also like to thank D. d'Humières for his critical reading of the manuscript. This work was supported in part by NSF Grants 9017062-EAR and 9218819-EAR, NATO Travel Grant 10756, and the sponsors of the MIT Porous Flow Project.

XII. Appendix A: Symmetry and related geometrical properties

The purpose of this appendix is to prove several useful symmetry results. We shall prove that for regular Bravais lattices all the symmetry assumptions on tensors necessary for the derivation of lattice-gas hydrodynamics without isotropy are true. Moreover, we shall prove that certain lattices also yield isotropic hydrodynamics.

A. Regular Bravais lattices

This section and the next consist mainly of definitions and are reminders of geometry and crystallography. As in section IV.A.1. we define a *Bravais lattice* as a lattice for which each point has identical surroundings. It is easy to prove that all Bravais lattices are periodic. Thus the lattice is invariant by a set of translations $\{T_{\mathbf{w}}\}$ with

$$\mathbf{w} = n_1\mathbf{u}_1 + \cdots + n_h\mathbf{u}_h \qquad \text{(A1)}$$

where all the n_i are variable integers and the $\mathbf{u}_i$ are fixed vectors. It is easily proved that all Bravais lattices are periodic. The $\mathbf{u}_i$ are a set of generating vectors of the lattice.

Bravais lattices possess a *point symmetry group* $\mathcal{G}$, i.e. a group of congruent transformations that leaves a point of the lattice fixed and the lattice globally invariant. The symmetry properties of the lattices are better grasped as the set of symmetry properties formed by a set of neighbors or *polytope*. (The definitions of regular polygons and polyhedra are well known. They can be extended to yield a definition of higher dimensional, regular polytopes as shown in the section below.)

Consider a reference point O of the lattice and a set of neighbors M_i of O. We take this set to be large enough to contain a set of generating vectors. The lattice may be obtained by the reproduction of the pattern formed by the lattice and the neighbors M_i. The set M_i forms a polytope in D-dimensional space. The vectors generating

vectors $\mathbf{c}_i = OM_i$ alternately characterise the lattice. They are identical to a set of velocity vectors for particles in the main text of the article. However here we consider a set of $\mathbf{c}_i$ all of identical norm $\|\mathbf{c}_i\| = c$. We further require that the polytope formed by the M_i or the $\mathbf{c}_i$ be *regular*. A Bravais lattice having a set of neighbors that form a regular polytope will be called a regular Bravais lattice. In this article and in almost all the lattice gas literature (the only exceptions are unpublished attempts to define lattice gases on quasilattices) one deals only with regular Bravais lattices.

B. Polytopes

There are only five regular polyhedra or *Platonic solids*: the tetrahedron {3,3}, octahedron {3,4}, cube {4,3}, dodecahedron {5,3}, and icosahedron {3,5}. The *Schläfi symbol* $\{p,q\}$ indicates the number p of edges around each face and the number q of edges attached to each vertex.

For a D dimensional polytope P we will denote "Et $P(\mathbf{c}_i)$" (Berger, 1978) the $D-1$ polytope formed by all the vertices adjacent to a given vertex $\mathbf{c}_i$. An example of this construction is given for the cube in Figure 37. The notion of a regular polytope may be given a recursive definition. The definition of a regular polygon is obvious. The polytope P is *regular* when all the Et $P(\mathbf{c}_i)$ formed about the various vertices are all regular and transformed into each other by isometries. We may then write Et P for Et $P(\mathbf{c}_i)$ when orientation is not important. The *Schläfi symbol* $\{p,q,r,\ldots,z\}$ of a regular polytope P is then formed by the number of edges p of a face and the Schläfi symbol $\{q,r,\ldots,z\}$ of Et P.

The group of symmetries $\mathcal{G}$ of a regular polytope is found for instance in Coxeter (Coxeter, 1977). The polytope is left invariant by reversal about the origin (parity transformation for all the coordinates) and rotations about pairs of opposite vertices.

C. Tensor symmetries

1. Isotropic tensors

Let R^β_α be the matrix of any linear space transformation R. Let $T_{\alpha_1\cdots\alpha_k}$ be a rank k tensor covariant in all indices. It is transformed by R as

$$T'_{\alpha_1\cdots\alpha_k} = T_{\beta_1\cdots\beta_k} R^{\beta_1}_{\alpha_1}\cdots R^{\beta_k}_{\alpha_k}. \tag{A2}$$

A tensor is isotropic if it is invariant by all congruent transformations, i.e. all transformations in the orthogonal group $O(D)$. We now seek to determine all rank k isotropic tensors symmetric by exchange of their k indices up to rank 4. By equation (A2) the tensors $I_{\alpha\beta} = \delta_{\alpha\beta}$ and $\Delta_{\alpha\beta\gamma\delta} = (\delta_{\alpha\beta}\delta_{\gamma\delta} + \delta_{\alpha\gamma}\delta_{\beta\delta} + \delta_{\alpha\delta}\delta_{\beta\gamma})$ are isotropic. We shall show that all the sought tensors are proportional to I in rank 2 or Δ in rank 4.

Consider a rank k isotropic tensor R. All the lattices we consider have at least *cubic symmetry*: they are invariant by parity transformation of all coordinates and by permutation of coordinates. The consequences of cubic symmetry are developed in mechanics textbooks such as Aris (Aris, 1962). We give the derivation here for completeness. In rank 2 cubic symmetry immediately yields $T_{12} = 0$ and $T_{\alpha\alpha} = T_{11}$ for all α (no summation). For tensors of order 4 we find only four independent terms T_{1111}, T_{1212}, T_{1221}, and T_{1122}. The last three are identical since we may permute the indices. Thus the general tensor invariant under cubic symmetry is

$$T_{\alpha\beta\gamma\delta} = \lambda(\delta_{\alpha\beta}\delta_{\gamma\delta} + \delta_{\alpha\gamma}\delta_{\beta\delta} + \delta_{\alpha\delta}\delta_{\beta\gamma}) + \mu\delta_{\alpha\beta}\delta_{\gamma\delta}\delta_{\alpha\gamma} \tag{A3}$$

Consider now a $\pi/3$ rotation. Using equation (A2) we find

$$T_{1111} = \frac{1}{16}T_{1111} + \frac{9}{4}T_{1122} + \frac{9}{16}T_{2222} \tag{A4}$$

and

$$T_{1111} = 3T_{1122}. \tag{A5}$$

We thus find $\mu = 0$ in (A3). The rotation leaves all components other than 1 and 2 invariant. It is thus a general D-dimensional result.

2. Tensors invariant under the lattice point symmetries

We now apply symmetry consideration to find the form of tensors having the discrete group $\mathcal{G}$ of lattice symmetries.

a. Tensor invariant under the whole group All the lattices we consider, except the hexagonal lattice, have cubic symmetry which readily gives the form of the 4th rank tensors to be (A3). The hexagonal case is readily treated as in the section above using parity, $\pi/3$ and $2\pi/3$ rotations (Landau and Lifshits, 1959b). We find that on the hexagonal lattice $T_{\alpha\beta\gamma\delta}$ is proportional to Δ and thus isotropic. In the square and cubic case the general form is (A3).

In the FCHC case we have cubic symmetry and symmetry about the plane defined by $x_1 + x_2 + x_3 + x_4 = 0$, i.e. the transformation

$$\sigma : x_\alpha \to x'_\alpha = x_\alpha - \frac{1}{2}\sum_\beta x_\beta. \tag{A6}$$

The scalar obtained by contracting R with the vector $y = (2, 0, 0, 0)$ is also invariant by σ. Thus

$$y^\alpha y^\beta y^\gamma y^\delta T_{\alpha\beta\gamma\delta} = y'^\alpha y'^\beta y'^\gamma y'^\delta T_{\alpha\beta\gamma\delta} \tag{A7}$$

where $y' = (1, -1, -1, -1)$. Inserting (A3) we find 16μ on the left-hand side and 4μ on the right-hand side of (A7). Thus $\mu = 0$ and $T_{\alpha\beta\gamma\delta}$ is isotropic.

b. Tensor attached to a given lattice vector It is of interest to determine the general form of a tensor $t_{i\alpha\beta}$ attached to the lattice vector $\mathbf{c}_i$ and symmetric in the indices $\alpha\beta$. A tensor attached to a vector is invariant by lattice symmetries in $\mathcal{G}$ that leave that vector $\mathbf{c}_i$ invariant. Its form is of interest to determine the general form of perturbations at first order in the Chapman-Enskog expansion. It is determined by the following theorem, which is an extension of similar results by Frisch et al. (Frisch et al., 1987) and Hénon (Hénon, 1987b).

Theorem 1 *Let $\mathcal{L}$ be a regular Bravais lattice and let $\mathbf{c}_i$ be the generating vectors. Let $\mathcal{G}$ be the symmetry group of the regular polytope formed by the $\mathbf{c}_i$. Let $t_{i\alpha\beta}$ be a*

tensor symmetric in the indices and invariant by all symmetries in $\mathcal{G}$ leaving c_i fixed. Then $t_{\alpha\beta}$ is of the form

$$t_{\alpha\beta} = \lambda c_{i\alpha} c_{i\beta} + \mu \delta_{\alpha\beta}. \tag{A8}$$

Proof:

We first introduce a definition, then proceed with 3 lemmas. The following definition is classical: *A set of transformations of space R^D which leaves no linear subspace invariant is called an irreducible family (Boerner, 1955).*

Lemma 1 *The symmetry group $\mathcal{G}$ of a regular polytope is an irreducible family.*

We work by recursion on the dimension D of space. We start the recursion in dimension $D = 2$. There we deal with regular polygons such as triangles, squares, etc., which have at least $n = 3$ vertices. The symmetry group of a regular polygon is a group of rotations and reflections. It is obviously irreducible: consider any linear subspace of R^2, i.e. any straight line, and rotate it by less than $2\pi/n$. Since no line is invariant, the group is irreducible.

We now continue the recursion for $D > 2$. Consider an arbitrary regular polytope P and the regular polytope Et $P(c_i)$ formed around c_i. By recursion the symmetry group $\mathcal{G}_i$ of Et $P(c_i)$ is irreducible. Moreover Et $P(c_i)$ is in some $D-1$ subspace Π_i of R^D. We reason by the absurd and suppose that $\mathcal{G}$ is reducible. Let Π' be a subspace of R^D invariant by $\mathcal{G}$.

We will first assume that Π' is neither in Π_i nor is it the line L_i parallel to c_i (see Figure 38). Notice $\mathcal{G}$ contains $\mathcal{G}_i$. Thus Π' is also invariant by $\mathcal{G}_i$. The action of $\mathcal{G}_i$ on Π' is shown in Figure 38. The intersection L of Π' and Π_i must also be invariant by $\mathcal{G}_i$. But since L is a subspace of Π_i the assumption that $\mathcal{G}_i$ is irreducible is violated. Thus Π' is either equal to Π_i or is the line parallel to c_i.

Thus if $\mathcal{G}$ is reducible it may only leave Π and c_i invariant. Take now another vertex c_j such that c_i is in Et $P(c_j)$. Et $P(c_j)$ has a symmetry group $\mathcal{G}_j$ that exchanges c_i with yet another vector c_k as in Figure 39. Otherwise c_i would be invariant by

$\mathcal{G}_j$ and $\mathcal{G}_j$ would not be irreducible. But we assumed that c_i was invariant, hence a contradiction.

Comment This lemma may be intuitively understood in the following way. If the symmetry group of a polytope leaves a subspace Π invariant, this means that this subspace is somehow "privileged" with respect to the others. Although it is a symmetry axis, it cannot be "rotated" into another similar subspace. This is contradictory with our idea of the symmetry of a regular polytope.

Lemma 2 (Schurr) *If a transformation commutes with all transformations in an irreducible family it is proportional to identity.*

A proof of this famous lemma of the representation theory of groups may be found in Boerner (Boerner, 1955).

Lemma 3 *If a symmetric twice covariant tensor $t_{\alpha\beta}$ is invariant by a congruent transformation R then the corresponding linear operator M with the same matrix $M^\beta_\alpha = t_{\alpha\beta}$ commutes with R.*

Indeed we have from (A2)

$$t_{\alpha\beta} = t_{\alpha'\beta'} R^{\alpha'}_{\alpha} R^{\beta'}_{\beta} \tag{A9}$$

$$M^\beta_\alpha = M^{\beta'}_{\alpha'} R^{\alpha'}_{\alpha} R^{\beta'}_{\beta} \tag{A10}$$

Since for a congruent transformation $(R^{-1})^\beta_\alpha = R^\alpha_\beta$ we have

$$M^\beta_\alpha = R^{\alpha'}_{\alpha} M^{\beta'}_{\alpha'} (R^{-1})^{\beta}_{\beta'} \tag{A11}$$

which may be written $MR = RM$.

We may now prove the theorem. Consider the hyperplane Π_i orthogonal to c_i. Consider the linear map A of matrix $t_{\alpha\beta}$. It is not difficult to show that A leaves the line L_i generated by c_i invariant. It thus also leaves Π_i globally invariant. It is symmetric and thus of the form

$$A = \begin{pmatrix} \lambda & 0 \\ 0 & B \end{pmatrix} \tag{A12}$$

where B is a transformation acting on Π_i. The hypothesis in the theorem is that $t_{i\alpha\beta}$ is invariant by all transformations in the subgroup $\mathcal{G}_i$. From that statement and Lemma 3, B commutes with all the transformations in the group $\mathcal{G}_i$ defined in the theorem. From the discussion in Section A.2., $\mathcal{G}_i$ is the symmetry group of Et P. From Lemma 1, $\mathcal{G}_i$ is irreducible. Since $t_{i\alpha\beta}$ restricted to Π_i (in other words B) commutes with all the members of an irreducible family it is proportional to $\delta_{\alpha\beta}$ by Schurr's lemma.

D. Tensors formed with generating vectors

Lattice gas theory involves the r-th order tensors

$$E^{(r)}_{\alpha_1 \ldots \alpha_r} = \sum_i c_{i\alpha_1} \cdots c_{i\alpha_r}. \tag{A13}$$

We are now able to determine these tensors to order 3:

$$\sum_i c_{i\alpha} = 0, \tag{A14}$$

$$\sum_i c_{i\alpha} c_{i\beta} = \frac{bc^2}{D} \delta_{\alpha\beta}, \tag{A15}$$

$$\sum_i c_{i\alpha} c_{i\beta} c_{i\gamma} = 0. \tag{A16}$$

Expressions (A14) and (A16) are obtained by parity. It suffices to remark that vectors $\mathbf{c}_i$ appear in pairs: for each $\mathbf{c}_i$ there is another opposed vector $\mathbf{c}_j = -\mathbf{c}_i$. To derive expression (A15) we first remark that the tensor on the left-hand side is invariant by the symmetry group $\mathcal{G}$ of the lattice. Since all the lattices we consider have at least hypercubic symmetry the results of Section XII.C.1. imply that $E^{(2)}$ is proportional to I. The coefficient of proportionality is readily found by summation over α and β.

For those lattices determined in Section XII.C.2. to yield isotropic fourth order tensors we also have

$$E^{(4)} = K\Delta. \tag{A17}$$

The proportionality constant K is determined by summing (A17) over all indices to yield

$$\sum_i c_{i\alpha} c_{i\beta} c_{i\gamma} c_{i\delta} = \frac{bc^4}{D(D+2)} (\delta_{\alpha\beta}\delta_{\gamma\delta} + \delta_{\alpha\gamma}\delta_{\beta\delta} + \delta_{\alpha\delta}\delta_{\beta\gamma}). \tag{A18}$$

The form of $E^{(4)}$ in the square and cubic case is given by (A3).

XIII. Appendix B: A catalogue of properties of the lattice Boltzmann equation

A. Basic definitions

We consider the discrete Boltzmann equation of Section III.,

$$N_i(\mathbf{x}+\mathbf{c}_i, t+1) = N_i(\mathbf{x}, t) + \Delta_i[\mathbf{N}(\mathbf{x}, t)] \tag{B1}$$

where Δ is defined by

$$\Delta_i(\mathbf{N}) = \sum_{ss'}(s_i' - s_i)A(s, s')\prod_j N_j^{s_j}\bar{N}_j^{\bar{s}_j}. \tag{B2}$$

The transition rates A are all positive and have the following properties:

1. Conservation of probability:

$$\sum_{s'} A(s, s') = 1 \quad \text{for all} \quad s. \tag{B3}$$

2. Semi-detailed balance:

$$\sum_{s} A(s, s') = 1 \quad \text{for all} \quad s'. \tag{B4}$$

3. Invariance under the action of $\mathcal{G}$:

$$A(Rs, Rs') = A(s, s') \quad \text{for any isometry} \quad R \in \mathcal{G}. \tag{B5}$$

4. Mass conservation: $A(s, s')$ vanishes whenever the s, s' have different masses.

5. Momentum conservation: $A(s, s')$ vanishes whenever the s, s' have different momenta.

B. Symmetric expression for the linearized operator

Under the properties 1-4 above, the linearised operator Λ_{ij} defined by

$$\Lambda_{ij} = \left.\frac{\partial \Delta_i}{\partial N_j}\right|_{\mathbf{N}(\bullet)} \tag{B6}$$

is given by

$$\Lambda_{ij} = -\frac{1}{2}\sum_{ss'}(s_i' - s_i)(s_j' - s_j)A(s, s')d^{n-1}(1-d)^{b-n-1} \tag{B7}$$

where $n = \sum_i s_i$.

Proof. Notice first that

$$\frac{\partial N_j^{s_j}(1-N_j)^{(1-s_j)}}{\partial N_j} = 2s_j - 1$$

since s_j may be only 0 or 1. Then

$$\Lambda_{ij} = \sum_{ss'}(s_i' - s_i)(2s_j - 1)A(s, s')\prod_{k\neq i,j} N_k^{s_k}\bar{N}_k^{\bar{s}_k}.$$

Using the approximation $N_k \simeq d$ we obtain

$$\Lambda_{ij} = \sum_{ss'}(s_i' - s_i)(2s_j - 1)A(s, s')d^{1-s_j}(1-d)^{s_j}w(s)$$

where $w(s) = d^{n-1}(1-d)^{b-n-1}$ with the notations above. From conservation of mass

$$w(s)A(s, s') = w(s')A(s, s'). \tag{B8}$$

Then

$$\Lambda_{ij} = \sum_{ss'}(s_i' - s_i)[s_j(1-d) - (1-s_j)d]A(s, s')w(s) \tag{B9}$$

$$= \sum_{ss'}(s_i' - s_i)s_j A(s, s')w(s) + \Lambda_1, \tag{B10}$$

where, using (B8), then (B3) and (B4),

$$\begin{aligned}\Lambda_1 &= -\sum_{ss'}(s_i' - s_i)dA(s, s')w(s)\\ &= \sum_s s_i w(s)d\sum_{s'} A(s, s')\\ &\quad -\sum_{s'} s_i' w(s')d\sum_s A(s, s')\\ &= \sum_s s_i w(s)d - \sum_{s'} s_i' w(s')d\\ &= 0.\end{aligned} \tag{B11}$$

Similarly using (B3) and (B4) we obtain

$$\sum_{ss'} s'_i s'_j A(s,s') = \sum_{s,s'} s_i s_j A(s,s'). \qquad \text{(B12)}$$

We now show one last useful identity. Let R be rotation of $\mathcal{G}$ exchanging $\mathbf{c}_i$ and $\mathbf{c}_j$. Then $(Rs)_i = s_j$,$(Rs)_j = s_i$ and thus

$$\begin{aligned}\sum_{ss'} s'_i s_j A(s,s') &= \sum_{s,s'} s'_i s_j A(Rs, Rs') \\ &= \sum_{s,s'} s'_j s_i A(s,s'). \qquad \text{(B13)}\end{aligned}$$

From equations (B10), (B11), (B12), and (B13) the desired result (B7) obtains.

XIV. Appendix C: The lattice Boltzmann method

The lattice-Boltzmann method or Boltzmann lattice gas is a numerical method for the solution of the artificially compressible Navier-Stokes equations. It is inspired by lattice gases but is in some respects akin to an explicit finite-difference method. It has several advantages with respect to the lattice gas for the numerical solution of the Navier-Stokes equation. In this appendix we briefly describe the method and mention some of its applications. For further details we refer the reader to the references, especially the recent review written by Benzi et al. (Benzi et al., 1992).

We begin with a word of caution. There is a great deal of similarity between the Boltzmann *method* and the Boltzmann *theory* of "Boolean" lattice gases developed in Section IV.. Several definitions and expressions of the Boltzmann methods have counterparts in the theory of lattice gases based on the Boltzmann approximation. However the definitions in the Boltzmann method are motivated by the construction of a simulation scheme.

A. Basic definitions

Space is discretised just as in the lattice-gas automaton. A regular Bravais lattice $\mathcal{L}$ is given with a set of generating or velocity vectors $(\mathbf{c}_i)_{0\le i<b}$. The geometrical definitions and theorem of Appendix A are relevant here also. Typical lattices are the hexagonal and FCHC lattices as in the Boolean case. The basic dependent variables in the method are the population variables, written $N_i(\mathbf{x},t)$, where $\mathbf{x} \in \mathcal{L}$ and t is discrete time. We will not introduce rest particles or multiple-speed models in this appendix.

B. Evolution equations

Several evolution schemes have been proposed for the populations N_i. The simplest idea is to use the "full" lattice-Boltzmann equation (IV.18) to evolve the populations (McNamara and Zanetti, 1988). In a typical simulation hydrodynamical variables

$\mathbf{u}(\mathbf{x},0)$ and $\rho(\mathbf{x},0)$ are given at the initial time. Then initial populations $\mathbf{N}(\mathbf{x},0)$ are calculated using one or two terms in the multiple-scale expansion (IV.36). Populations are then evolved in time using equation (IV.18). Velocity and density may be recovered at each time step.

The above method is impractical when too many collision terms appear in the Boltzmann equation (IV.18). An alternative is then to define *a priori* a pseudo-linearized operator A_{ij} similar to the linearized operator defined in Section IV. (Higuera and Jimenez, 1989; Higuera and Succi, 1989; Succi et al., 1989; Benzi et al., 1992). We describe this operator in detail below. To each local population vector N we associate a pseudo-equilibrium distribution in the following way. First we define the local invariants associated with the population vector

$$\rho = \sum_i N_i, \tag{C1}$$

and momentum vector

$$\rho\mathbf{u} = \sum_i N_i \mathbf{c}_i. \tag{C2}$$

Then the pseudo-equilibrium $\mathbf{N}^{(0)}$ is defined by

$$N_i^{(0)} = d\left(1 + \frac{D}{c^2}c_{i\alpha}u_\alpha + G_0 Q_{i\alpha\beta}u_\alpha u_\beta\right) \tag{C3}$$

where $Q_{i\alpha\beta}$ is defined as in equation (IV.31) and G_0 is an adjustable constant. The above expression resembles the low-velocity expansion (IV.30). However it is not the approximation of any Fermi-Dirac distribution. It is easy to check, just as in the Boolean case, that this pseudo-equilibrium population has the same invariants as the original populations.

The Boltzmann equation with linearized collision operator is then

$$N_i(\mathbf{x}+\mathbf{c}_i, t+1) - N_i(\mathbf{x},t) = \sum_j A_{ij}(N_j(\mathbf{x},t) - N_j^{(0)}(\mathbf{x},t)). \tag{C4}$$

This equation fully defines the evolution scheme. The pseudo-equilibrium populations $N_j^{(0)}(\mathbf{x},t)$ that enter equation (C4) are calculated from the populations $N_j(\mathbf{x},t)$ using

definitions (C1), (C2), and (C3). The evolution scheme (C4) is entirely explicit since the populations at time $t+1$ may be obtained without any operator inversion. The simplest linearized operator is simply the scalar operator $A_{ij} = \omega\delta_{ij}$, where ω is an adjustable relaxation rate and δ_{ij} is the Kronecker symbol (Qian et al., 1992b).

C. Hydrodynamic limit

The hydrodynamic limit is obtained by an expansion identical to the multiple-scale or Chapman-Enskog expansion of Section IV.:

$$N_i = N_i^{(0)} + N_i^{(1)} + \cdots + N_i^{(n)} + \cdots. \tag{C5}$$

Here the 0-th order term is the pseudo-equilibrium density. Equations are obtained at each order by substituting expansion (C5) into the evolution equation (C4). These equations are formally identical to those derived in Section IV. with the equilibrium distribution and the linearized operator replaced by their Boltzmann-method counterparts. The continuity equation is obtained from conservation of mass. Thus the Euler and Navier-Stokes equations (IV.54) and (IV.88) are obtained. However the calculation of the coefficients is slightly different. The $g(\rho)$ factor is now a constant g_0. Using the continuity equation and (IV.88) we obtain

$$\rho\partial_t u_\alpha + g_0\rho\mathbf{u}\cdot\nabla u_\alpha = -\partial_\alpha[p(\rho,\mathbf{u}^2)] + \partial_\beta\left\{\nu_1[\partial_\beta(\rho u_\alpha) + \partial_\alpha(\rho u_\beta)]\right\} + \partial_\alpha\left[\nu_2 \mathrm{div}(\rho\mathbf{u})\right], \tag{C6}$$

where

$$g_0 = G_0\frac{2c^4}{D(D+2)} \tag{C7}$$

and

$$p(\rho,\mathbf{u}^2) = \frac{c^2}{D}\rho - G_0\frac{2bc^4}{D^2(D+2)}\mathbf{u}^2. \tag{C8}$$

We may choose G_0 in order to recover the Galilean-invariant form with $g_0 = 1$. Another choice may be to set $G_0 = 0$ when the zero Reynolds-number limit is sought. This removes the $\mathbf{u}^2$ dependence of the pressure and makes the calculation of the pseudo-equilibrium $N^{(0)}$ faster.

The equations are again pseudo-compressible and the incompressible limit is recovered for vanishingly small Mach numbers.

The prediction of the viscosity coefficients is simplified. In a Boltzmann scheme the eigenvector λ is directly available and the shear viscosity follows by equation (IV.90). For instance in the case of the trivial linearised operator $\lambda = \omega$. For the "user" of the method this amounts to setting directly the viscosity. The only restriction is one of stability: the viscosities may not be made too small without the creation of instabilities, which we discuss further below.

D. Construction of the linearized operator

The pseudo-linearized operator shares the following properties with the "true" Boolean linearized operator:

- *Symmetry.* We must have $A_{ij} = A_{ji}$.
- *Angle dependence.* A_{ij} may depend only on the angle $(\mathbf{c}_i, \mathbf{c}_j)$. On the hexagonal lattice, the matrix A_{ij} is thus a symmetric, circulant matrix.
- *Conservation laws.* Mass conservation implies that

$$\sum_j A_{ij} = 0 \tag{C9}$$

Momentum conservation is expressed by

$$\sum_j A_{ij}\mathbf{c}_j = 0. \tag{C10}$$

The linearised operator is completely characterised by these properties and its eigenvectors and eigenvalues. We give an example on the hexagonal lattice, where we may find all eigenvalues and eigenvectors easily. The possible angles are $k\pi/3$ for

$k = 0, 1, 2, 3$. Thus the general form of A is:

$$\mathrm{A} = \begin{pmatrix} a_0 & a_{60} & a_{120} & a_{180} & a_{120} & a_{60} \\ a_{60} & a_0 & a_{60} & a_{120} & a_{180} & a_{120} \\ a_{120} & a_{60} & a_0 & a_{60} & a_{120} & a_{180} \\ a_{180} & a_{120} & a_{60} & a_0 & a_{60} & a_{120} \\ a_{120} & a_{180} & a_{120} & a_{60} & a_0 & a_{60} \\ a_{60} & a_{120} & a_{180} & a_{120} & a_{60} & a_0 \end{pmatrix}. \tag{C11}$$

The indices in the coefficients a_θ refer to the angles between the directions i and j. Since the matrix A is circulant, its eigenvectors $(v_i^{(k)})_i$ are the 6-th roots of unity: the k-th eigenvector is $(v_j^{(k)})_j = (\zeta_k^j)_j$ with $\zeta_k = e^{ik\pi/3}$. The mass eigenvector is $(\zeta_0^j)_j = (1, 1, \ldots, 1)$ while $(\zeta_1^j)_j$ and $(\bar{\zeta}_1^j)_j$ are the two momentum eigenvectors $(c_{j\alpha})_j$. The vectors (ζ_2^j) and $(\bar{\zeta}_2^j)_j$ span the space generated by the three vectors $(Q_{j\alpha\beta})_j$. By symmetry they correspond to the same eigenvalue, λ, of the linearized operator. Finally the last eigenvector, $(\zeta_3^j)_j = ((-1)^j)_j$ has another eigenvalue τ. At this point we notice that the coefficients a_θ are not independent but are instead related by equations (C9) and (C10). This leaves two independent coefficients. The eigenvalues can be expressed in terms of these two coefficients (Bensi et al., 1992):

$$\lambda = 6(a_0 + a_{60}) \qquad \tau = -6(a_0 + 2a_{60}). \tag{C12}$$

From equation (IV.90) the shear viscosity ν_1 is obtained. The coefficient X is zero as in the Boolean case with no rest particles. The second viscosity then results from expression (IV.86).

E. Stability

An elementary stability analysis can be performed in the following way. Consider the special case where $N_i^{(0)}$ is everywhere constant. Let the populations N_i be a homogeneous perturbation of the form

$$\mathbf{N} = \mathbf{N}^{(0)} + \mathbf{V}\mathcal{S}^t, \tag{C13}$$

where V is an eigenvector of A. Then inserting into equation (C4) one obtains

$$(S-1)\mathbf{V} = \mathbf{AV}. \tag{C14}$$

As A is symmetric $S-1$ is a real eigenvalue. Linear stability requires that $|S| < 1$. Thus all eigenvalues ξ of A must verify $-2 < \xi < 0$. From equation (IV.90) this seems to allow all positive values of the shear viscosity, but see below. Equation (C14) also shows that if an eigenvalue is equal to -1 the resulting perturbation from equilibrium vanishes in one time step. This "superfast" convergence to equilibrium is one reason why $\tau = -1$ is chosen in practice.

The above analysis of stability is however rather incomplete. A more classical analysis of stability, akin to the stability analysis performed for finite-difference methods (Peyret and Taylor, 1983), could be made in the following way. Let the hydrodynamical variables vary as

$$\mathbf{u}(\mathbf{x},t) = \mathbf{u}_0 + \epsilon \mathbf{u}_1 \exp(i\mathbf{k}.\mathbf{x} + st) \tag{C15}$$

$$\rho(\mathbf{x},t) = \rho_0 + \epsilon \rho_1 \exp(i\mathbf{k}.\mathbf{x} + st) \tag{C16}$$

where k is a wavevector in the reciprocal lattice of $\mathcal{L}$. Such a full analysis is rather intricate and has been carried out only in the one-dimensional case (Qian et al., 1990). A condition very reminiscent of explicit finite difference schemes was found. It seems likely that it can be generalised to all Boltzmann models to yield

$$\nu > C_1 \mathbf{u}^2, \tag{C17}$$

where C_1 is a dimensionless number depending on the specific model considered. Our numerical experience seems to confirm this fact in a qualitative manner.

F. Multiphase models and other applications

A multiphase version of the lattice-Boltzmann method may be created by modifying the rules used to construct the ILG (Gunstensen et al., 1991). The resulting 3D

models (Gunstensen and Rothman, 1992) have led to interesting work on two-phase and three-phase flow in porous media (Gunstensen, 1992; Gunstensen and Rothman, 1993). Extensions of the method to cover multiple viscosities and densities have also been proposed (Grunau et al., 1993). It is also of interest to note that the multiphase Boltzmann models have inspired new devlopments in finite-difference methods for multiphase flow (Lafaurie et al., 1993).

The Boltzmann method may without too much trouble also be extended to multiple speeds and square lattices (Qian, 1990). The former extension is motivated in part by an interest in thermal models and the simulation of shocks.

Among the other applications of the lattice-Boltzmann method are viscous flow in 3D porous media (Cancelliere et al., 1990), thermal convection at high Rayleigh number (Massaioli et al., 1993), and flow behind a symmetric backward facing step (Cornubert, 1991). In the latter case an extensive analysis of the accuracy of the method has been performed (d'Humières and Cornubert, 1993). Dispersion in various flow geometries has also been studied (Flekkoy, 1993). A variety of other applications may be found in the review article of Benzi et al. (Benzi et al., 1992).

In closing this brief review of the lattice-Boltzmann method, we note that it has several practical advantages with respect to Boolean lattice gases. It is easier to extend to 3D. Galilean-invariance is restored easily which simplifies finite Reynolds-number calculations. The surface tension coefficient of the lattice-Boltzmann ILG may also be predicted theoretically with accuracy (Gunstensen et al., 1991; Paul et al., 1993). Finally, the lack of statistical noise in the Boltzmann method can bring a considerable gain of efficiency in problems where fluctuating hydrodynamics is neither of interest nor any possible use.

References

Adler, C., d'Humières, D., and Rothman, D. (1994). Surface tension and interface fluctuations in immiscible lattice gases. in press (January).

Adler, P. and Brenner, H. (1988). Multiphase flow in porous media. *Ann. Rev. Fluid Mech.*, 20:35–59.

Alder, B. and Wainwright, T. (1970). *Phys. Rev. Lett.*, 18:968.

Alexander, F. J., Edrei, I., Garrido, P. L., and Lebowitz, J. L. (1992). Phase transitions in a probabilistic cellular automaton: growth kinetics and critical properties. *J. Stat. Phys.*, 68:497–514.

Appert, C. (1993). *Transition de phase dynamique de type liquide-gaz et création d'interfaces dans un gaz sur réseau.* PhD thesis, Université de Paris 6.

Appert, C., d'Humières, D., Pot, V., and Zaleski, S. (1993a). Three dimensional lattice gas with minimal interactions. *Transport Theory and Statistical Physics, in press.*

Appert, C., d'Humières, D., and Zaleski, S. (1993b). Gas sur reseau avec interactions attractives minimales. *C. R. Acad. Sci. Paris*, 316:569–574.

Appert, C., Pot, V., and Zaleski, S. (1993c). Liquid-gas models on 2D and 3D lattices. preprint, to appear in the proceedings of NATO conference on Pattern Formation in Lattice-Gas Automata, June 1993.

Appert, C., Rothman, D., and Zaleski, S. (1991). A liquid-gas model on a lattice. *Physica D*, 47:85–96.

Appert, C. and Zaleski, S. (1990). A lattice gas with a liquid-gas transition. *Phys. Rev. Lett.*, 64:1.

Appert, C. and Zaleski, S. (1993). Dynamical liquid-gas phase transition. *J. Phys. II France*, 3:309–337.

Aris, R. (1962). *Vectors, tensors, and the basic equations of fluid mechanics.* Prentice-Hall.

Batchelor, G. K. (1967). *An Introduction to Fluid Dynamics.* Cambridge University Press, Cambridge.

Batchelor, G. K. and Janse van Rensburg, R. W. (1986). Structure formation in bidisperse sedimentation. *J. Fluid Mech.*, 166:379.

Baudet, C., Hulin, J. P., Lallemand, P., and d'Humières, D. (1989). Lattice-gas automata: a model for the simulation of dispersion phenomena. *Phys. Fluids A*, 1:507–512.

Bear, J. (1972). *Dynamics of Fluids in Porous Media.* Dover Publications, New York.

Benzi, R., Succi, S., and Vergassola, M. (1992). The lattice Boltzmann equation: Theory and applications. *Phys. Rep.*, 222:145–197.

Berger, M. (1978). *Géométrie.* F. Nathan, Paris.

Bernardin, D. (1992). Global invariants and equilibrium states in lattice gases. *J. Stat. Phys.*, 68:457–495.

Boerner, H. (1955). *Group Representations.* Springer, Berlin.

Brady, J. F. and Bossis, G. (1988). Stokesian dynamics. *Ann. Rev. Fluid Mech.*, 20:111.

Brito, D. and Ernst, M. H. (1991a). Propagating staggered waves in cellular automata fluids. *J. Phys. A*, 24:3331.

Brito, D., Ernst, M. H., and Kirkpatrick, T. R. (1991). Staggered diffusivites in lattice gas automata. *J. Stat. Phys.*, 62:283–295.

Brito, R. and Ernst, M. H. (1991b). Lattice gases in slab geometries. *Phys. Rev. A*, 44:8384.

Broadwell, J. E. (1964). Shock structure in a simple discrete velocity gas. *Phys. Fluids*, 7:1243–1247.

Burges, C. and Zaleski, S. (1987). Buoyant mixtures of cellular automaton gases. *Complex Systems*, 1:31.

Burgess, D., Hayot, F., and Saam, W. F. (1989). Interface fluctuations in a lattice gas. *Phys. Rev. A.*, 39:4695–4700.

Bussemaker, H. and Ernst, M. (1993). Phase separation in a biased lattice-gas automaton. preprint.

Cancelliere, A., Chang, C., Foti, E., Rothman, D., and Succi, S. (1990). The permeability of a random medium: Comparison of simulation with theory. *Physics of Fluids A*, 2:2085.

Chan, C. and Liang, N. Y. (1990). Critical phenomena in an immiscible lattice gas cellular automaton. *Europhys. Lett.*, 13:495–500.

Chan, C., Perrot, F., and Beysens, D. (1988). Effect of hydrodynamics on growth: spinodal decomposition under uniform shear flow. *Phys. Rev. Lett.*, 61:412.

Chapman, S. and Cowling, T. G. (1970). *The Mathematical theory of non-uniform gases, 3rd ed.* Cambridge University Press, Cambridge.

Chen, H. and Matthaeus, W. H. (1987). Cellular automaton formulation of passive scalar dynamics. *Phys. Fluids*, 30:1235–1237.

Chen, S., Diemer, K., Doolen, G., Eggert, K., Fu, C., Gutman, S., and Travis, B. J. (1991a). Lattice gas automata for flow through porous media. *Physica D*, 47:72–84.

Chen, S., Doolen, G., Eggert, K., Grunau, D., and Loh, E. (1991b). Local lattice-gas model for immiscible fluids. *Phys. Rev. A*, 43:7053–7056.

Chopard, B. and Dros, M. (1988). Cellular automata model for heat conduction in a fluid. *Phys. Lett.*, A126:476–480.

Chorin, J. D. (1967). *J. Comp. Phys*, 2:12–26.

Clavin, P., d'Humières, D., Lallemand, P., and Pomeau, Y. (1986). Cellular automata for hydrodynamics with free boundaries in two and three dimensions. *C. R. Acad. Sci. Paris*, 303:1169.

Clavin, P., Lallemand, P., Pomeau, Y., and Searby, G. (1988). Simulation of free boundaries in flow systems by lattice-gas models. *J. Fluid Mech.*, 188:437–464.

Clouqueur, A. and d'Humières, D. (1987). Rap1, a cellular automaton machine for fluid dynamics. *Complex Systems*, 1:584–597.

Cornubert, R. (1991). *Conditions aux limites des modèles cinétiques discrets: couche de Knudsen et obstacles.* PhD thesis, École Normale Supérieure.

Cornubert, R., d'Humiéres, D., and Levermore, D. (1991). A knudsen layer theory for lattice gases. *Physica D*, 47:241.

Coxeter, H. S. M. (1977). *Regular Polytopes.* Dover.

Dab, D., Boon, J., and Li, Y. (1991). Lattice-gas automata for coupled reaction-diffusion equations. *Phys. Rev. Lett.*, 66:2535–2538.

Dab, D., Lawniczak, A., Boon, J., and Kapral, R. (1990). Cellular automaton model for reactive systems. *Phys. Rev. Lett.*, 64:2462–2465.

de Gennes, P. (1983). Theory of slow biphasic flows in porous media. *Physico-Chem. Hydrodyn.*, 4:175.

d'Humières, D. and Cornubert, R. (1993). Flow past a symmetric back-facing step using lattice-Boltzmann equations. preprint.

d'Humières, D. and Lallemand, P. (1986). Lattice gas automata for fluid mechanics. *Physica A*, 140:326–335.

d'Humières, D. and Lallemand, P. (1987). Numerical simulations of hydrodynamics with lattice gas automata in two dimensions. *Complex Systems*, 1:599–632.

d'Humières, D., Lallemand, P., Boon, J. P., Dab, D., and Noullez, A. (1988). Fluid dynamics with lattice gases. In Livi, R., Ruffo, S., Cilberto, S., and Buiatti, M., editors, *Chaos and Complexity*, page 278. World Scientific, Singapore.

d'Humières, D., Lallemand, P., and Frisch, U. (1986). Lattice gas models for 3d hydrodynamics. *Europhys. Lett.*, 2:291.

d'Humières, D., Lallemand, P., and Searby, G. (1987). Numerical experiments on lattice gases: Mixtures and Galilean invariance. *Complex Systems*, 1:633–647.

d'Humières, D., Lallemand, P., and Shimomura, T. (1985a). An experimental study of lattice gas hydrodynamics. Technical Report LA-UR-85-4051, Los Alamos National Laboratory.

d'Humières, D., Pomeau, Y., and Lallemand, P. (1985b). Simulation d'allées de von Karman bidimensionelle à l'aide d'un gas sur réseau. *C. R. Acad. Sc. Paris*, 301:1391–1394.

d'Humieres, D., Qian, Y., and Lallemand, P. (1989). Invariants in lattice gas models. In Monaco, R., editor, *Discrete kinetic theory, lattice gas dynamics, and foundations of hydrodynamics*, Singapore. World Scientific.

d'Humieres, D., Qian, Y., and Lallemand, P. (1990). Finding the linear invariants of lattice gases. In A. Pires, D. P. L. and Herrmann, H., editors, *Computational Physics and Cellular Automata*, pages 97–115, Singapore. World Scientific.

di Pietro, L. (1993). *Transfert d'eau dans des milieux à porosité bimodale: modelisations par la methode de gaz sur reseaux*. PhD thesis, Universite Montpellier II.

di Pietro, L. B., Melayah, A., and Zaleski, S. (1993). Modelling water flow in unsaturated porous media by interacting lattice gas – cellular automata: Infiltration. preprint.

Diemer, K., Hunt, K., Chen, S., Shimomura, T., and Doolen, G. (1990). Density and velocity dependence of reynolds numbers for several lattice gas models. In Doolen, G., Frisch, U., Hasslacher, B., Orszag, S., and Wolfram, S., editors, *Lattice-gas methods for partial differential equations*, pages 137–177. Addison Wesley, New York.

Dorfman, J. R. and Cohen, E. (1970). *Phys. Rev. Lett.*, 25:1257.

Drew, D. A. (1983). Mathematical modeling of two-phase flow. *Ann. Rev. Fluid Mech.*, 15:261.

Dyson, F. (1979). *Disturbing the Universe*. Harper and Row, New York.

Ernst, M. (1991). Mode-coupling theory and tails in CA fluids. *Physica D*, 47:198–211.

Ernst, M. H. and Dufty, J. W. (1990). Hydrodynamics and time correlation functions for cellular automata. *J. Stat. Phys.*, 58:57–86.

Evans, D. J., Hanley, H., and Hess, S. (1984). Non-newtonian phenomena in simple fluids. *Physics Today*, 43:26.

Farmer, D., Toffoli, T., and Wolfram, S., editors (1984). *Cellular Automata*. North Holland Physics Publishing, New York.

Feder, J. (1988). *Fractals*. Plenum Press, New York.

Feynman, R. (1982). Simulating physics with computers. *Int. J. Theor. Phys.*, 21:467–488.

Flekkoy, E. (1993). *Modeling miscible fluids*. PhD thesis, University of Oslo.

Forster, D., Nelson, D., and Stephen, M. (1977). *Phys. Rev. A*, 16:732.

Fratzl, P. and Lebowitz, J. L. (1989). Universality of scaled structure functions in quenched systems undergoing phase separation. *Acta Metall.*, 37:3245–3248.

Frenkel, D. (1990). Fast algorithms for slow processes in lattice-gas cellular automata. *Int. J. Mod. Phys. C*, 2:66–74.

Frenkel, D. and Ernst, M. H. (1989). Simulation of diffusion in a two-dimensional lattice-gas cellular automaton: a test of mode-coupling theory. *Phys. Rev. Lett.*, 63:2165–2168.

Frisch, U., d'Humières, D., Hasslacher, B., Lallemand, P., Pomeau, Y., and Rivet, J.-P. (1987). Lattice gas hydrodynamics in two and three dimensions. *Complex Systems*, 1:648.

Frisch, U., Hasslacher, B., and Pomeau, Y. (1986). Lattice-gas automata for the Navier-Stokes equations. *Phys. Rev. Lett.*, 56:1505–1508.

Furukawa, H. (1985). A dynamic scaling assumption for phase separation. *Adv. Phys.*, 34:703.

Gatignol, R. (1975). *Théorie cinétique des gaz à répartion discrète des vitesses, Le cture Notes in Physics* 36. Springer, Berlin.

Gerits, M., Ernst, M., and Frenkel, D. (1993). Lattice gas automata with attractive and repulsive interactions. preprint.

Grosfils, P., Boon, J.-P., and Lallemand, P. (1992). Spontaneous fluctuation correlations in termal lattice gas automata. *Phys. Rev. Lett.*, 68:1077–1080.

Grunau, D., Chen, S., and Eggert, K. (1993). A lattice-Boltzmann model for multiphase fluid flows. *Phys. Fluids A*, 5:2557–2562.

Gunstensen, A. K. (1992). *Lattice-Boltzmann Studies of Multiphase Flow Through Porous Media*. PhD thesis, Massachusetts Institute of Technology.

Gunstensen, A. K. and Rothman, D. H. (1991a). A Galilean-invariant two-phase lattice gas. *Physica D*, 47:53–63.

Gunstensen, A. K. and Rothman, D. H. (1991b). A lattice-gas model for three immiscible fluids. *Physica D*, 47:47–52.

Gunstensen, A. K. and Rothman, D. H. (1992). Microscopic modeling of immiscible fluids in three dimensions by a lattice-Boltzmann method. *Europhys. Lett.*, 18(2):157–161.

Gunstensen, A. K. and Rothman, D. H. (1993). Lattice-Boltzmann studies of two-phase flow through porous media. *J. Geophys. Res.*, 98:6431–6441.

Gunstensen, A. K., Rothman, D. H., Zaleski, S., and Zanetti, G. (1991). A lattice-Boltzmann model of immiscible fluids. *Phys. Rev. A.*, 43:4320–4327.

Gunton, J., Miguel, M. S., and Sahni, P. (1983). The dynamics of first-order phase transitions. In Domb, C. and Lebowitz, J. L., editors, *Phase transitions and critical phenomena*, volume 8, pages 269–482. Academic Press.

Hansen, J. P. (1976). *Theory of simple liquids*. Academic Press, New York.

Hardy, J., de Passis, O., and Pomeau, Y. (1976). Molecular dynamics of a classical lattice gas: Transport properties and time correlation functions. *Phys. Rev. A.*, 13:1949–1961.

Hardy, J., Pomeau, Y., and de Passis, O. (1973). Time evolution of a two-dimensional model system. I. invariant states and time correlation functions. *J. Math. Phys.*, 14:1746–1759.

Hashimoto, T., Takebe, T., and Suehiro, S. (1988). Ordered structure and critical phenomena of a semidilute solution of polymer mixtures under shear flow. *J. Chem. Phys.*, 88:5874.

Hénon, M. (1987a). Appendix F to "Lattice gas hydrodynamics in two and three dimensions". *Complex Systems*, 1:648–707.

Hénon, M. (1987b). Viscosity of a lattice gas. *Complex Systems*, 1:763–789.

Hénon, M. (1989). Optimization of collision rules in the FCHC lattice gas, and addition of rest particles. In Monaco, R., editor, *Discrete Kinetic Theory, Lattice-Gas Dynamics, and Foundations of Hydrodynamics*, page 146. World Scientific.

Higuera, F. and Jimenez, J. (1989). Boltzmann approach to lattice gas simulations. *Europhysics Letters*, 9:663.

Higuera, F. and Succi, S. (1989). Simulating the flow around a cylinder with a lattice boltzmann equation. *Europhysics Letters*, 8(6):517.

Hohenberg, P. and Halperin, B. (1977). Theory of dynamic critical phenomena. *Rev. Mod. Phys.*, 49:435.

Hopkins, M. A. and Louge, M. Y. (1991). Inelastic microstructure in rapid granular flows of smooth disks. *Phys. Fluids A*, 3:47–57.

Imaeda, T., Onuki, A., and Kawasaki, K. (1984). anisotropic spinodal decomposition under shear flow. *Prog. Theor. Phys.*, 71:16.

Kadanoff, L. (1986). On two levels. *Physics Today*, 39:7–9.

Kadanoff, L., McNamara, G., and Zanetti, G. (1989). From automata to fluid flow: comparisons of simulation and theory. *Phys. Rev. A*, 40:4527–4541.

Kadanoff, L. and Swift, J. (1968). Transport coefficients near the critical point: a master equation approach. *Phys. Rev.*, 165:310–322.

Kalaydjian, F. (1990). Origin and quantification of coupling between relative permeabilities for two-phase flows in porous media. *Transport in Porous Media*, 5:215–229.

Kapral, R., Lawniczak, A., and Masiar, P. (1991). Oscillations and waves in a reactive lattice-gas automaton. *Phys. Rev. Lett.*, 66:2539–2542.

Kirkpatrick, T. R. and Ernst, M. H. (1991). Kinetic theory for lattice gas cellular automata. *Phys. Rev. A*, 44:8051.

Kohring, G. (1991a). Calculation of the permeability of porous media using hydrodynamic cellular automata. *J. Stat. Phys.*, 63:411–418.

Kohring, G. (1991b). Effect of finite grain size on the simulation of fluid flow in porous media. *J. Phys. II*, 1:87–90.

Kohring, G. (1991c). Limitations of a finite mean free path for simulating flows in porous media. *J. Phys. II*, 1:593–597.

Kong, X. P. and Cohen, E. G. D. (1991). A kinetic theorist's look at lattice gas cellular automata. *Physica D*, 47:9–18.

Krall, A. H., Sengers, J. V., and Hamano, K. (1989). Viscosity of a phase-separating critical mixture. *Intl. J. Thermophys.*, 10:309.

Krall, A. H., Sengers, J. V., and Hamano, K. (1992). Viscoelasticity of a simple liquid mixture during spinodal decomposition. *Phys. Rev. Lett.*, 69:1963–1966.

Ladd, A. J. C. and Colvin, M. E. (1988). Application of lattice-gas cellular automata to Brownian motion of solids in suspension. *Phys. Rev. Lett.*, 60:975–978.

Ladd, A. J. C. and Frenkel, D. (1990). Dissipative hydrodynamic interactions via lattice-gas cellular automata. *Phys. Fluids A*, 2:1921–1924.

Lafaurie, B., Nardone, C., Scardovelli, R., Zaleski, S., and Zanetti, G. (1993). Modelling merging and fragmentation in multiphase flows with SURFER. preprint.

Landau, L. D. and Lifshitz, E. M. (1959a). *Fluid Mechanics*. Pergamon Press, New York.

Landau, L. D. and Lifshitz, E. M. (1959b). *Theory of Elasticity*. Pergamon Press, New York.

Landau, L. D. and Lifshitz, E. M. (1986). *Statistical Physics (Part 1)*. Pergamon Press, New York.

Lawniczak, A., Dab, D., Kapral, R., and Boon, J. P. (1991). Reactive lattice-gas automata. *Physica D*, 47:132–158.

Lebowitz, J. L., Marro, J., and Kalos, M. H. (1982). Dynamical scaling of sturcture function in quenched binary alloys. *Acta Metall.*, 30:297–310.

Lebowitz, J. L., Orlandi, E., and Presutti, E. (1991). A particle model for spinodal decomposition. *J. Stat. Phys.*, 63:933–974.

Lees, A. and Edwards, S. (1972). The computer study of transport processes under extreme conditions. *J. Phys. C: Solid State Physics*, 5:1921–1929.

Loose, W. and Hess, S. (1989). Rheology of dense model fluids via nonequilibrium molecular dynamics: shear thinning and ordering transition. *Rheologica Acta*, 28:91–101.

Ma, S.-K. (1985). *Statistical Mechanics*. World Scientific, Singapore.

Manneville, P. (1990). *Dissipative structures and weak turbulence*. Academic Press, Boston.

Mareschal, M. and Kestemont, E. (1987). Order and fluctuations in nonequilibrium molecular dynamics simulations of two-dimensional fluids. *J. Stat. Phys.*, 48:1187.

Margolus, N. (1984). Physics-like models of computation. *Physica*, D 10:81–95.

Marro, J., Lebowitz, J. L., and Kalos, M. H. (1979). Computer simulation of the time evolution of a quenched model alloy in the nucleation region. *Phys. Rev. Lett.*, 43:282–284.

Massaioli, F., Succi, S., and Benzi, R. (1993). *Europhys. Lett.*, 21:305.

McNamara, G. and Zanetti, G. (1988). Use of the Boltzmann equation to simulate lattice-gas automata. *Phys. Rev. Lett.*, 61:2332.

McNamara, G. R. (1990). Diffusion in a lattice gas automaton. *Europhys. Lett.*, 12:329.

Molvig, K., Donis, P., and Teixeira, C. (1992). Lattice-gas aerodynamics. preprint.

Naitoh, T. and Ernst, M. H. (1991). Full time-dependence of the VACF in CA-fluids: Theory and simulations. In Alves, A. S., editor, *Proceedings of Euromech Colloquium 267, Series on Advanced Mathematics for Applied Sciences*, pages 166–175, Singapore. World Scientific.

Naitoh, T., Ernst, M. H., and Dufty, J. W. (1990). Long time tails in two-dimensional cellular-automata fluids. *Phys. Rev. A*, 42:7187–7194.

Naitoh, T., Ernst, M. H., Van der Hoef, M. A., and Frenkel, D. (1991). Extended mode coupling and simulations in cellular-automata fluids. *Phys. Rev. A*, 44:2484–2494.

Noulles, A. and Boon, J.-P. (1991). Long-time correlations in a 2d lattice gas. *Physica D*, 47:212–215.

Nozières, P. and Quemada, D. (1986). A possible instability mechanism for plug formation in a sheared suspension flow. *Europhys. Lett.*, 2:129–135.

Ohta, T., Nozaki, H., and Doi, M. (1990). Computer simulations of domain growth under steady shear flow. *J. Chem. Phys.*, 93:2664–2675.

Olson, J. F. and Rothman, D. H. (1993). Effective viscosity of 3d lattice-gas emulsions. unpublished.

Onuki, A. (1987). Viscosity ehnancement by domains in phsae-separating fluids near the critical point: proposal of critical rheology. *Phys. Rev. A*, 35:5149–5155.

Orszag, S. and Yakhot, V. (1986). Reynolds number scaling of cellular-automaton hydrodynamics. *Phys. Rev. Lett.*, 56:1691–1693.

Paul, B., d'Humières, D., and Rothman, D. (1993). Exact solutions for the relaxation lattice-Boltzmann model of immiscible fluids. preprint.

Peyret, R. and Taylor, T. D. (1983). *Computational Methods for Fluid Flow*. Springer-Verlag.

Pomeau, Y. (1986). *Physica D*, 23:3.

Pomeau, Y. and Résibois, P. (1975). Time dependent correlation functions and mode-mode coupling theories. *Phys. Rep.*, 19:63–139.

Pot, V., Appert, C., Melayah, A., Rothman, D. H., and Zaleski, S. (1993). Modelling water flow in unsaturated porous media by interacting lattice gas – cellular automata: Evaporation. preprint.

Qian, Y. (1990). *Gaz sur Réseaux et Théorie Cinétique sur les Réseaux Appliquée à l'Équation de Navier-Stokes*. PhD thesis, École Normale Supérieur.

Qian, Y., d'Humières, D., and Lallemand, P. (1990). A one-dimensional lattice-Boltzmann equation with Galilean invariance. In Gatignol, R. and Soubbaramayer, editors, *Advances in Kinetic Theory and Continuum Mechanics*, pages 127–138. Springer, Berlin.

Qian, Y., D'Humières, D., and Lallemand, P. (1992a). Diffusion simulation with a deterministic one-dimensional model. *J. Stat. Phys.*, 68:563–573.

Qian, Y., D'Humières, D., and Lallemand, P. (1992b). Lattice BGK models for Navier-Stokes equation. *Europhys. Lett.*, 17(6):479–484.

Rapaport, D. and Clementi, E. (1986). Eddy formation in obstructed fluid flow: a molecular dynamics study. *Phys. Rev. Lett.*, 57:69.

Rem, P. and Somers, J. (1989). Cellular automata on a transputer network. In Monaco, R., editor, *Discrete Kinetic Theory, Lattice-Gas Dynamics, and Foundations of Hydrodynamics*, pages 268–275. World Scientific.

Richter, F. and McKensie, D. (1984). Dynamical models for melt segregation from a deformable matrix. *J. Geol.*, 92:729–740.

Rivet, J. P. (1987). Green-Kubo formalism for lattice gas hydrodynmics and Monte-Carlo evaluation of shear viscosities. *Complex Systems*, 1:838–851.

Rivet, J.-P. (1991). Brisure spontanée de symétrie dans le sillage tri-dimensionnel d'un cylindre allongé, simulé par la méthode des gas sur réseaux. *C. R. Acad. Sci. Paris*, 313:151–157.

Rivet, J.-P., Hénon, M., Frisch, U., and d'Humières, D. (1988). Simulating fully three-dimensional external flow by lattice gas methods. *Europhys. Lett.*, 7(3):231.

Rocard, Y. (1967). *Thermodynamique, 2ème édition*. Masson, Paris.

Rothman, D. H. (1988). Cellular-automaton fluids: A model for flow in porous media. *Geophysics*, 53:509–518.

Rothman, D. H. (1990a). Deformation, growth and order in sheared spinodal decomposition. *Phys. Rev. Lett.*, 65:3305.

Rothman, D. H. (1990b). Macroscopic laws for immiscible two-phase flow in porous media: Results from numerical experiments. *J. Geophys. Res.*, 95:8663.

Rothman, D. H. (1991). Complex rheology in a phase-separating fluid. *Europhys. Lett.*, 14:337–342.

Rothman, D. H. (1992). Simple models of complex fluids. In Mareschal, M. and Holian, B., editors, *Microscopic simulations of complex hydrodynamics*. Plenum Press.

Rothman, D. H. and Kadanoff, L. P. (1993). Bubble, bubble, boil and trouble. *Computers in Physics*. in press (November-December).

Rothman, D. H. and Keller, J. (1988). Immiscible cellular-automaton fluids. *J. Stat. Phys.*, 52:1119.

Rothman, D. H. and Zaleski, S. (1989). Spinodal decomposition in a lattice-gas automaton. *J. Phys. France*, 50:2161–2174.

Rowlinson, J. and Widom, B. (1982). *Molecular Theory of Capillarity*. Clarendon Press, Oxford.

Schlichting, H. (1979). *Boundary Layer Theory*, chapter 9. McGraw Hill, New York.

Sheidegger, A. (1960). *The Physics of Flow Through Porous Media*. Macmillan Company, New York.

Somers, J. and Rem, P. (1992). Obtaining numerical results from the 3D FCHC-lattice gas. In *Springer Proceedings on Physics, Workshop on Numerical Methods for the Simulation of Multi-Phase and Complex Flow*, pages 59–78. Springer-Verlag.

Somers, J. A. and Rem, P. C. (1991). Analysis of surface tension in two-phase lattice gases. *Physica D*, 47:39–46.

Stanley, H. E. (1971). *Introduction to Phase Transitions and Critical Phenomena*. Dover Publications, New York.

Stockman, H. W., Stockman, C. T., and Carrigan, C. R. (1990). Modeling viscous segregation in immiscible fluids using lattice-gas automata. *Nature*, 34:523.

Succi, S., Foti, E., and Higuera, F. (1989). Three-dimensional flows in complex geometries with the lattice Boltzmann method. *Europhysics Letters*, 10(5):433–438.

Taylor, W. and Boghosian, B. M. (1992). Renormalization of lattice gas transport coefficients. preprint.

Teixeira, C. M. (1992). *Coninuum limit of lattice-gas fluid dynamics*. PhD thesis, Massachusetts Institute of Technology.

Temam, R. (1969). *Archiv. Ration. Mech. Anal.*, 32:135–153.

Toffoli, T. (1984). Cellular automata as an alternative to (rather than an approximation of) partial differential equations in modeling physics. *Physica*, D 10:117–127.

Toffoli, T. and Margolus, N. (1987). *Cellular automata machines*. MIT Press, Oxford.

Toffoli, T. and Margolus, N. (1991). Programmable matter: Concepts and realization. *Physica D*, 47:263–272.

Tritton, D. J. (1988). *Physical Fluid Dynamics, 2nd edition*. Clarendon Press, Oxford.

Van der Hoef, M. and Frenkel, D. (1990). Long-time tails of the velocity autocorrelation function in 2d and 3d lattice-gas cellular automata: a test of mode-coupling theory. *Phys. Rev. A*, 41:4277.

Van der Hoef, M. A., Dijkstra, M., and Frenkel, D. (1992). Velocity autocorrelation function in a four-dimensional lattice gas. *Europhys. Lett.*, 17:39–43.

Van der Hoef, M. A. and Frenkel, D. (1991). Evidence for faster-than-t^{-1} decay of the velocity autocorrelation function in a 2-D fluid. *Phys. Rev. Lett.*, 66:1591–1594.

Van der Hoef, M. A. and Frenkel, D. (1991). Tagged particle diffusion in 3D lattice gas cellular automata. *Physica D*, 47:191–197.

Vichniac, G. (1984). Simulating physics with cellular automata. *Physica*, D 10:96–116.

von Neumann, J. (1966). *Theory of self-reproducing automata (edited and completed by A. Burks)*. University of Illinois Press.

Weiland, R. H., Fessas, Y. P., and Ramarao, B. V. (1984). On instabilities arising during sedimentation of two-component mixtures of solids. *J. Fluid Mech.*, 142:383.

Weisbuch, G. (1991). *Complex Systems Dynamics*. Addison-Wesley, New York.

Whitham, G. B. (1974). *Linear and nonlinear waves*. Wiley, New York.

Whitmore, R. L. (1955). The sedimentation of suspensions of spheres. *Brit. J. Appl. Phys.*, 6:239–245.

Wolfram, S. (1983). Statistical mechanics of cellular automata. *Rev. Mod. Phys.*, 55:601–644.

Wolfram, S. (1986a). Cellular automaton fluids 1: Basic theory. *J. Stat. Phys.*, 45:471.

Wolfram, S., editor (1986b). *Theory and Applications of Cellular Automata*. World Scientific, Singapore.

Zaleski, S. (1989). Weakly compressible fluid simulations at high reynolds numbers. In Monaco, R., editor, *Discrete Kinetic Theory, Lattice-Gas Dynamics, and Foundations of Hydrodynamics*, pages 384–394. World Scientific.

Zanetti, G. (1989). The hydrodynamics of lattice gas automata. *Phys. Rev. A*, 40:1539.

Zanetti, G. (1991). Counting hydrodynamic modes in lattice gas automata models. *Physica D*, 47:30–35.

Zuse, K. (1970). Calculating space. Technical Report Tech. Transl. AZT-70-164-GEMIT, MIT Project MAC.

FIG. 1. An example of one time step in the evolution of the FHP lattice gas. Each arrow represents a particle of unit mass moving in the direction given by the arrow. Figure 1a is the initial condition. Figure 1b represents the propagation, or free-streaming step: each particle has moved one lattice unit in the direction of its velocity. Figure 1c shows the result of collisions. The only collisions that have changed the configuration of particles are located in the middle row.

FIG. 2. Explicit examples of some collisions that may occur in the FHP model. The two-body head-on collision may result in either a clockwise or counter-clockwise rotation; here we show just one example. The two-body collision shown with non-zero net momentum results in no change, since no other configuration exists that conserves both the number of particles and the net momentum.

FIG. 3. Two dimensional flow past a flat plate, simulated using the FHP lattice gas (d'Humières et al., 1985b). The Reynolds number is approximately 70.

FIG. 4. Lattice-gas simulation of flow through a two-dimensional porous medium (Rothman, 1988). The fluid is forced from left to right.

FIG. 5. Microdynamics of the immiscible lattice gas, in which the initial condition (a), the propagation step (b), and collision step (c) are displayed as in Figure 1. The initial condition and propagation step are the same as before, except that now some particles are red (bold arrows) while others are blue (double arrows). In the collision step, the particles are re-arranged so that, as much as possible, the flux of color is in the direction of the local gradient of color. Compare the middle row here with Figure 1 to see how ILG collisions can create a "colorblind" microdynamics different from that created by FHP collisions.

FIG. 6. Phase separation in the immiscible lattice gas. The initial condition was a homogeneous random mixture, with 50% red (black) particles, and 50% blue (grey). Time t is given in time steps. Boundaries are periodic in both directions. From Rothman (Rothman, 1992).

FIG. 7. Microdynamics of the liquid-gas model, in which the initial condition (a), the propagation step (b), and collision step (c) are precisely the same as that showed in Figure 1. The new, interaction, step is shown in (d). In this example, the interaction distance $r = 2$.

FIG. 8. The interacting collision in the simplest liquid-gas model. Smooth arrows represent particles while broken arrows represent the absence of a particle. The sites on which the interaction occurs are situated r lattice units apart.

FIG. 9. Phase separation with particle removal in the 2D liquid gas model (Appert and Zaleski, 1993). The pixels are black for more than 2 particles per site and white otherwise. Thus the liquid phase is mostly black while the gas phase is mostly white. The lattice is initialised with a uniform particle distribution. As time progresses particles are slowly removed at random. After an initial transient, the density of the liquid and the gas remain constant, but the fraction of space covered by the dense phase is decreasing. This leads to the formation of a 2D soap froth.

FIG. 10. A table of configurations for the six-velocity FHP lattice gas. Each entry corresponds to a given class (n, g_x^*, g_y^*). Other configurations in the same class may sometimes be obtained by rotation. The number of configurations in the class is then shown in parentheses. Configurations for other values of (g_x^*, g_y^*) may be obtained by reflections. Configurations for $n > 3$ are all obtained by exchanging particles with holes.

FIG. 11. A table of configurations for the seven-velocity FHP lattice gas, constructed using the same scheme as in Figure 10. Notice that for $(n, g_x^*, g_y^*) = (3, 0, 0)$ there are two subclasses A and B. In each subclass the configurations may be deduced from each other by rotations and reflections.

FIG. 12. The face-centered cubic lattice. The filled circles belong to the face-centered lattice and correspond to coordinates (a, b, c) of even sum. The unfilled circles have integer coordinates with odd sum. This lattice is the analog in three dimensions of the FCHC lattice. A 2D layer of the lattice contains points of coordinates $c = 0$ or 1. Similarly a 3D layer of the FCHC lattice spans two values of the coordinate in the fourth dimension.

FIG. 13. A perspective view of the FCHC primitive cell, projected into 3D space. Instead of explicitly showing all 24 velocities, only 2 of the 12 velocities which extend into the fourth dimension are shown, along with just one of the velocities with no component in the fourth dimension.

FIG. 14. A projection of the polytope of Schläfi symbol $\{3, 4, 3\}$ (Coxeter, 1977). Vertices are shown as small circles. As indicated by the Schläfi symbol each face has 3 edges. The 8 edges atttached to each vertex join it to a cube. This cube is the Et P polytope connected to each vertex and its Schläfi symbol $\{4, 3\}$. A definition of Et P and the Schläfi symbol may be found in Appendix A.

FIG. 15. A more complex interacting model. The five interactions are performed in a sequence for a given pair of sites. The diagrams represent the particles before and after the collision as in Figure 8. A thin line is added between the two sites to guide the eye.

FIG. 16. Control volume $ABCD$ (bold curves) around an interface (thin curve). The capillary forces, $\mathbf{f}_c$, act on the control volume.

FIG. 17. Estimates of apparent viscosity as a function of velocity for the liquid phase of the liquid-gas model (di Pietro, 1993). The viscosities were obtained from simulations of Poiseuille flow in a 2D rectangular channel for various velocities and channel widths. The various symbols correspond to different channel widths, and the dotted curve corresponds to the best-fitting quadratic function of velocity.

FIG. 18. Measurements of equilibrium pressures on each side of a curved interface for the liquid-gas model on the FCHC lattice (Appert et al., 1993c). Pressures are plotted as a function of the curvature $1/R$. The descending curves are the equilibrium liquid and gas pressures, stars are gas pressures, diamonds are liquid pressures, and the straight lines correspond to equation (VI.63) in text. The ascending curve and the triangles are the difference between the liquid and gas pressures.

FIG. 19. a) The 0-degree interface. b) The 30-degree interface. The directions $\mathbf{c}_1, \ldots, \mathbf{c}_8$ are labeled explicitly in the former case. Note that the 0-degree interface may be described by two layers whereas that the 30-degree interface requires four layers.

FIG. 20. Surface tension as a function of reduced density d in the immiscible lattice gas (Adler et al., 1994). Smooth curve: Boltzmann approximation for a two-layer 0-degree interface. Dotted curve: Boltzmann approximation for a four-layer 30-degree interface. Circles: empirical results from fitting Laplace's formula to measurements made from bubbles of different sizes. Squares: measurements made from flat, 0-degree, interfaces. Triangle: measurements made from flat, 30-degree, interfaces. Error bars are smaller than the size of the symbols.

FIG. 21. Verification of Laplace's law in the immiscible lattice gas (Adler et al., 1994). Bubble radii R range from 4 to 64 lattice units. An estimate of surface tension is given by the slope of the best fitting line that passes through the origin. Error bars are smaller than the size of the symbols.

FIG. 22. Setup for interface calculations in the liquid gas model on the FCHC lattice. Momentum transfer across the surface Σ is calculated.

FIG. 23. Density profile (dashed line) obtained from the resolution of equation (VII.34), and from direct numerical simulation.

FIG. 24. Comparison of interface fluctuations ($\langle |A_q|^2 \rangle$) obtained from simulations (circles) and those predicted from classical theory (straight line, given by equation (VII.38)) (Adler et al., 1994).

FIG. 25. Pressure measurements for the liquid-gas model on the FCHC lattice. Symbols represent estimates from numerical simulations: stars are simulations of the non-interacting, ideal gas, diamonds are the liquid-gas model for $r = 3$, and triangles and squares are the liquid-gas model for $r = 8$. Triangles refer to early measurements, whereas squares have been plotted after equilibrium has been reached (except in the metastable region). Solid lines correspond to equation (VIII.1) in text. Pressures are divided by $c^2 = 2$.

FIG. 26. Typical free-energy curves in a binary fluid mixture, for temperatures $T_1 < T_2 < T_3$, where $T_2 \approx T_c$.

FIG. 27. Plot of Boltzmann approximation for $D(d, \theta) = 0$ (smooth curve) vs. empirical estimates of the point of marginal stability (circles) for ILG mixtures, in the plane of concentration θ and reduced density d (Rothman and Zaleski, 1989). Errors in the empirical estimates are approximately the same size as the symbols. The curves represent theoretical and empirical phase diagrams, respectively, for the ILG.

FIG. 28. (a) Contours of $\log_{10} S(\mathbf{k})$ at $t = 1000$ time steps after quenching, in intervals of $10^{1/2}$. The highest contour level (near center) is bold. (b) $\hat{S}(k)$ for $t = 100, 200, \ldots, 1000$, where the maximum of each curve grows with time. (c) Scaled structure functions $A^{-1}k_m^2\hat{S}(k)$ for $t = 100, 200, \ldots, 1000$. Wavenumber axes in (a) and (b) represent cycles per lattice unit. From Rothman (Rothman, 1990a).

FIG. 29. Design of numerical experiment for sheared phase separation. Boundaries are periodic in both directions.

FIG. 30. Phase separation patterns at two different times after quenching (Rothman, 1990a). (a) No shear. (b) Shear rate $C = C_0$. (c) Shear rate $C = 1.5C_0$. Time t is in time steps; Ct is shear strain.

FIG. 31. Contours of $\log_{10} S(\mathbf{k})$ computed by averaging spectra from 40 independent simulations of sheared phase separation (Rothman, 1990a). The contour interval is $10^{1/2}$; the lowest level in each plot is the same and the highest contour in each plot is bold. Times t and shear rates C in (a)–(c) correspond to those of the real-space patterns depicted at the later time in (a)–(c), respectively, of Figure 30.

FIG. 32. Three dimensional lattice-Boltzmann simulation of multiphase flow through porous media (Gunstensen and Rothman, 1993). (See Appendix C for a discussion of the relation of the lattice-Boltzmann method to the lattice-gas method.) The porous medium is modeled by the random placement of overlapping (yellow) spheres of constant radius. The medium is initially filled with a transparent wetting fluid. The non-wetting fluid, shown in blue, is injected into the porous medium from behind, forcing the transparent clear fluid to evacuate the medium. The lattice size is 32^3.

FIG. 33. An equilibrium configuration in the many bubble model (Rothman and Kadanoff, 1993). The lattice is 128×128, each bubble has a radius of about 5 lattice units, and the concentration of bubbles is 0.40. The random placement of each bubble resulted from collective Brownian motion.

FIG. 34. A simulation of two-component sedimentation, using the many-bubble model (Rothman and Kadanoff, 1993). The lattice contains 512×512 points; positively buoyant bubbles are red and negatively buoyant bubbles are blue; there are 1024 bubbles, each with a radius of about 5 lattice units, encompassing a total volume fraction of 0.4. The figure shown is 8500 time steps after initialisation of the gravitational acceleration, at which time the distribution of red and blue bubbles was random. The recent motion of the individual bubbles prior to each snapshot is indicated by a reverse fade-out: the more distant in time prior to the present configuration, the more pale is the shade of red or blue. If bubble trajectories cross, the more recent trajectory takes precedence. Note the appearance of large-scale finger-like or column-like structures. while other structures look more like the heads of plumes.

FIG. 35. Phase separation in a 3D implementation of the liquid-gas model.

FIG. 36. Simulation of sheared phase separation, using a 3D immiscible lattice gas model (Olson and Rothman, 1993). The shear strains Ct correspond to time steps 800, 4160, and 4240 after quenching from an initial condition of a homogeneous mixture with 10% concentration of the minority phase; the height of the lattice is 64, the width is 32, and the depth is 16. The flow is downward on the left and upward on the right; boundary conditions in the shear direction are periodic with vertical displacement due to the shear (Lees and Edwards, 1972) and simply periodic in the other two directions. The two later snapshots are from the steady state in which a characteristic bubble size has evolved due to the competition between shear and surface tension. Note the bubble at the bottom center for $Ct = 26$ has broken into two bubbles by $Ct = 26.5$.

FIG. 37. An example of the construction of Et(P). The cube (symbol $\{4,3\}$) is shown. All the vertices attached to vertex A form the triangle Et P (A) shown in the figure. The cube has 4-edged faces and thus has symbol $\{4,3\}$.

FIG. 38. A construction used in the proof of Lemma 1.

FIG. 39. Another construction used in the proof of Lemma 1.

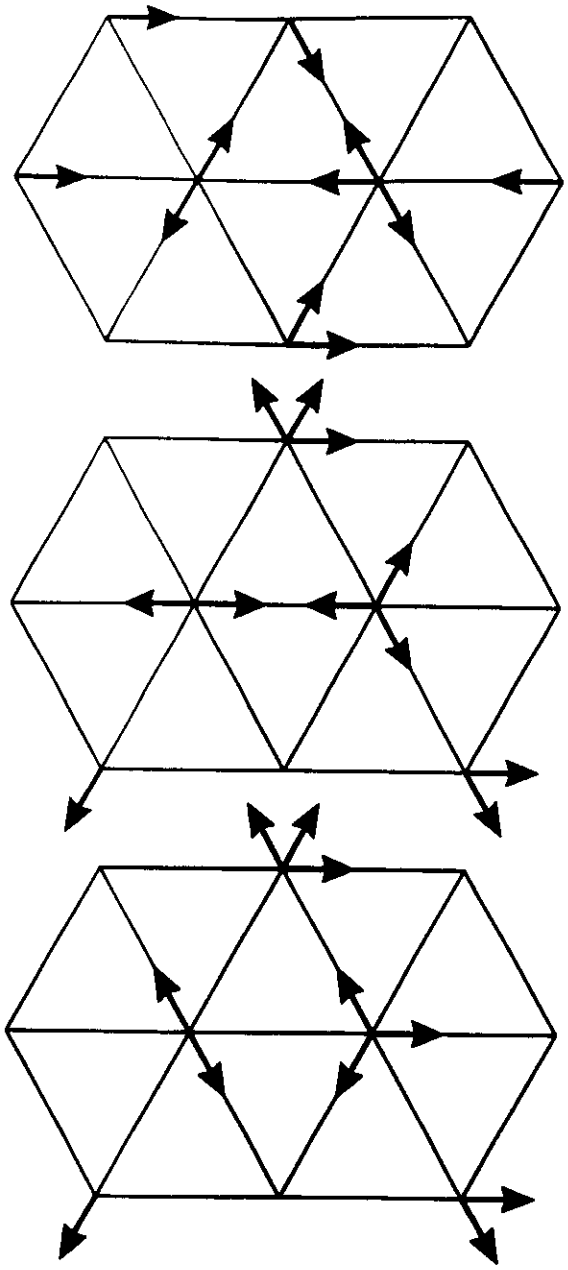

Fig 1

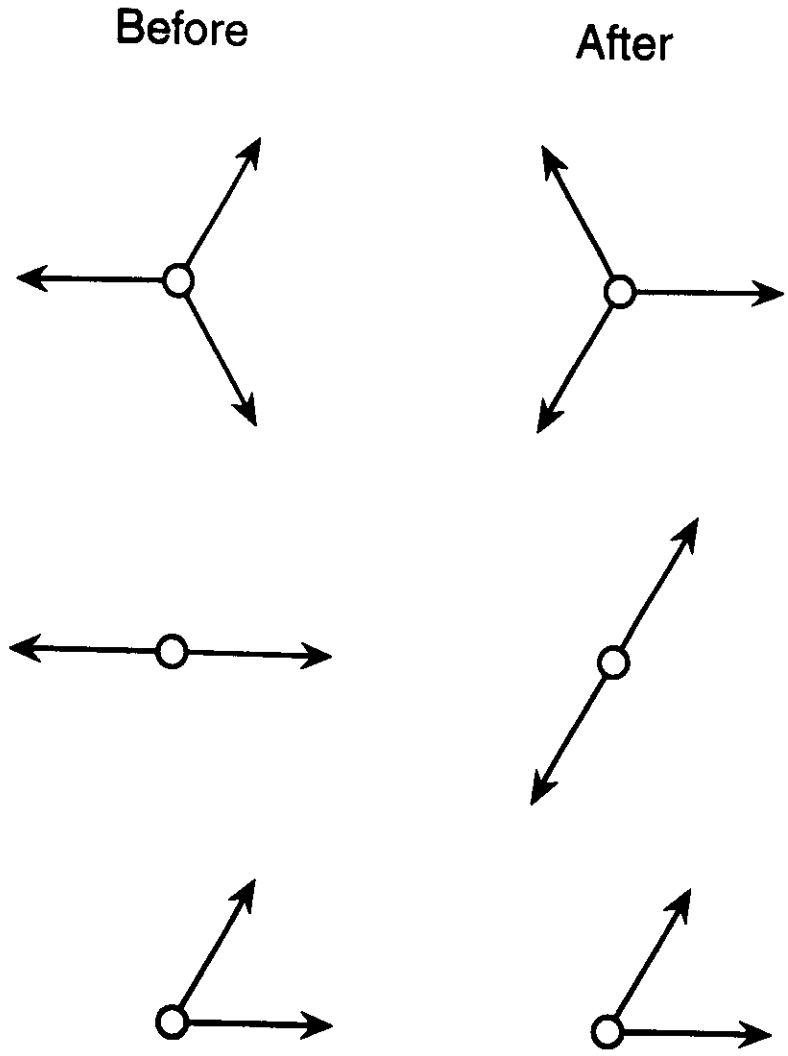

Fig 2

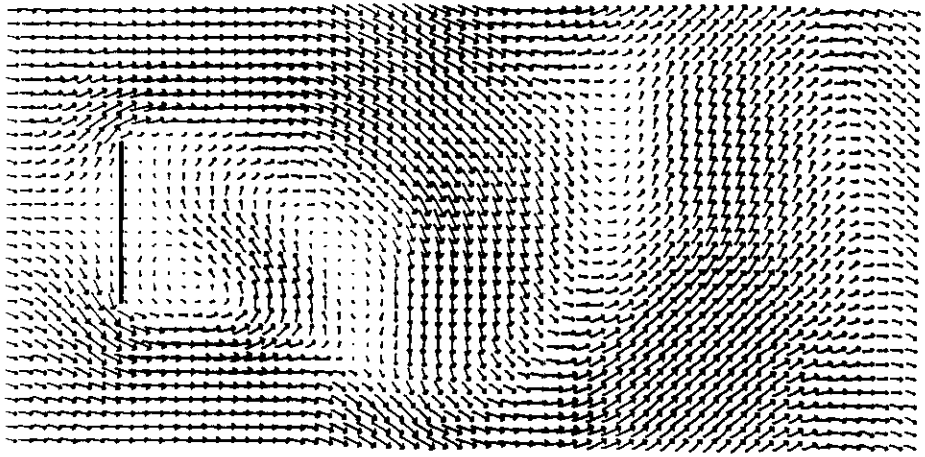

Fig 3

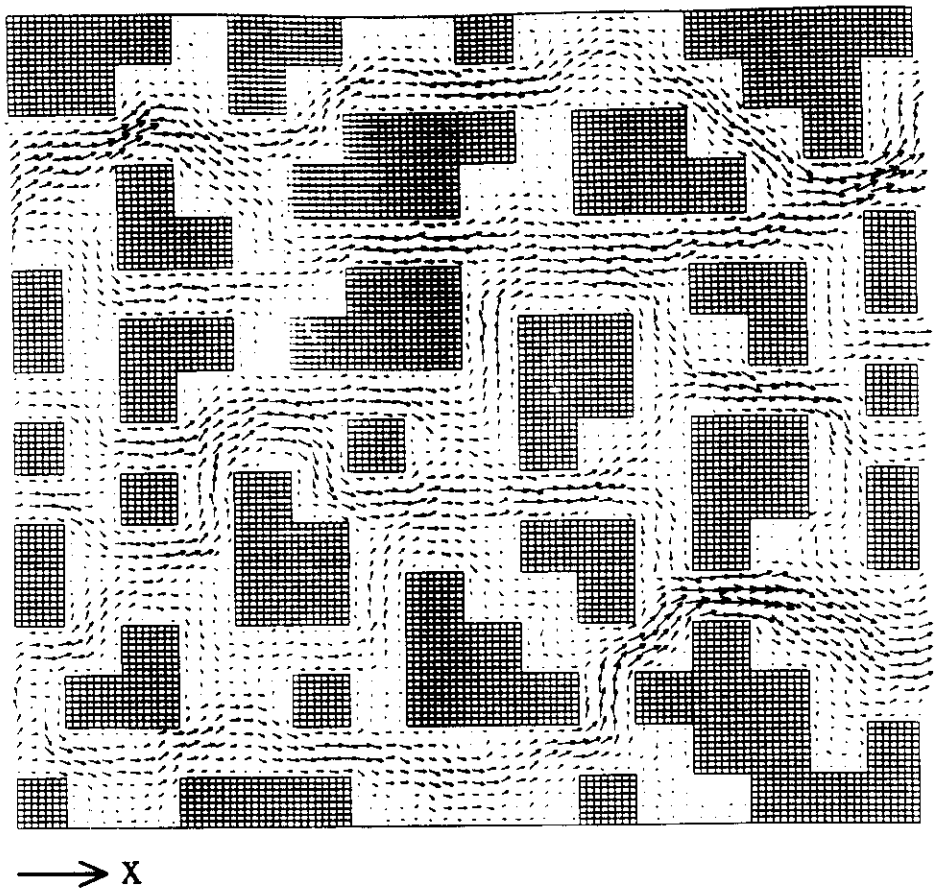

Fig 4

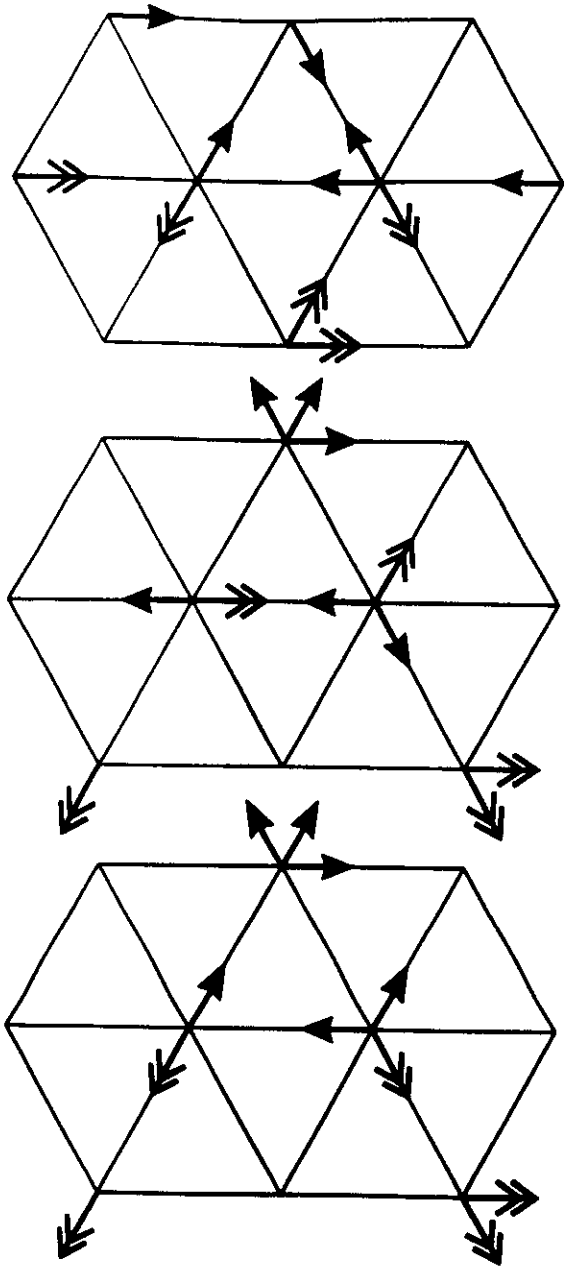

Fig 5

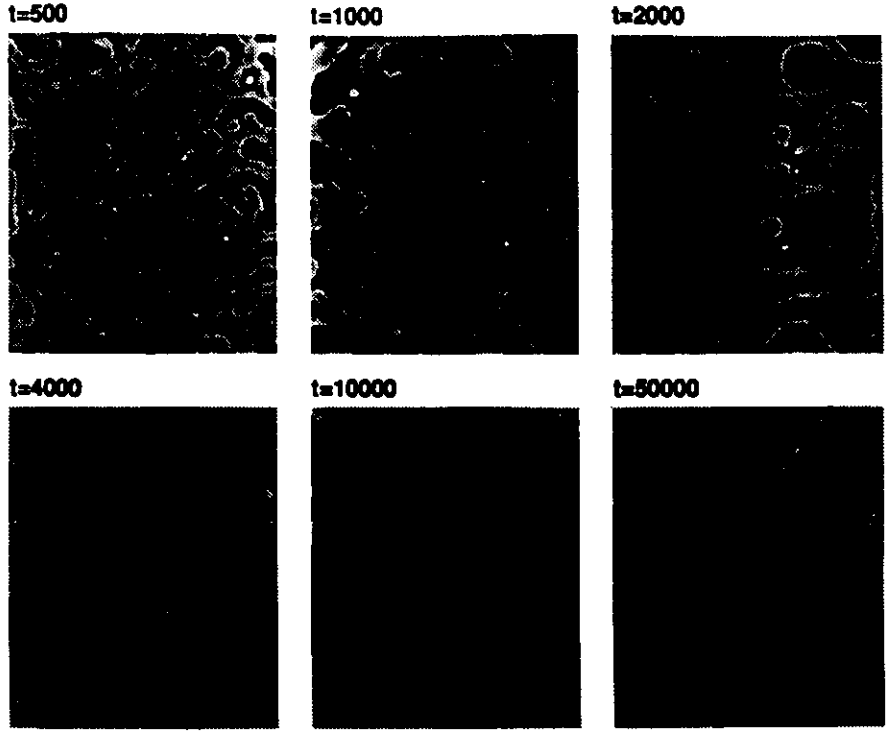

Fig 6

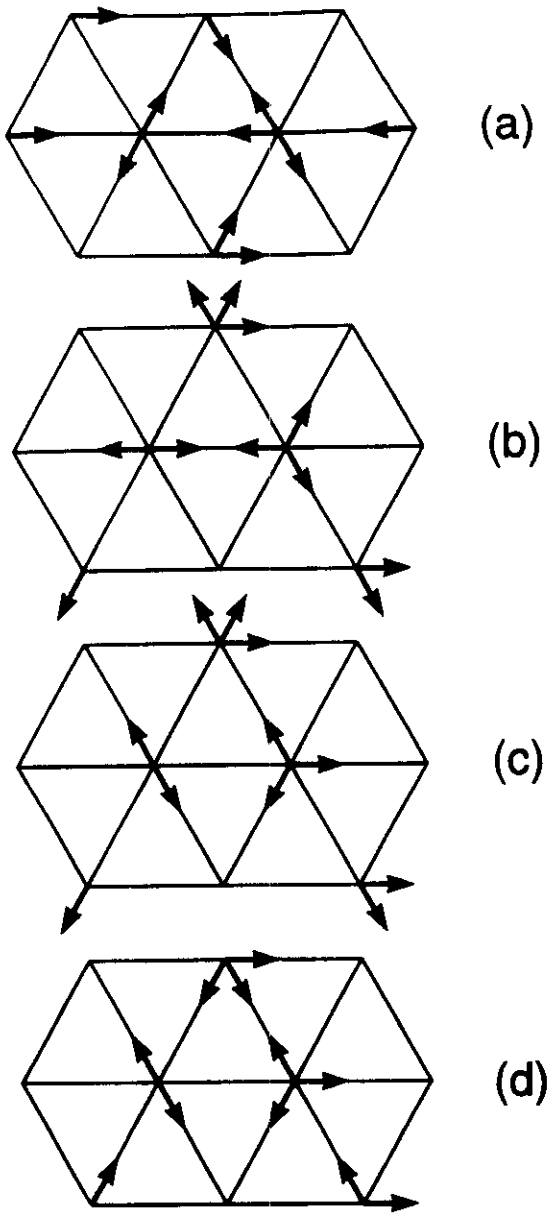

Fig 7

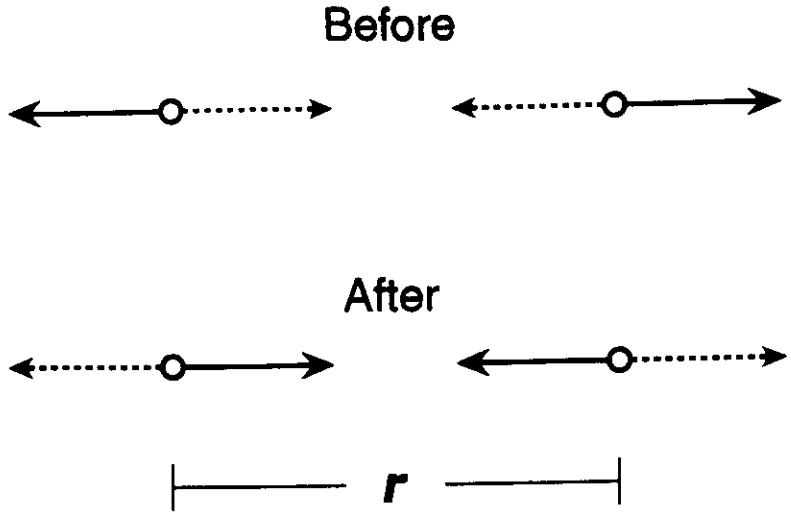

Fig 8

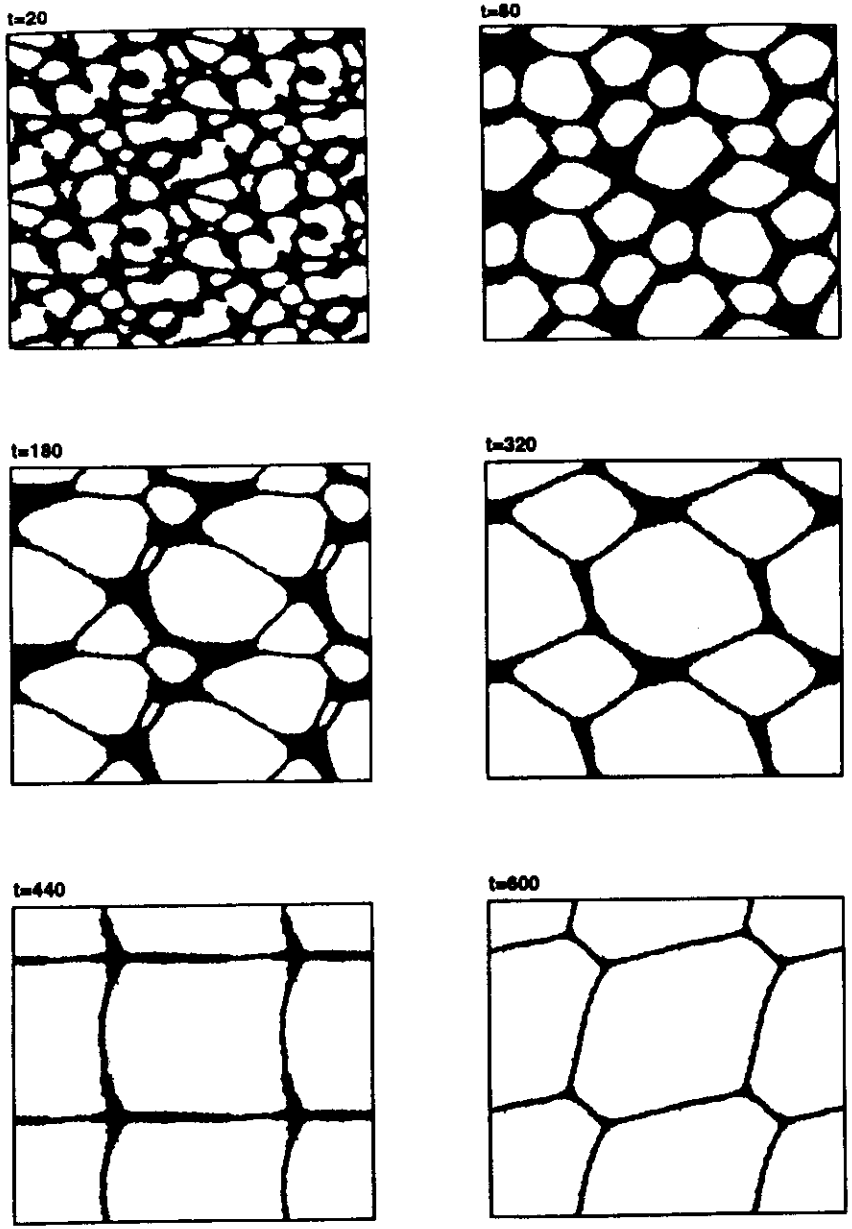

Fig 9

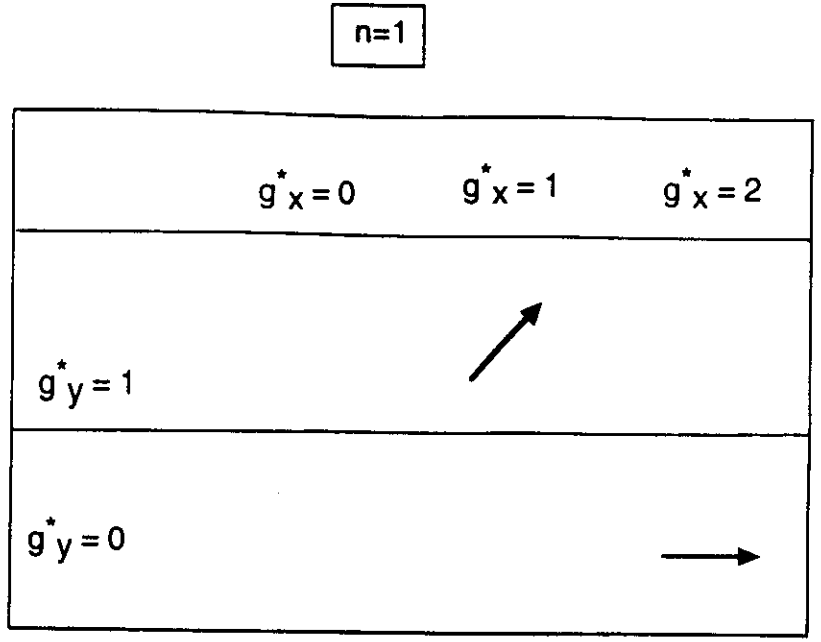

Fig 10
Part 1

n=2

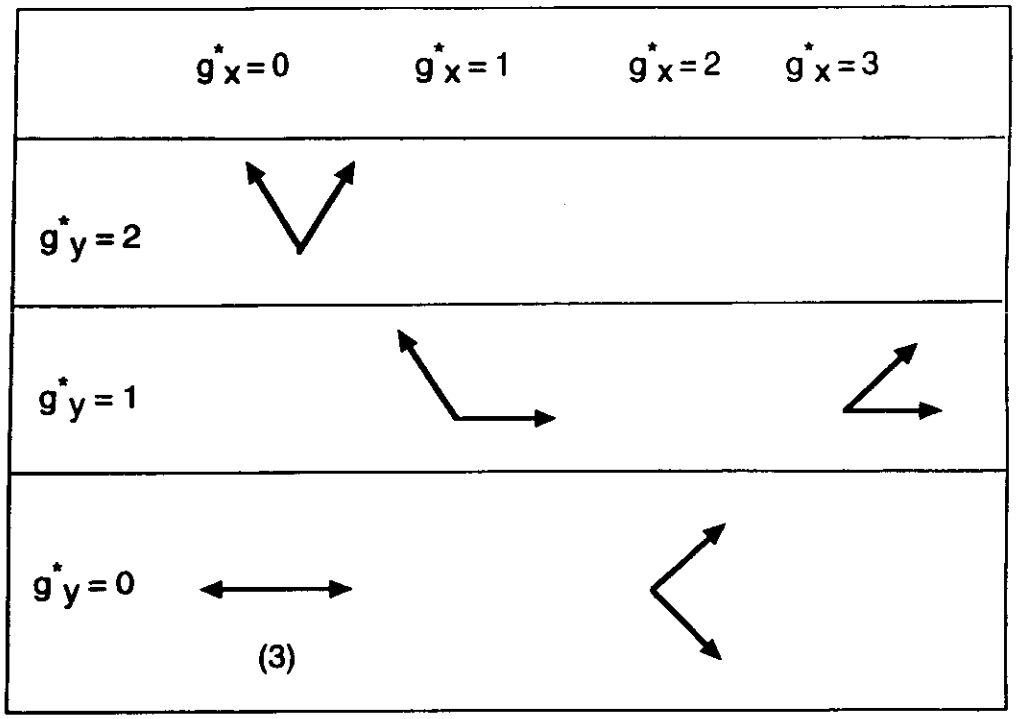

Fig 10 Part 2

n=3

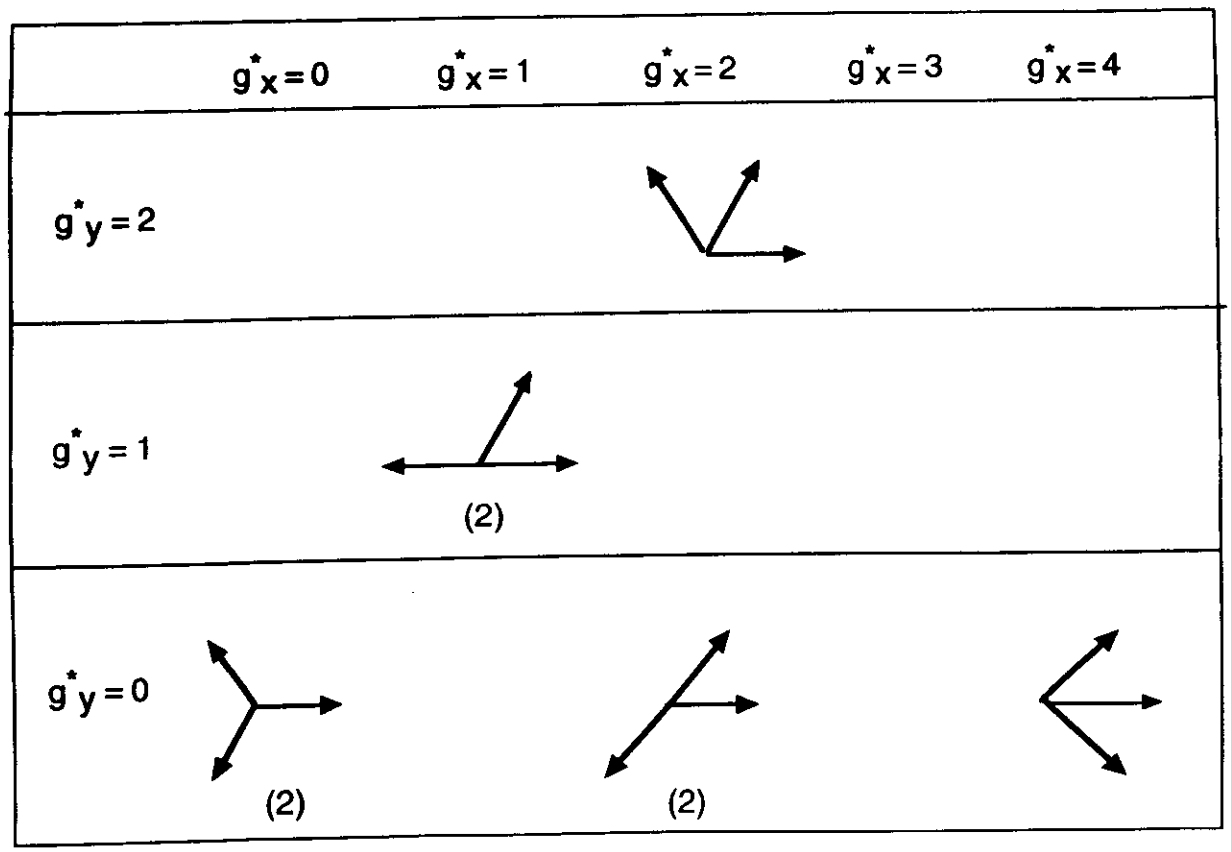

Fig 10 Part 3

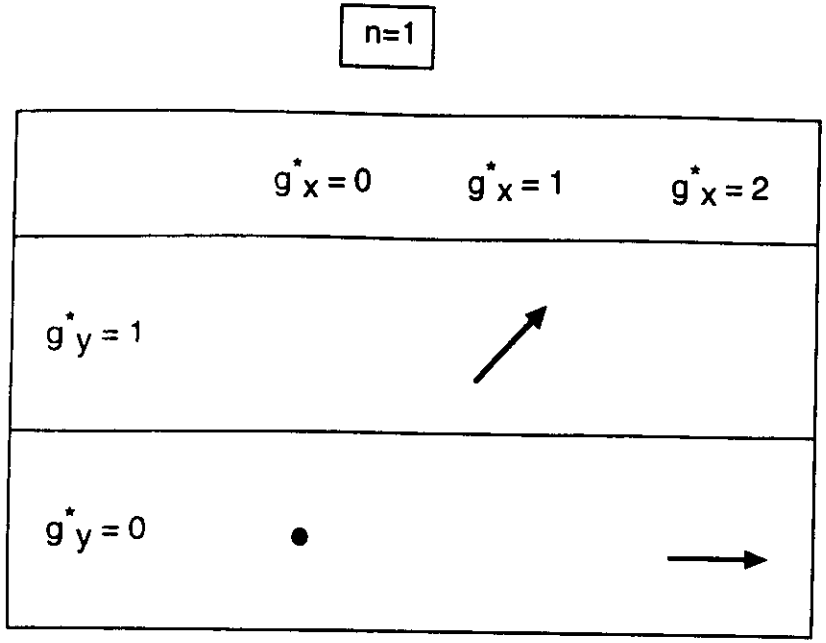

Fig 11
Part 1

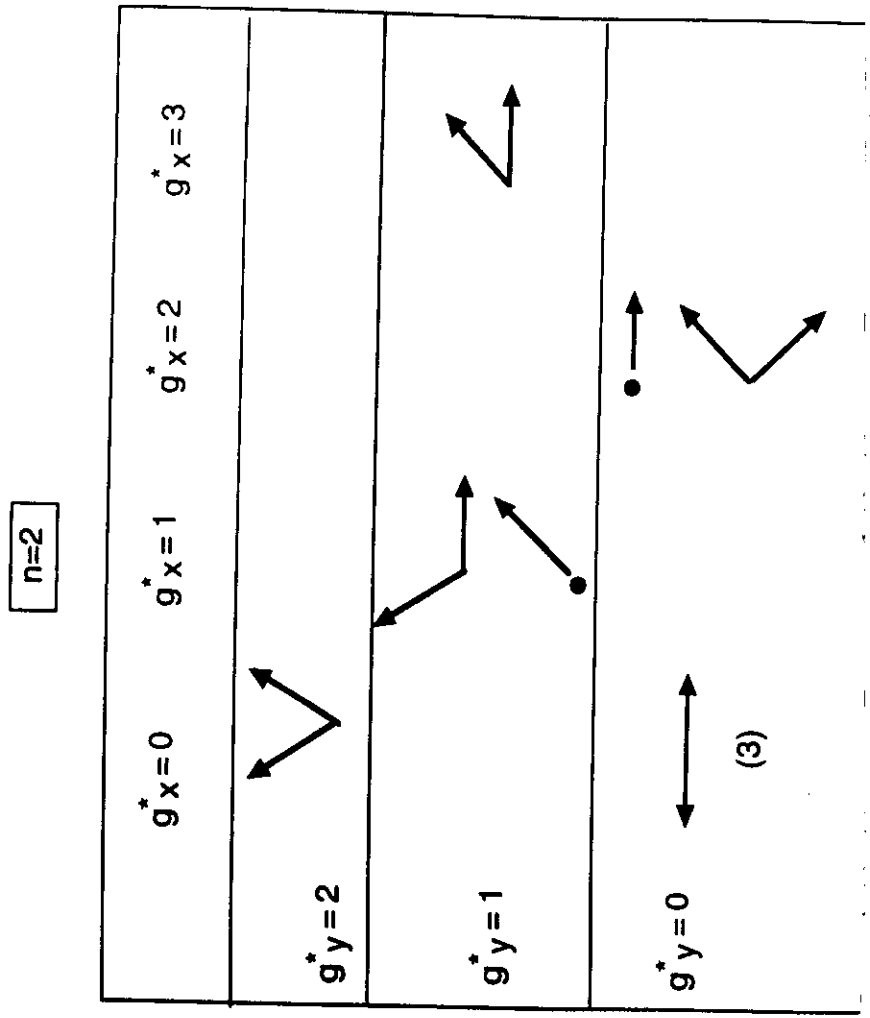

Fig 11
Part 2

Fig 11 Part 1

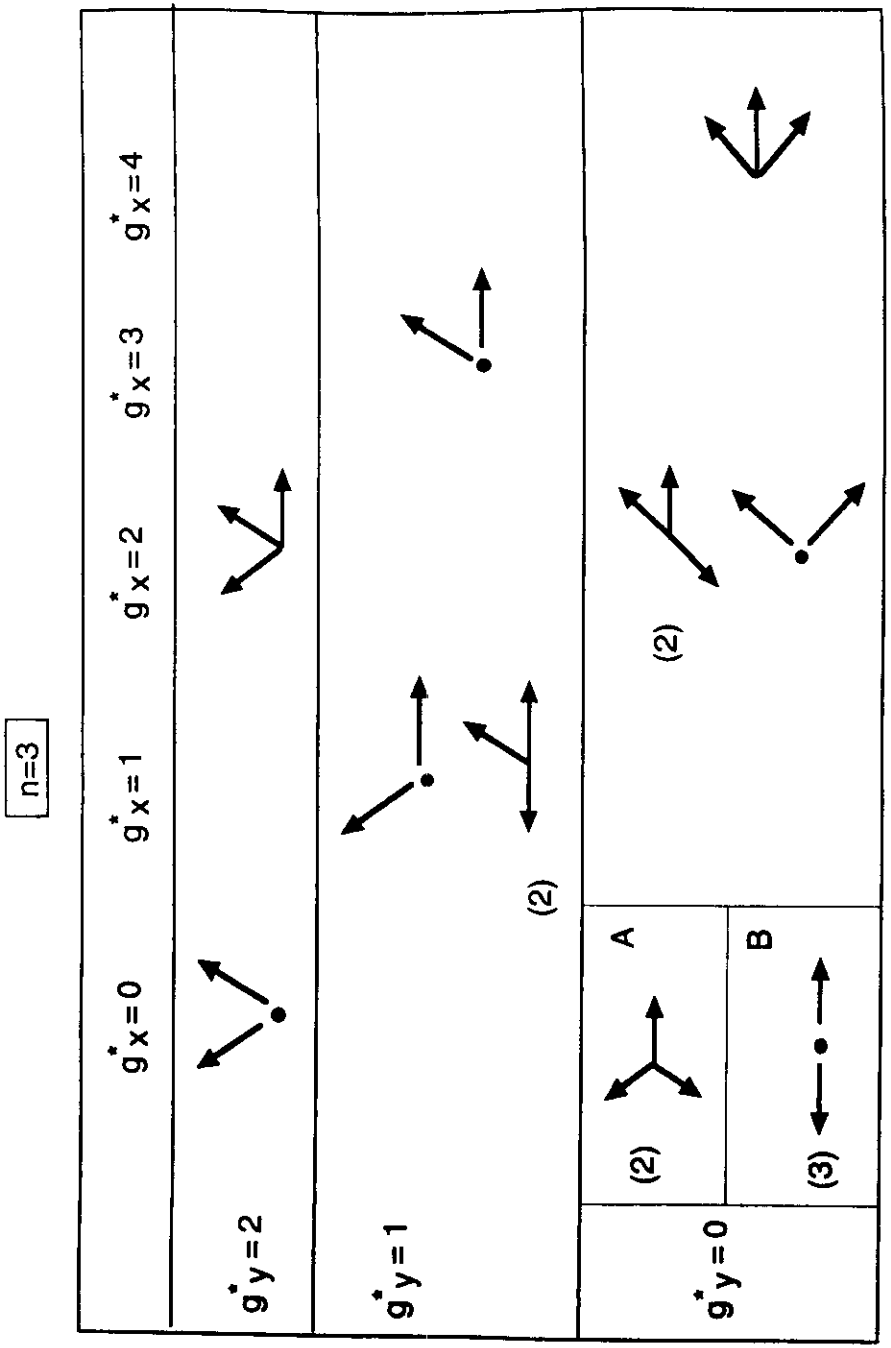

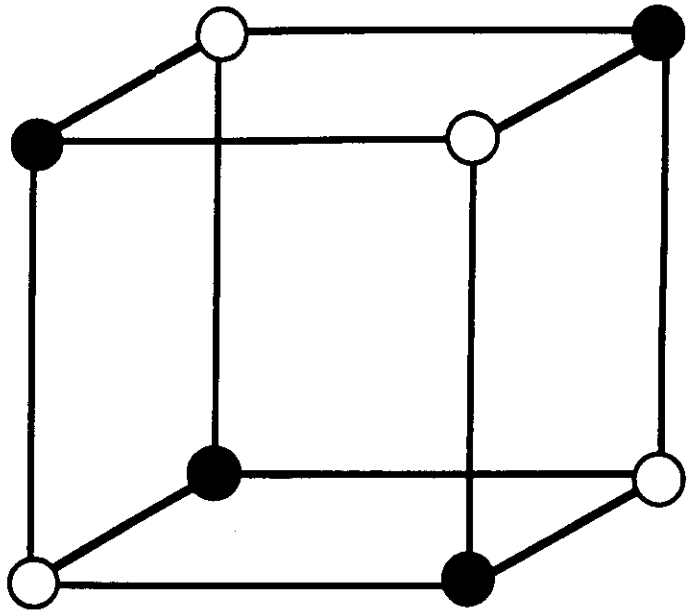

Fig 12

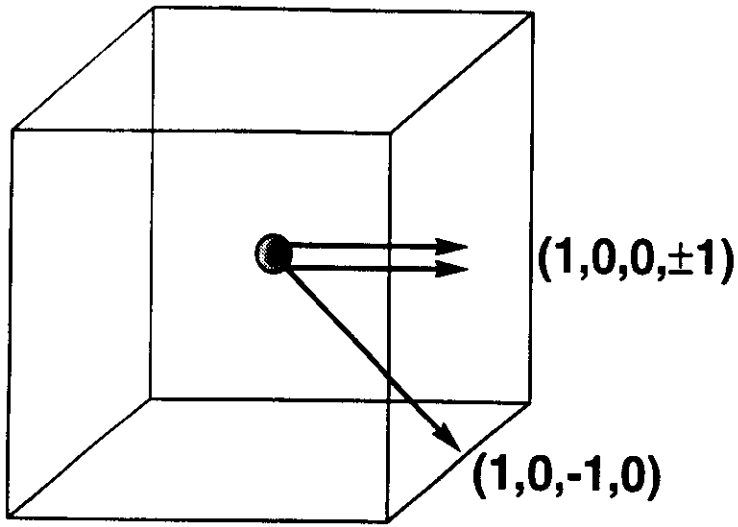

Fig 13

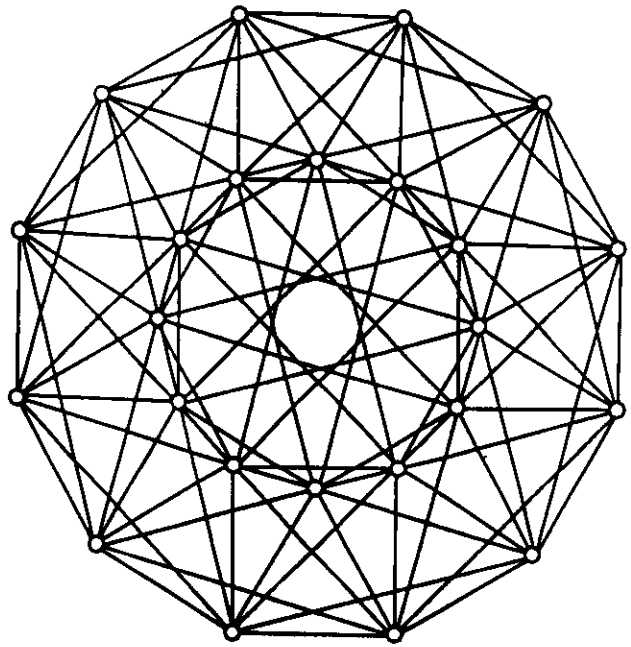

Fig 14

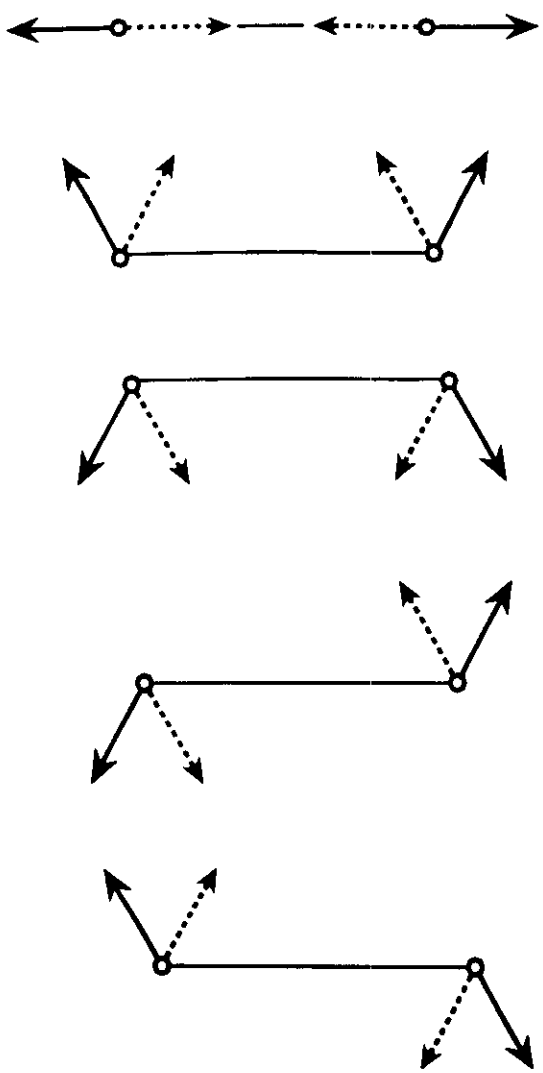

Fig 15

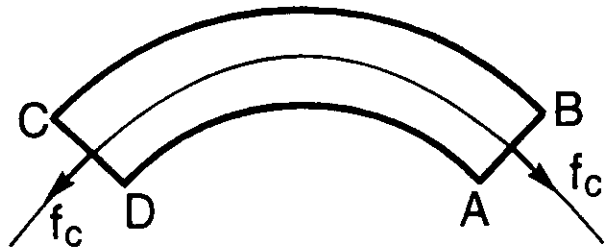

Fig 16

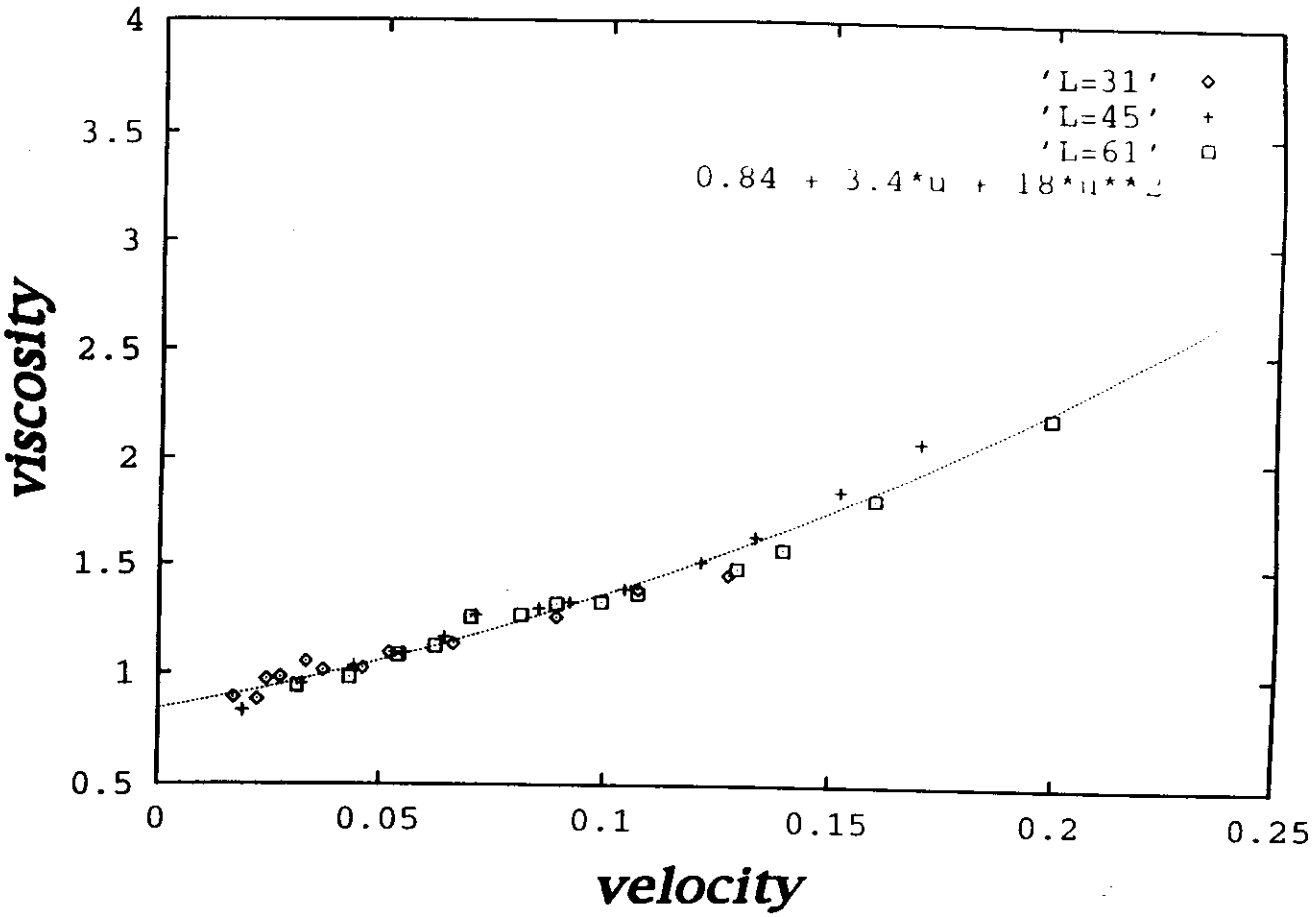
'L=31' ◇
'L=45' +
'L=61' □
0.84 + 3.4*u + 18*u**2
viscosity
velocity
4
3.5
3
2.5
2
1.5
1
0.5
0
0.05
0.1
0.15
0.2
0.25

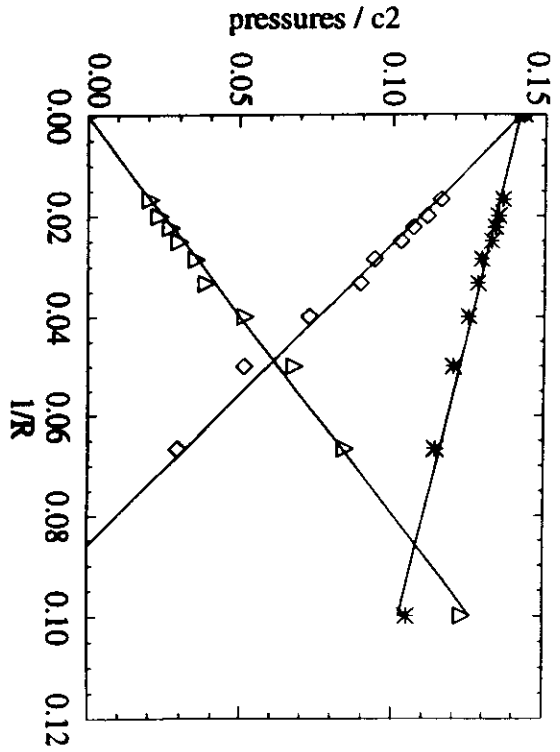
pressures / c2
1/R
0.00
0.05
0.10
0.15
0.00
0.02
0.04
0.06
0.08
0.10
0.12

Fig 18

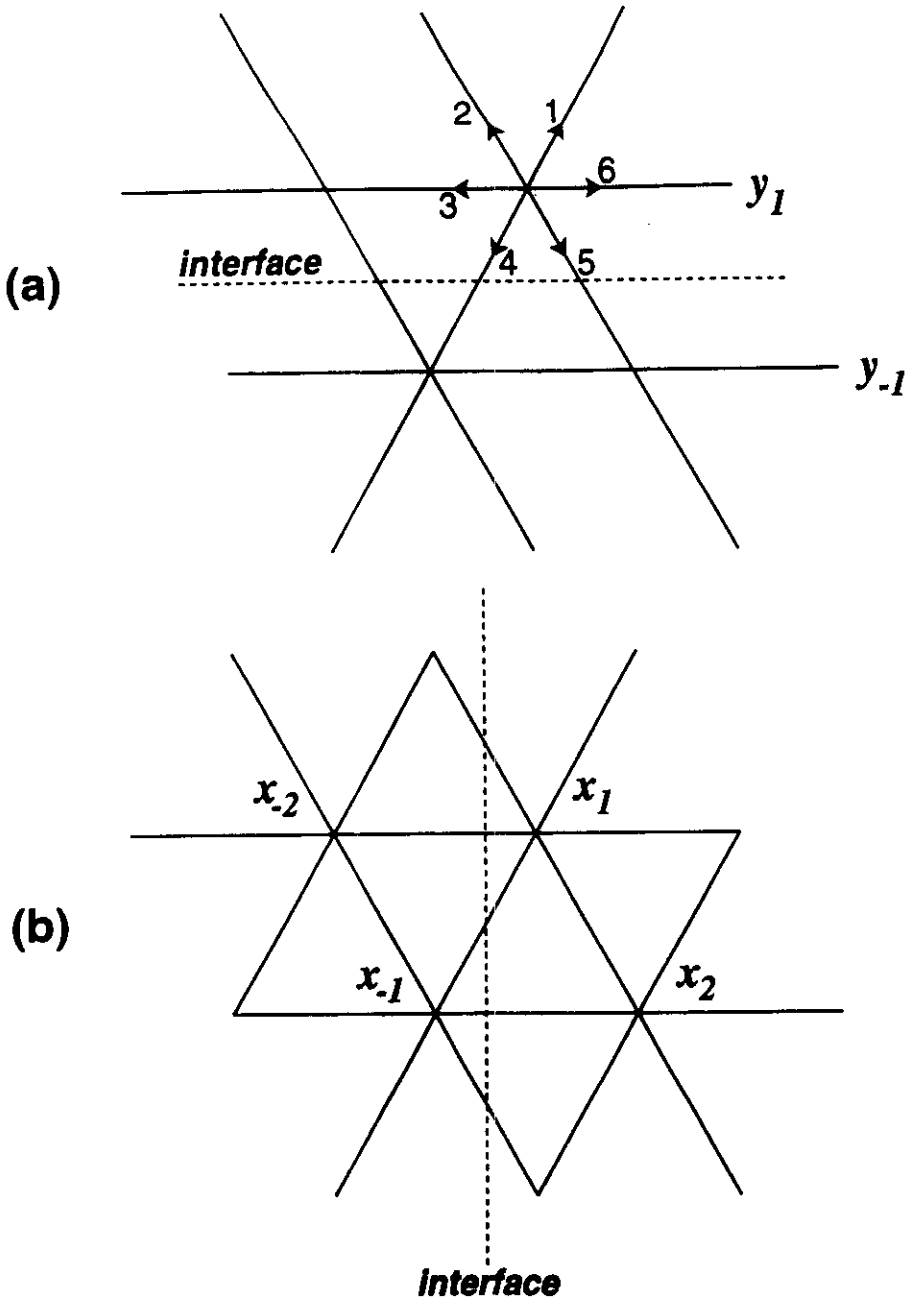
(a)
2
1
6
3
y_1
interface
4
5
y_{-1}
(b)
x_{-2}
x_1
x_{-1}
x_2
interface

Fig 19

Fig 20

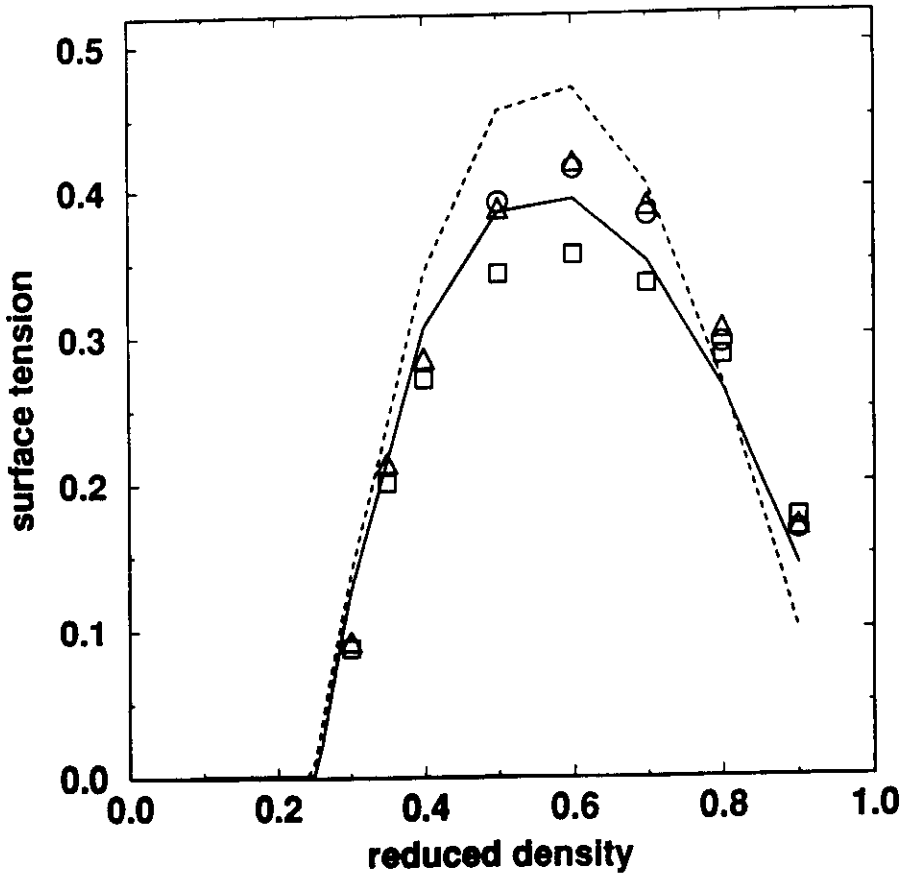
surface tension
0.0
0.1
0.2
0.3
0.4
0.5
0.0
0.2
0.4
0.6
0.8
1.0
reduced density

Fig 21

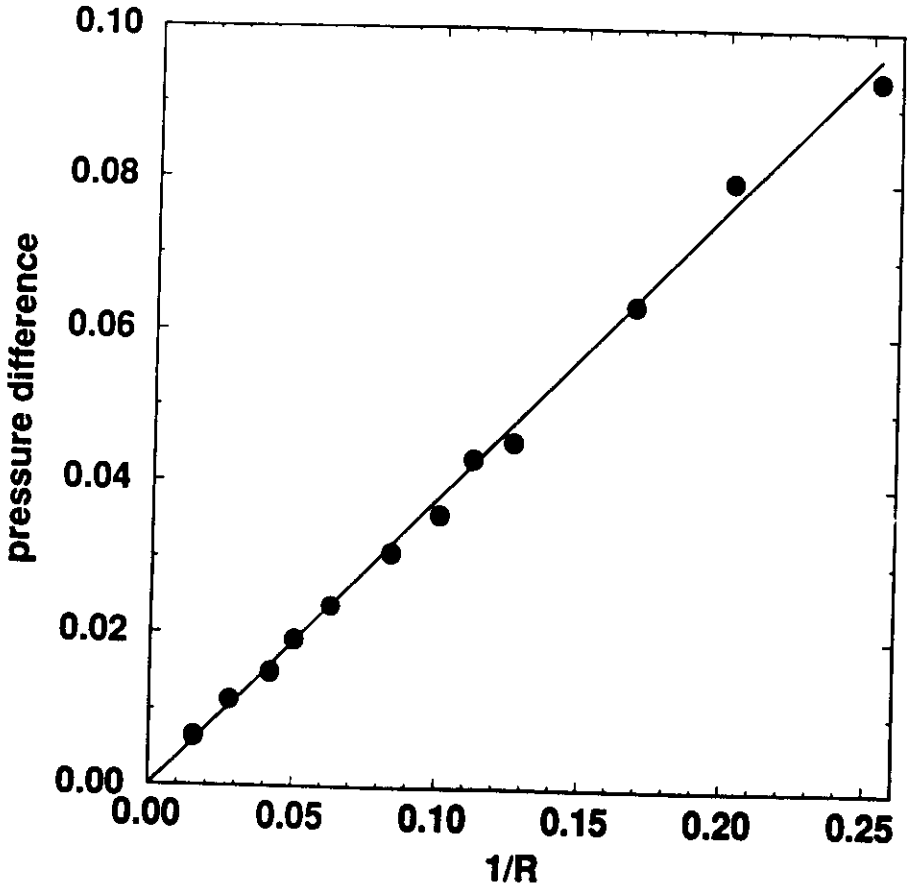
0.10
0.08
0.06
0.04
0.02
0.00
pressure difference
0.00
0.05
0.10
0.15
0.20
0.25
1/R

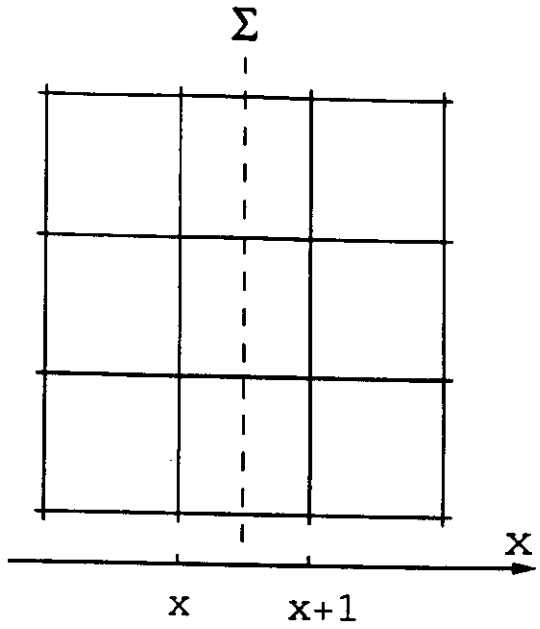
Σ
X
x
x+1

Fig 22

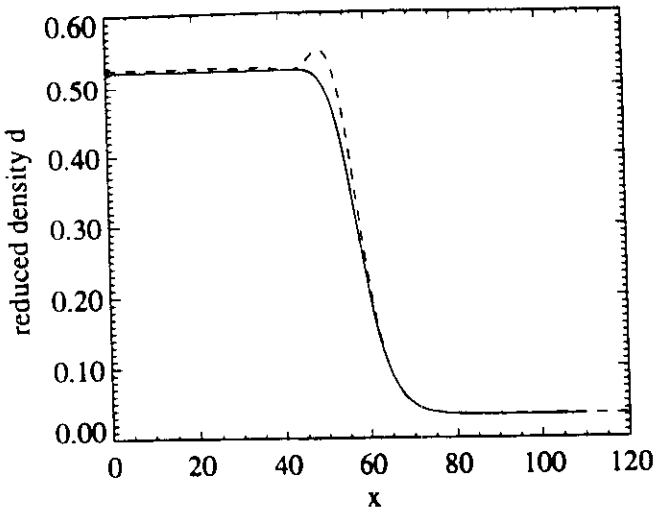
reduced density d
0.60
0.50
0.40
0.30
0.20
0.10
0.00
0
20
40
60
80
100
120
x

Fig 23

Fig 24

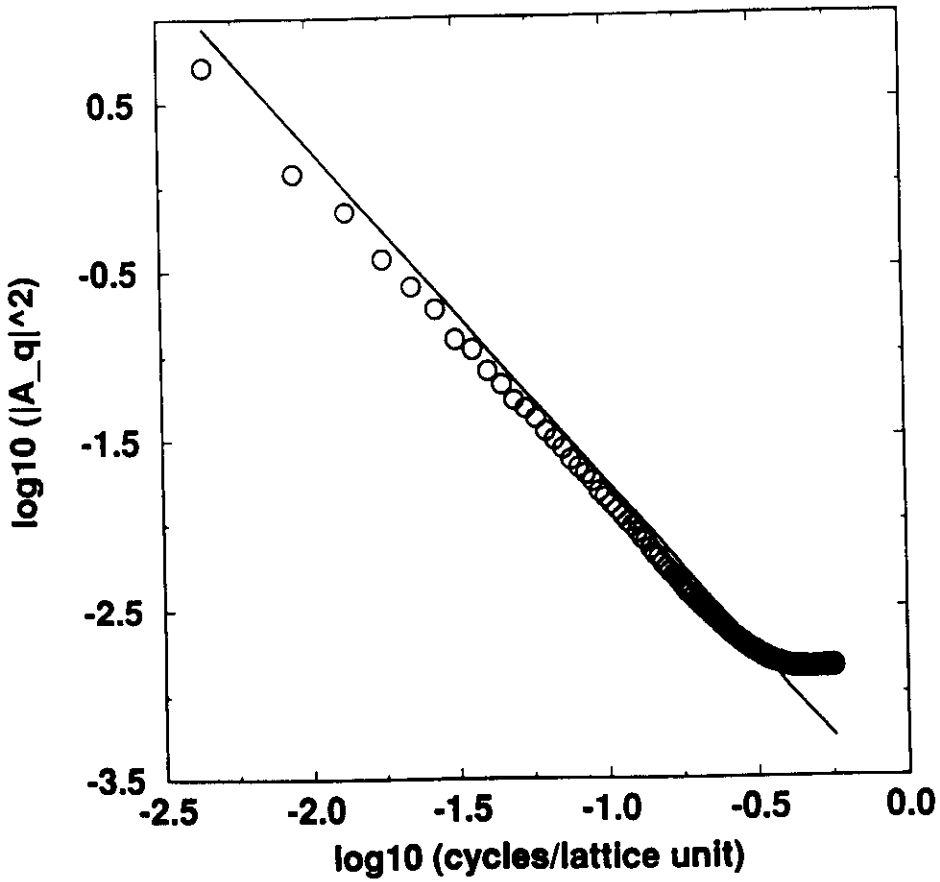
log10 (|A_q|^2)
0.5
-0.5
-1.5
-2.5
-3.5
-2.5
-2.0
-1.5
-1.0
-0.5
0.0
log10 (cycles/lattice unit)

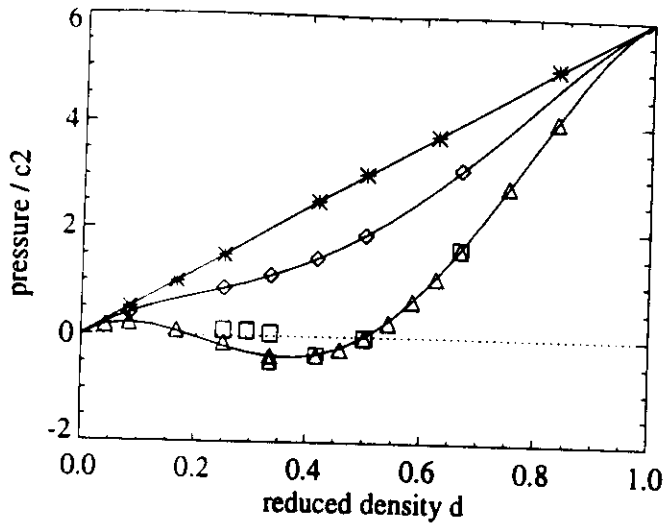
pressure / c2
6
4
2
0
-2
0.0
0.2
0.4
0.6
0.8
1.0
reduced density d

Fig 25

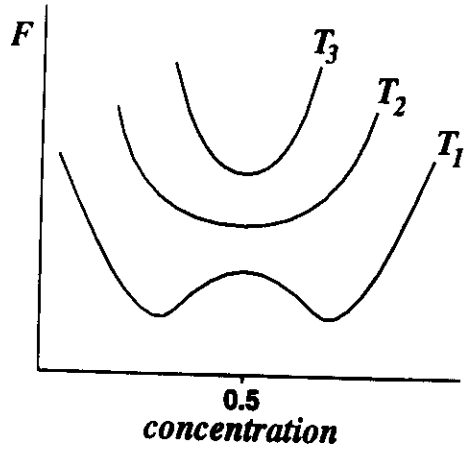
F
T_3
T_2
T_1
0.5
concentration

Fig 26

Fig 27

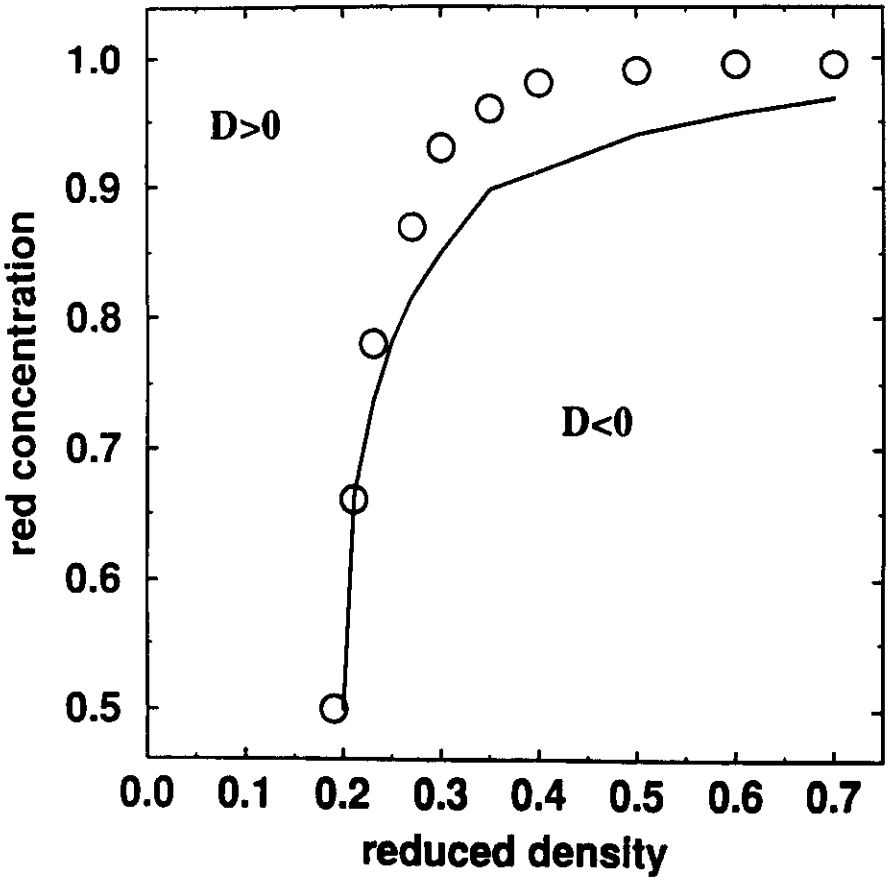
1.0
0.9
0.8
0.7
0.6
0.5
red concentration
D>0
D<0
0.0
0.1
0.2
0.3
0.4
0.5
0.6
0.7
reduced density

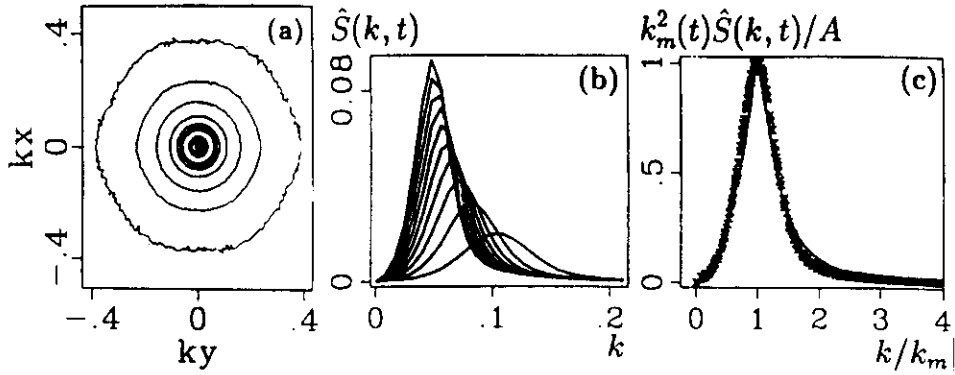
(a)
$\hat{S}(k,t)$
$k_m^2(t)\hat{S}(k,t)/A$
(b)
(c)
kx
ky
k
k/k_m

Fig 28

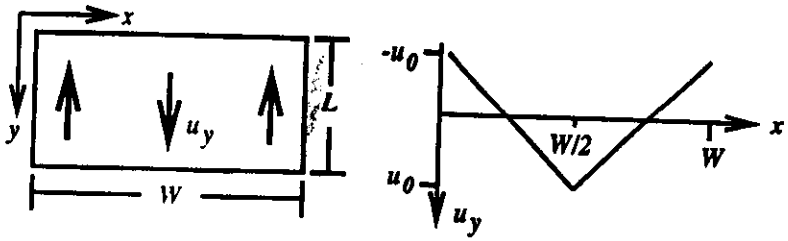
x
y
u_y
L
W
$-u_0$
u_0
u_y
W/2
W
x

Fig 29

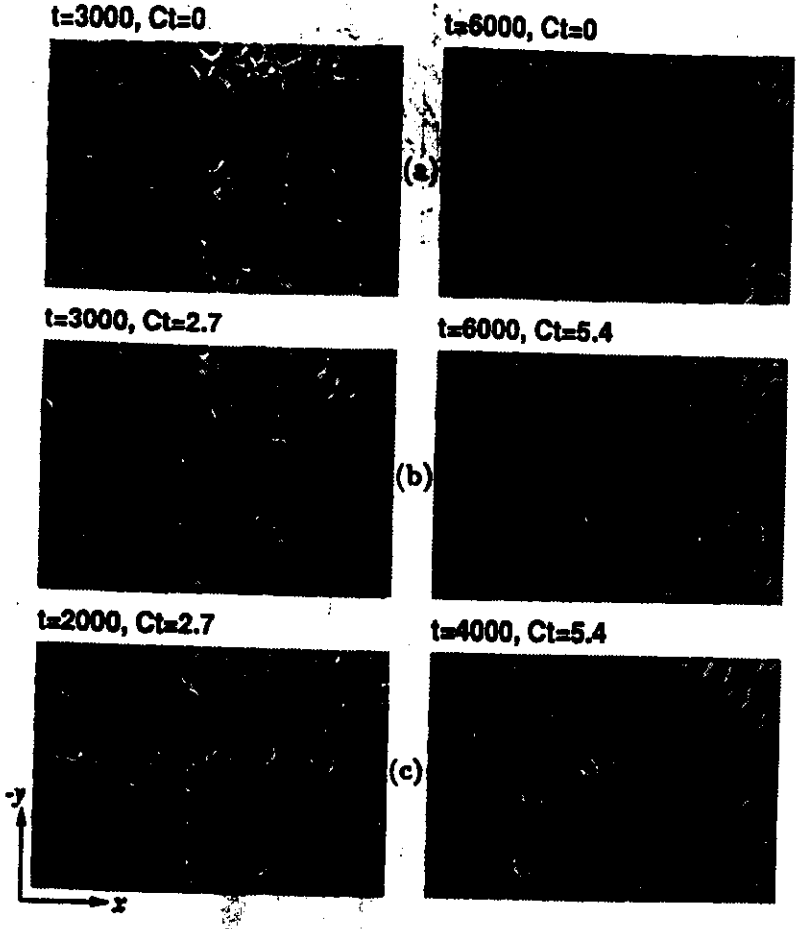
t=3000, Ct=0
t=6000, Ct=0
(a)
t=3000, Ct=2.7
t=6000, Ct=5.4
(b)
t=2000, Ct=2.7
t=4000, Ct=5.4
(c)
-y
x

Fig 30

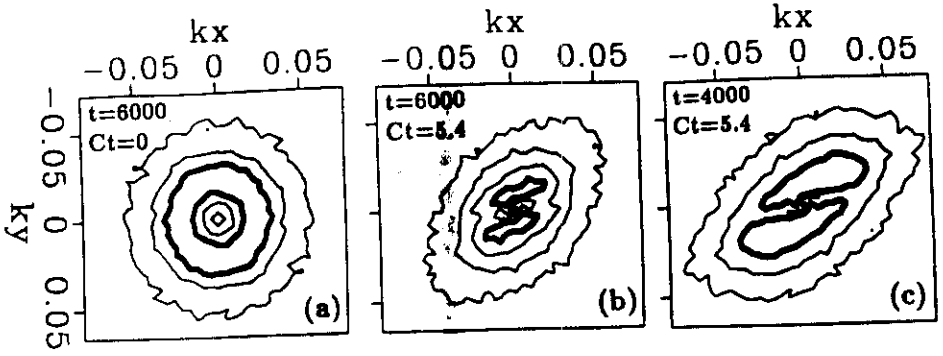
kx
−0.05 0 0.05
ky
−0.05 0 0.05
t=6000
Ct=0
(a)
kx
−0.05 0 0.05
t=6000
Ct=5.4
(b)
kx
−0.05 0 0.05
t=4000
Ct=5.4
(c)

Fig 31

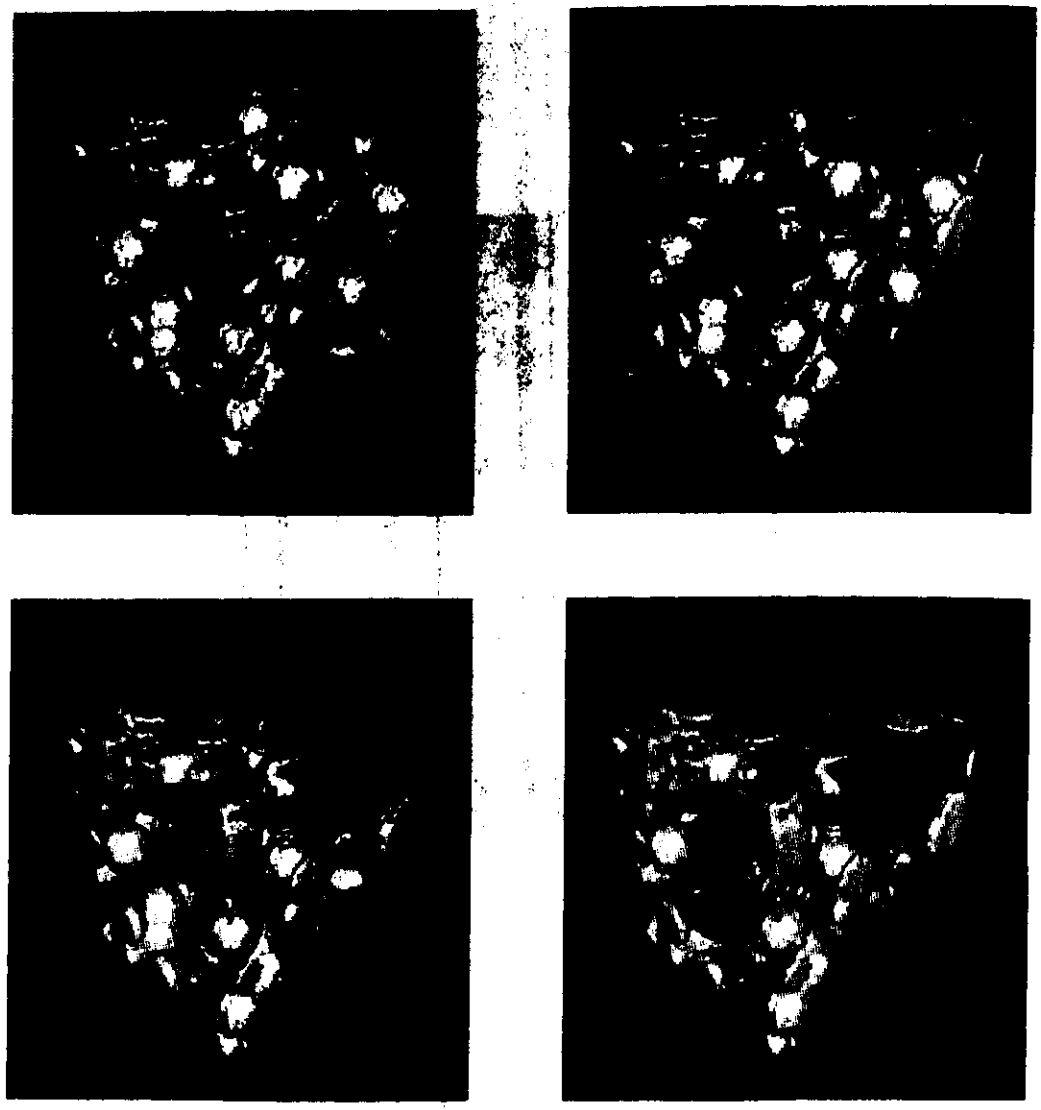

Fig 32

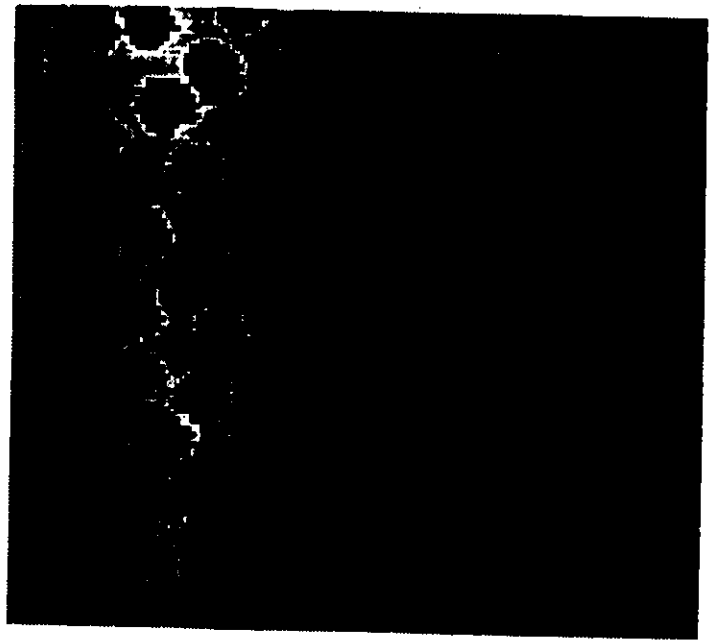

Fig 33

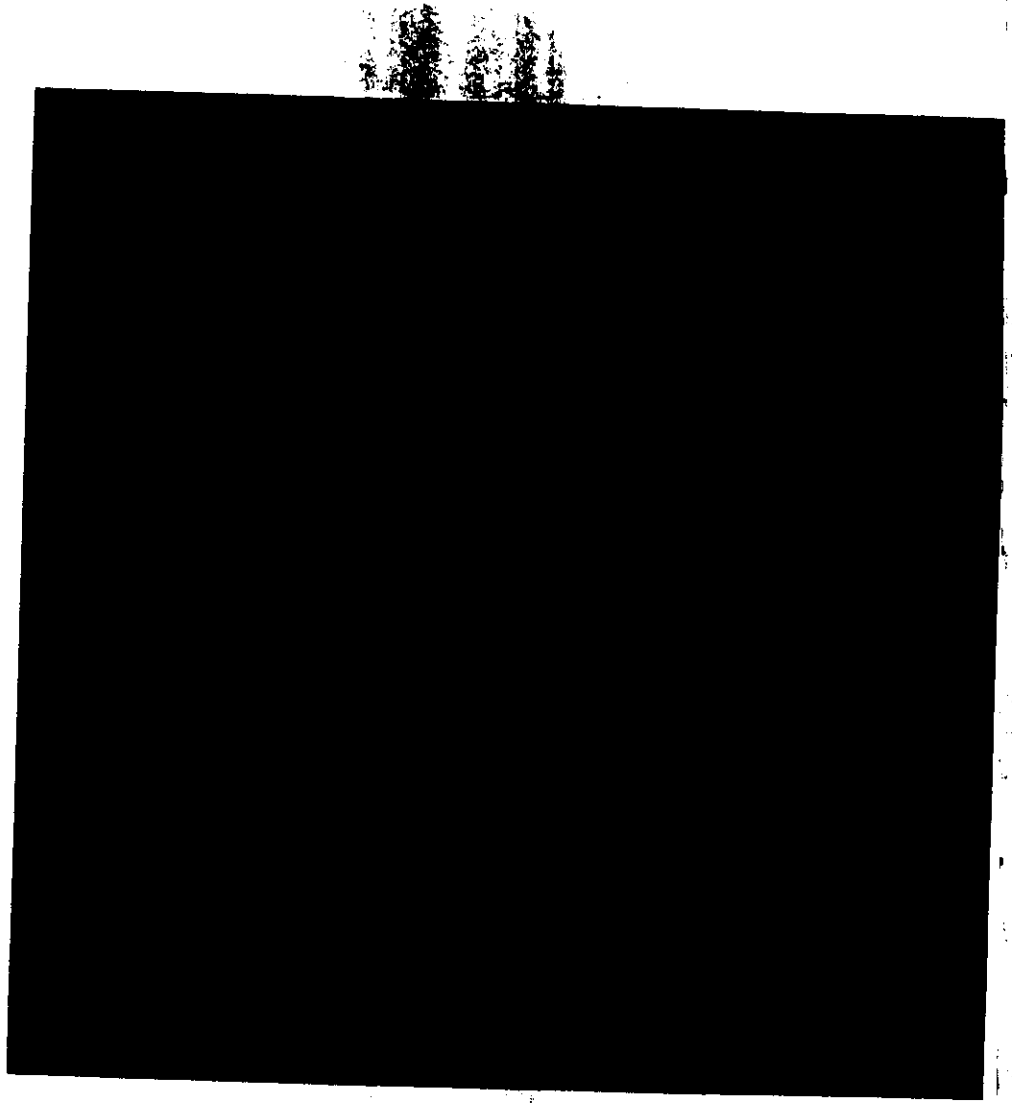

Fig 34

top

Fig 35

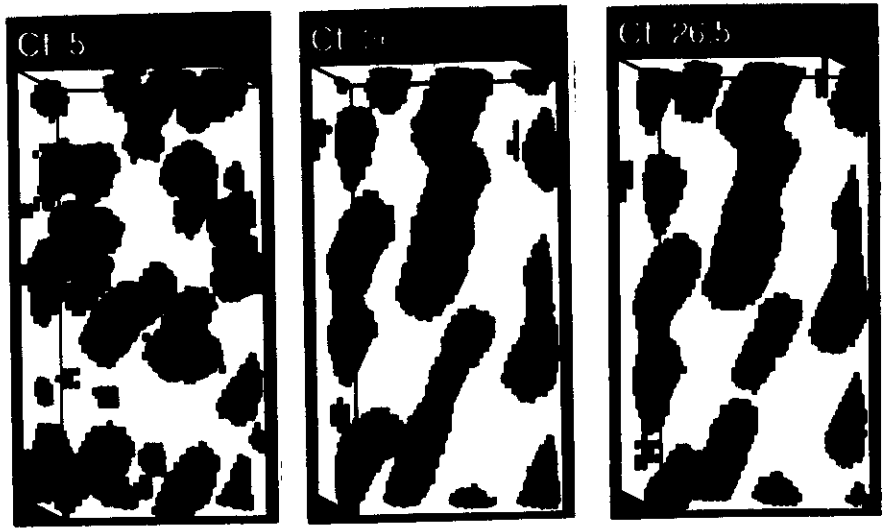

Fig 36

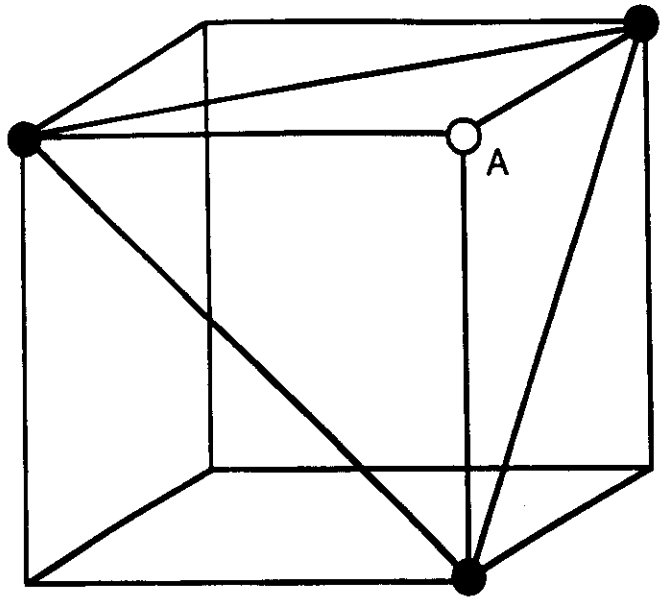

Fig 37

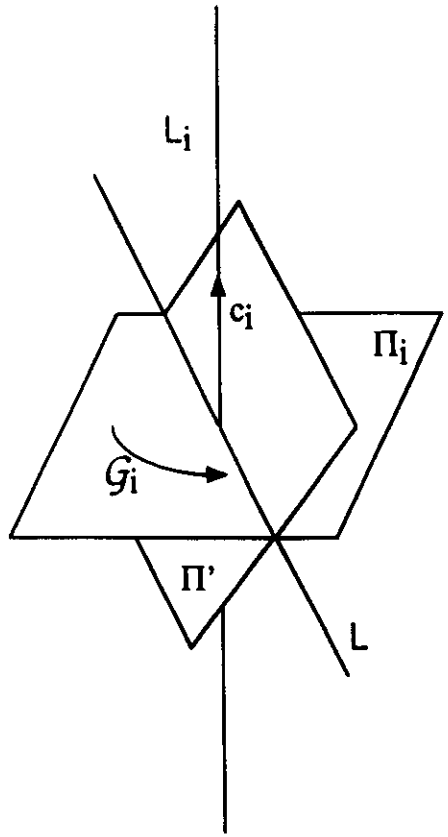

Fig 38

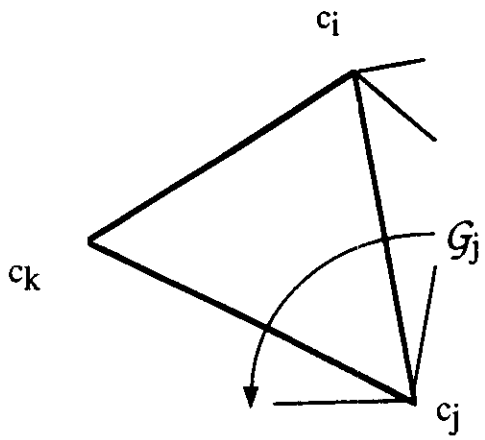

Fig 39